7

LBL-34800
UC-408

Lawrence Berkeley Laboratory

UNIVERSITY OF CALIFORNIA

ENERGY & ENVIRONMENT DIVISION

Polarized Light Scattering as a Probe for Changes in Chromosome Structure

D.B. Shapiro
(Ph.D. Thesis)

October 1993

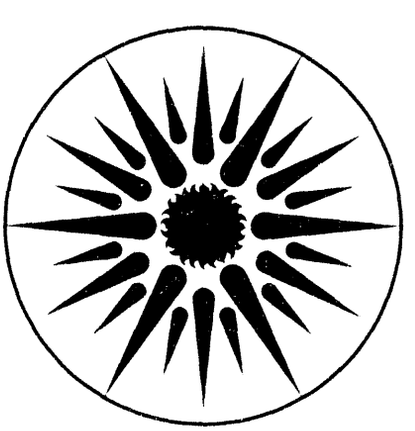

ENERGY & ENVIRONMENT DIVISION

Prepared for the U.S. Department of Energy under Contract Number DE-AC03-76SF00098

LBL-34800
UC-408

Polarized Light Scattering as a Probe for Changes in Chromosome Structure

Daniel Benjamin Shapiro
(Ph.D. Thesis)

Graduate Group in Biophysics
University of California, Berkeley

and

Energy and Environment
Lawrence Berkeley Laboratory
University of California
Berkeley, CA 94720

October 1993

This work was supproted by the Director, Office of Energy Research, Office of Basic Energy Sciences, Materials Sciences Division, of the Department of Energy under contract No. DE-AC03-76SF00098.

ABSTRACT

Polarized Light Scattering as a Probe for Changes in Chromosome Structure

by

Daniel Benjamin Shapiro

Doctor in Philosophy in Biophysics

University of California at Berkeley

Professor John E. Hearst, Chair

Measurements and calculations of polarized light scattering are applied to chromosomes. Calculations of the Mueller matrix, which completely describes how the polarization state of light is altered upon scattering, are developed for helical structures related to that of chromosomes. Measurements of the Mueller matrix are presented for octopus sperm heads, and dinoflagellates. Comparisons of theory and experiment are made.

A working theory of polarized light scattering from helices is developed. The use of the first Born approximation *vs* the coupled dipole approximation are investigated. A comparison of continuous, calculated in this work, and discrete models is also discussed. By comparing light scattering measurements with theoretical predictions the average orientation of DNA in an octopus sperm head is determined. Calculations are made for the Mueller matrix of DNA plectonemic helices at UV, visible and X-ray wavelengths. Finally evidence is presented that the chromosomes of dinoflagellates are responsible for observed differential scattering of circularly-

polarized light. This differential scattering is found to vary in a manner that is possibly correlated to the cell cycle of the dinoflagellates.

It is concluded that by properly choosing the wavelength probe polarized light scattering can provide a useful tool to study chromosome structure.

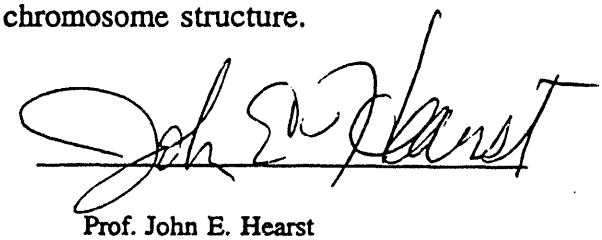

Prof. John E. Hearst

Chair, Thesis committee

Table of Contents

Acknowledgements

This work would not have been possible without the continued support and guidance of Dr. Arlon Hunt. I am also indebted to John Hearst for his help and criticisms during my graduate study. In addition, my collaborations with Marcos Maestre and Pat Hull were very worthwhile. Several chapters could not have been competed without the help of Yaomiong Shi and Martin McClain. The reading and critiques from Mary Hunt were also quite helpful. Finally the work conducted wuth Jamshid Arjomand and Terry Leighton, although not overly successful, was nevertheless rewarding.

As my mind was occupied by my academic endeavors with the help of those above, my body and spirit were being tended to by others during my graduate studies. I thank Christopher Dolder and Reginald Ray Savage for their instruction in dance. Finally I thank Lisa Kim for putting up with me, listening to me, and being there to occupy my thoughts when I was not thinking about Mueller matrices.

I. Introduction

The history of light scattering begins with the attempt to explain the color of the sky. The physicist Alhazen is recorded as proposing that the blue sky is due to reflected light in the eleventh century.[1] In the sixteenth century Da Vinci used aerosols to reproduce the blueness of the sky. [1] In 1802, J.B. Richter made recorded observations on the propagation of light in a colloidal sol. [2] In 1852, G.G. Stokes wrote[3] :

> "When any number of independent polarized streams, of given refrangibility, are mixed together, the nature of the mixture is completely determined by the values of four constants, which are certain functions of the intensities of the streams and of the azimuths and eccentricities of the ellipses by which they are respectively characterized; so that any two groups of polarized streams which furnish the same values for each of these four constants are optically equivalent."

The four constants mentioned above are now known as the Stokes parameters which completely describe the polarization properties of light. G. Govi and J. Tyndall also made observations on the light scattering properties of aerosols in 1860 and 1869.[1] They showed that the scattered light was polarized and Tyndall found that the degree of polarization depends on the size of the particle. Lord Rayleigh developed theory describing the light scattering from a small dielectric sphere based on electrodynamics.[1,4] This theory was sufficient to explain the color of the sky. The solution of the scattering problem for a sphere of arbitrary size is attributed to G. Mie. [1]

Rayleigh also derived an approximate theory for the light scattering from an arbitrary particle.[4] This theory was further developed by P. Debeye in 1915.[1] The theory applies to particles that are not strong scatterers. This theory has also become known as the first Born approximation from its application in quantum mechanics. P. Soleillet showed that the four Stokes parameters describing the intensity and polarization state of light emerging from an optical element are a linear combinations of the Stokes parameters describing the incident light.[5] In 1942, F. Perrin published a paper, building on earlier work by R.S. Krishnan and Soleillet, that described sixteen coefficients characteristic of a scattering medium that fully describe how the intensity and polarization state of light is altered upon scattering.[6] He derived symmetry relationships between the sixteen parameters that we will outline in the next chapter. The work of Soleillet and Perrin was formulated as a matrix calculus by Hans Mueller around 1943.[7,8] The matrix containing Perrin's sixteen coefficients is known as the Mueller matrix.

In the late 1940s and 1950s researchers began to develop instruments to study the angular dependence of scattered light.[2] An instrument developed by B. Zimm served as a prototype for many others.[2,9] This instrument included two photomultiplier tubes to detect the incident and scattered light. The detector could be moved to examine the scattering at different angles. Zimm conducted experiments on polystyrene spheres and compared his data with theoretical calculations based on the work of P. Debeye.[9] The goal of his work was to demonstrate the ability of light scattering to determine the size and shape of macromolecules. A further advance in the development of light scattering technology came with the work by B.A. Brice *et al.* in 1950.[10] They used a photomultiplier tube mounted on a movable arm to measure

light scattering from 0° to 135°. By placing a monochromatic filters after their mercury lamp light source they were able to measure wavelength dependence. They also used linear polarizers aligned parallel or perpendicular to the scattering plane before and after the sample in order to determine the ratio of linear polarization in the scattered light (depolarization). These measurements, together with those of the turbidity and dissymmetry (intensity at 45° *vs* that at 90°), made it possible for them to obtain values for the molecular weights of several polymers based on theory developed by Debeye. In 1952 P. Horn and H. Benoit reported values for the length and anisotropy in the polarizability of tobacco mosaic viruses.[11] Their theoretical predictions were based on those of Debeye. They measured the angle dependence of scattered light with combinations of linear polarizers placed before and after (an analyzer) the sample. They measured V_v, V_h, H_h, and H_v, where V and H refer to vertically or horizontally placed polarizers and v and h to the corresponding analyzers. These intensities (defined by R.S. Krishan in 1938[12]) are still measured today in the field of depolarized dynamic light scattering.[13] The study by Horn and Benoit gave a good result for the length of the virus particle but the theory they used did not produce an accurate value for the anisotropy in the polarizability. B.S. Pritchard and G. Elliot developed an instrument, the "Recording Polar Nephelometer," to measure the Mueller matrix as a function of angle in 1960.[14] The Mueller matrix completely determines how a scattering system will alter the intensity and polarization state of light. The Recording Polar Nephelometer used sets of horizontal, vertical, diagonal and circular polarizers as polarizers and analyzers to determine the Mueller matrix. The instrument was used to study the optical properties of the atmosphere. Some of the Mueller matrix elements are very small compared to the

total intensity of scattered light. They should therefore be measured using some kind of modulation technique. Z. Sekera modulated the polarization state of incident light by rotating the polarizers in 1957.[15] A better modulation technique was developed in 1973 by A.J. Hunt and D.R. Huffman by coupling a photoelastic modulator to a polar nephelometer.[16] Measurements on this instrument of the Mueller matrix for Mie as well as Rayleigh size spheres agreed well with theoretical predictions. The instrument used in the measurements of the present work is based on the 1973 instrument and will be described in detail in chapter 4.

The application of polarized light scattering to structural biology was first proposed by P.J. Wyatt in 1968.[17] Wyatt proposed the use of differential scattering of linearly polarized light (S_{12}) to differentiate between different species of bacteria. Around the same time, interesting anomalies in circular dichroism spectra were being investigated that would eventually lead to the application of differential scattering of circularly polarized light as a probe in structural biology. D.W. Urry and coworkers were the first to propose and then show that some anomalies observed in circular dichroism spectra were partially due to differential scattering of polarized light.[18,19] In 1970, A.S. Schneider showed that anomalous CD spectra for red blood cell membranes could be corrected with the elimination of scattering by the samples.[20] Shortly thereafter, L.D. Barron and A.D. Buckingham calculated the intensity of Rayleigh and Raman scattering from optically active molecules.[21] They defined the circular intensity differential as the difference of the intensity of right *vs* left circularly polarized light divided by the sum of these intensities. This quantity is now known as circular intensity differential scattering (CIDS). These authors proposed that CIDS could be used to study optically active molecules. Maestre *et al.*

measured significant CD for bacteriophages at long wavelengths where there is no absorption for these particles.[22] This CD was attributed to differential scattering of circularly polarized light (CIDS). Shortly afterwards Dorman *et al.* showed that the scattering effects could be eliminated by using a detector that collected transmitted as well as scattered light.[23] They proposed that CIDS could be used as a probe of ordered macromolecular structure. The work of Dorman *et al.* was published in the same year as that of Hunt *et al.* Purcell and Pennypacker developed theory now known as the coupled dipole approximation, a light scattering theory that accounts for internal dipolar interactions, in the field of astrophysics in 1973.[24] Harris *et al.* developed a generalized theory of polarized light scattering published in 1974 for an ensemble of randomly oriented polymers of a general geometry allowing for some internal dipolar interactions.[25] In 1976, an article appeared in PNAS entitled "Application of polarization effects in light scattering: A new biophysical tool."[26] It was therein proposed that the Hunt's light scattering instrument be used to measure the angular dependence of polarized light scattering from biological samples to investigate scattering effects observed in CD spectra. It is this proposal that motivates the current work.

Major contributions, upon which much of the current work is based, to the theory of polarized light scattering were made by C. Bustamante and coworkers in calculating CIDS from helices. These researchers recognized the potential of CIDS to study chiral particles such as chromosomes. Bustamante *et al.* calculated CIDS from a single helix oriented parallel or perpendicular to the incident light using the first Born approximation.[27] The helix was defined as a continuous dielectric with a uniaxial polarizability tangent to the helix. In the first Born approximation, CIDS is

zero when the polarizability is isotropic. By defining an anisotropic (in this case uniaxial) polarizability tensor internal interactions (ignored by the first Born approximation) are compensated for resulting in a non-zero CIDS. It was shown that the angular dependence of CIDS is much more sensitive to helical parameters (pitch, radius, sense, and length) than is the total scattering intensity.[28] The theory was later developed to include a triaxial polarizability tens~~[29] and the second Born approximation.[30] In addition, using a helix composed of point polarizable groups, the CIDS in the orientation average using the first Born approximation was calculated.[31] These theories were applied to superhelical structures where it was shown that the overall CIDS is a superposition of that from each helical level.[32]

Another group that has made large contributions to polarized light scattering theory is that lead by W.M. McClain. McClain *et al.* have concentrated on problems in obtaining the Mueller matrix elements in the orientation average.[25,33,34] They have used the Wigner matrix formalism to this end. McClain, Schauerte, and Harris showed that certain elements are always zero in the orientation average when the first Born approximation is applied.[33] An analytical solution was obtained for the Mueller matrix in the orientation average using the coupled dipole approximation by Mclain and Ghoul in 1986.[34] The first group to apply the coupled dipole approximation to calculate the Mueller matrix was that of Zeitz, Belmont and Niccolini.[35] Nicollini's group modelled polarized light scattering from polynucleosome structures placing one dipole at each nucleosome position. They used a numerical method to calculate the orientation average. A comparison made by McClain's group between numerical and analytical approaches to obtaining an orientation average showed the superiority of the analytical solution.[36] More recent work has McClain *et al.* has

focused on problems in the longwave limit[37,38] and most recently a closed form solution to the problem of polarized light scattering from long, thin cylinders has been obtained.[39] This later result should prove to be more widely applicable than the infinite cylinder solution.[40]

A group including S.B. Singham and G.C. Salzman have also made important contributions to the theory of polarized light scattering using the coupled dipole approximation. They applied the coupled dipole approximation to a variety of structures for single particles[41] and for an orientation average.[42] They showed that a helix modelled by spherical or prolate spheroidal subunits is equivalent as long as the thickness of the subunits are the same and Maxwell-Garnett theory[40] is used to determine the polarizability of the dipole representing the subunit.[43] In the same publication this group did a preliminary investigation of the necessity of including dipolar interactions. We will conduct a similar investigation in chapter three. Other work by Singham and others includes an approximate solution to the computationally cumbersome coupled dipole theory[44-46] and applications to optically active particles.[47]

Early measurements of CIDS were conducted on CD or modified CD machines similarly to those conducted by Maestre. CD present outside absorption bands is interpreted as resulting from CIDS. Nicollini and Kendall measured CIDS from chromatin in this way in 1977.[48] Work by Maestre *et al.* showed that the CD/CIDS of chinese hamster ovary cells is cell cycle dependent.[49] Another important example of this type of measurement is that conducted by Livolant and Maestre on chromosomes of dinoflagellates.[50] By comparing the apparent CIDS from single dinoflagellates in a CD microscope to that of cholesteric phases of DNA these

authors provided evidence that the chromosomes of dinoflagellates are similar in structure to nematic cholesteric liquid crystals. Recently, a Russian group has used a modified CD apparatus to measure CIDS in order to study the compaction of DNA by spermine.[51]

A CD spectrometer can be useful in determining the presence of CIDS but does not provide the abundance of information that the angular dependence of CIDS could. In addition the other Mueller matrix elements cannot be measured in a CD machine. As mentioned above, measurements of the angular dependence of polarized light scattering began with the work of Wyatt measuring S12 on bacteria. In the field of ocean optics several researchers concerned themselves with measurements of the entire Mueller matrix.[52,53] With few exceptions, the application of polarized light scattering to structural biology has mostly been concerned with CIDS, or S_{14}. Maestre *et al.* reported a relatively large CIDS from helical sperm heads.[54] Salzman and coworkers have tried to develop the measurement of S_{14} for microbial identification.[55] They report measurements of virus particles of the order of 0.01% of S_{11}. This sensitivity is much greater than that obtainable by the methods of the present work. To our knowledge Salzman's application of CIDS has not been widely used. An arguably more promising application of polarized light scattering to microbiology is that by Bronk and coworkers.[56] They used S_{34} to size bacterial populations. Other measurements of the angular dependence of Mueller matrix elements include those made on chloroplast membranes[57], sickling hemoglobin[58] (S_{14} is proposed as a measure of polymer formation), and single immobilized dinoflagellates.[59] Measurements of immobilized particles including dinoflagellates are described in this work in chapter seven. Nicollini and coworkers have recently

made polarized light scattering measurements using a technique with significant modifications from that of Hunt *et al.* [60,61] This does not use the feedback circuit used in Hunt's instrument. Measurements on spheres using Nicollini's apparatus has not to our knowledge been compared to Mie theory in a rigorous way as has the instrument developed by Hunt and Huffman. Nicollini and coworkers have published measurements of the angular dependence of several Mueller matrix elements made on nucleosomes and polynucleosomes showing great sensitivity to higher order structure.[60] In addition, they have shown differences in CIDS at 632 nm. measured from λ–DNA in buffers with different concentrations of ethidium bromide.[61] They conclude that CIDS measured in their instrument is sensitive to the writhe of the DNA. Unfortunately no sample analysis was presented. We feel that the intriguing results obtained by Nicollini *et al.* deserve further investigation.

In order to fully exploit the information contained in measurements made of the Mueller scattering matrix, models based on theoretical calculations must be compared to experimental data. Considerable progress has been made in the study of polarized light scattering by spherical particles. Bricaud and Morel used Mie scattering theory applied to homogeneous spheres to model light scattering from various marine microorganisms.[62] Quinby-Hunt *et al.* showed that comparing the Mie description of coated spheres with experimental data taken from marine *Chlorella* yields information about the optical and geometrical properties of this alga.[53] Mie theory provides an exact solution to the problem of elastic scattering from a sphere. Unfortunately, it cannot be applied to other, more complex geometries, such as helices, where approximate methods must be used. Several authors have used various methods to model light scattering from helices.[27-32,43,63]

The utility of each of these methods will ultimately be determined by comparison with experimental data. One of the few studies on light scattering from helical particles where theoretical predictions were compared to measurements was conducted by Wells *et al.*[64] This group showed that a relatively simple model could be used to model the S_{14} Mueller matrix element measured from a collection of helical, screw-like, octopus sperm heads. Their model consisted of a thin wire helix made up of point-polarizable groups that do not interact (the first Born approximation). This model proved to be reasonably successful but, it is possible that a model that accounts for interaction between groups, the coupled-dipole approximation method, may be more successful in modelling these helical structures. The evaluation of various models and their application to octopus sperm heads is a major goal of the present work.

II. Electromagnetic Theory

Light is a form of electromagnetic radiation. Electromagnetic radiation and its interaction with matter are described by Maxwells' equations. The macroscopic form of these equations are:

$$\vec{\nabla} \cdot \vec{D} = 4\pi\rho \quad \vec{\nabla} \times \vec{H} = \frac{4\pi}{c}\vec{J} + \frac{1}{c}\frac{\partial \vec{D}}{\partial t} \tag{2.1}$$
$$\vec{\nabla} \cdot \vec{B} = 0 \quad \vec{\nabla} \times \vec{E} + \frac{1}{c}\frac{\partial \vec{B}}{\partial t} = 0,$$

where $\vec{E}$ and $\vec{B}$ are the electric and magnetic fields, ρ and $\vec{J}$ are the charge and current densities. $\vec{D}$ and $\vec{B}$ are related to the electric and magnetic fields as follows:

$$\vec{D} = \vec{E} + 4\pi\vec{P} \quad \vec{H} = \vec{B} - 4\pi\vec{M}, \tag{2.2}$$

where $\vec{P}$ is the polarization and $\vec{M}$ is the magnetization of the material medium. For many types of materials (those that are isotropic),

$$\vec{P} = \chi\vec{E} \quad \vec{B} = \mu\vec{H} \quad \vec{J} = \sigma\vec{E}, \tag{2.3}$$

where χ is the electric susceptibility, μ the permeability, and σ the conductivity of the medium. The dielectric constant describing the medium is related to the electric susceptibility as follows:

$$\varepsilon = 1 + 4\pi\chi. \tag{2.4}$$

Thus,

$$\vec{D} = \varepsilon\vec{E}. \tag{2.5}$$

When the medium is devoid of charges and currents, and the dielectric constant and permeability are constant, Maxwells' equations become

$$\vec{\nabla} \cdot \vec{E} = 0 \quad \vec{\nabla} \times \vec{B} - \frac{\mu\varepsilon}{c}\frac{\partial \vec{E}}{\partial t} = 0 \tag{2.6}$$
$$\vec{\nabla} \cdot \vec{B} = 0 \quad \vec{\nabla} \times \vec{E} + \frac{1}{c}\frac{\partial \vec{B}}{\partial t} = 0,$$

Taking the curl of the curl of $\vec{E}$ we have,

$$\begin{aligned} &\vec{\nabla} \times \vec{\nabla} \times \vec{E} + \frac{1}{c} \frac{\partial(\vec{\nabla} \times \vec{B})}{\partial t} \\ &= \vec{\nabla}(\vec{\nabla} \cdot \vec{E}) - \nabla^2\vec{E} + \frac{1}{c} \frac{\partial(\frac{\mu\varepsilon}{c} \frac{\partial\vec{E}}{\partial t})}{\partial t} \\ &= -\nabla^2\vec{E} + \frac{\mu\varepsilon}{c^2} \frac{\partial^2\vec{E}}{\partial t^2} = 0. \end{aligned} \tag{2.7}$$

Thus we have the wave equation in terms of the electric field:

$$\nabla^2\vec{E} - \frac{\mu\varepsilon}{c^2} \frac{\partial^2\vec{E}}{\partial t^2} = 0. \tag{2.8}$$

A similar equation can be derived in terms of the magnetic field. A solution of these wave equations for a plane wave propagating in the $\hat{r}$ direction is:

$$\vec{E} = \vec{E}_0 e^{i\vec{k}.\vec{r} - i\omega t} \text{ and } \vec{B} = \vec{B}_0 e^{i\vec{k}.\vec{r} - i\omega t}, \tag{2.9}$$

where $\vec{E}_0$ and $\vec{B}_0$ are amplitude vectors, and the magnitude of the propagation vector, $\vec{k}$, $k = \sqrt{\mu\varepsilon}\frac{\omega}{c}$. k is called the wave number. It is related to the wavelength by:

$$k = 2\frac{\pi}{\lambda} \tag{2.10}$$

The velocity of the wave in the medium, v, is given by:

$$v = \frac{c}{\sqrt{\mu\varepsilon}} = \frac{\omega}{k} \tag{2.11}$$

Certain other restrictions are imposed on the solution of Equation 2.9 by Maxwells' equations. The condition that the divergence of the electric field be zero gives:

$$\begin{aligned} &\vec{\nabla} \cdot \vec{E}_0 e^{i\vec{k}.\vec{r} - i\omega t} \\ &= e^{i\vec{k}.\vec{r} - i\omega t} \vec{\nabla} \cdot \vec{E}_0 + \vec{E}_0 \cdot \vec{\nabla} e^{i\vec{k}.\vec{r} - i\omega t} \\ &= \vec{E}_0 \cdot i\vec{k} e^{i\vec{k}.\vec{r} - i\omega t} = 0. \end{aligned} \tag{2.12}$$

Thus we have (using a similar derivation for the magnetic field),

$$\vec{E}_0 \cdot \vec{k} = 0 \quad \text{and} \quad \vec{B}_0 \cdot \vec{k} = 0. \tag{2.13}$$

The result of Equation 2.13 requires that the electric and magnetic fields of a plane

wave be perpendicular to the propagation direction; the waves are transverse. Application of the Maxwell equations describing the curl of the electric field gives:

$$\begin{aligned} &\vec{\nabla} \times \vec{E}_0\, e^{i\vec{k}\cdot\vec{r} - i\omega t} + \frac{1}{c}\frac{\partial(\vec{B}_0\, e^{i\vec{k}\cdot\vec{r} - i\omega t})}{\partial t} \\ &= e^{i\vec{k}\cdot\vec{r} - i\omega t}\,\vec{\nabla} \times \vec{E}_0 - \vec{E}_0 \times \vec{\nabla} e^{i\vec{k}\cdot\vec{r} - i\omega t} - \frac{1}{c} i\omega \vec{B}_0\, e^{i\vec{k}\cdot\vec{r} - i\omega t} \\ &= -\vec{E}_0 \times i\vec{k} e^{i\vec{k}\cdot\vec{r} - i\omega t} - \frac{1}{c} i\omega \vec{B}_0\, e^{i\vec{k}\cdot\vec{r} - i\omega t} = 0 \end{aligned} \tag{2.14}$$

Thus,

$$\vec{E}_0 \times \vec{k} = -\frac{\omega}{c}\vec{B}_0 \tag{2.15}$$

Since $\vec{E}$ and $\vec{B}$ are perpendicular to $\vec{k}$, this result means that $\vec{E}$ and $\vec{B}$ are mutually perpendicular.

The most general plane wave solution of Equation 2.8 is

$$\vec{E} = (E_1\hat{e}_1 + E_2\hat{e}_2)\, e^{i\vec{k}\cdot\vec{r} - i\omega t}, \tag{2.16}$$

where $\hat{e}_1$ and $\hat{e}_2$ are unit vectors with directions perpendicular to each other and to $\vec{k}$ and E_1 and E_2 are complex allowing for a possible phase difference between them. The polarization of a electromagnetic wave is conventionally defined by the direction of the electric field vector. If E_1 and E_2 have the same phase, then the light is linearly polarized. Let, for example, $\vec{k} = k\hat{z}$, $E_2 = 0$, and $\hat{e}_1 = \hat{x}$. This describes a plane wave polarized along the x direction and travelling in the z direction. If $E_1 = E_0$ and $E_2 = iE_0$, the plane wave is circularly polarized; its electric field vector traces out a circle. To see this one applies the convention that the real electric field is the real part of Equation 2.16. This application yields:

$$\vec{E} = E_0\cos(\vec{k}\cdot\vec{r} - \omega t)\hat{e}_1 - E_0\sin(\vec{k}\cdot\vec{r} - \omega t)\hat{e}_2. \tag{2.17}$$

At a fixed position, the electric field vector traces out a circle. If the magnitude of the components of the wave defined by Equation 2.17 are not equal then the wave is

elliptically polarized. The ratio of the magnitudes of E_1 and E_2 define the ellipticity of the wave. The angle between the direction of $\hat{e}_1$ or $\hat{e}_2$ and a reference direction define the azimuth of the wave. At t=0, the real part of Equation 2.16 which describes the wave, becomes the equation for a helix:

$$\vec{E}(t=0) = E_1\cos(\vec{k}.\vec{r})\hat{e}_1 + E_2\sin(\vec{k}.\vec{r})\hat{e}_2. \qquad (2.18)$$

The handedness of this helix defines the handedness of the corresponding elliptical wave. The ellipsometric parameters: the handedness, ellipticity, the irradiance ($\vec{E}$. $\vec{E}$), and azimuth fully describe the polarization state of an electromagnetic wave.

The Stokes parameters are a more convenient way to describe light and its polarization than are the ellipsometric parameters. The Stokes parameters describe the degree as well as the type of polarization of light; they can describe unpolarized light whereas the ellipsometric parameters cannot. In addition, the Stokes parameters correspond to intensities of light and are thus directly measurable. The Stokes parameters (I, Q, U, V) can be operationally defined by a series of experiments in which the light is passed through different analyzers before reaching the detector. These experiments, described previously[40] are outlined below:

I. Total Intensity, I

If there is no analyzer the irradiance is

$$E_1E_1^* + E_2E_2^* \equiv I. \qquad (2.19)$$

II. Perpendicular *vs* Parallel Polarization, Q

In this experiment a polarizer oriented along $\hat{e}_1$ and then along $\hat{e}_2$ serves as an analyzer. A polarizer will transmit the component of the electric field that is parallel to its orientation. Therefore the irradiances measured at the detector for these two orientations of the polarizer are $E_1E_1^*$ and $E_2E_2^*$. The difference between these two

measured intensities defines Q:

$$Q \equiv E_1E_1^* - E_2E_2^* \tag{2.20}$$

III. Diagonal Polarization.

Two polarizers are oriented alternatively along the diagonal directions, $1/\sqrt{2}(\hat{e}_1 + \hat{e}_2)$ and $1/\sqrt{2}(\hat{e}_1 - \hat{e}_2)$. With the first orientation, the amplitude of the transmitted wave is $1/\sqrt{2}(E_1 + E_2)$. The irradiance of this transmitted wave is 1/2 $(E_1E_1^* + E_2E_2^* + E_1E_2^* + E_2E_1^*)$. For the second orientation of the polarizer the amplitude and irradiance of the transmitted wave will be $1/\sqrt{2}(E_1 - E_2)$ and 1/2 $(E_1E_1^* + E_2E_2^* - E_1E_2^* - E_2E_1^*)$. The difference between these two measured intensities defines U:

$$U \equiv E_1E_2^* + E_2E_1^* \tag{2.21}$$

III. Circular Polarization.

For the final experiment left and right circular polarizers are used as analyzers. The amplitudes of the transmitted waves using right and left circular polarizers are $\frac{1}{\sqrt{2}}(E_1 - iE_2)$ and $\frac{1}{\sqrt{2}}(E_1 + iE_2)$. The corresponding irradiances are 1/2 $(E_1E_1^* + E_2E_2^* - iE_1E_2^* + iE_2E_1^*)$ and 1/2 $(E_1E_1^* + E_2E_2^* + iE_1E_2^* - iE_2E_1^*)$. The difference between these two intensities defines V:

$$V \equiv i(E_1E_2^* - E_2E_1^*) \tag{2.22}$$

The stokes parameters completely describe the state and degree of polarization of light. The above discussion applies to monochromatic light, where E_1 and E_2 are constant in time. If E_1 and E_2 vary slowly in time with respect to $\frac{2\pi}{\omega}$, the light is called quasi-monochromatic and the electric field vector does not trace out a well defined ellipse. This light is partially depolarized. If $E_1(t)$ and $E_2(t)$ are completely

uncorrelated then the light is unpolarized. The stokes parameters can now be written:

$$\begin{aligned} I &= \langle E_l E_l^* + E_r E_r^* \rangle, \text{ total intensity of light,} \\ Q &= \langle E_l E_l^* - E_r E_r^* \rangle, \text{ linear polarization ,} \\ U &= \langle E_l E_r^* + E_r E_l^* \rangle, \text{ diagonal polarization ,} \\ V &= \langle i(E_l E_r^* - E_r E_l^*) \rangle, \text{ circular polarization,} \end{aligned} \tag{2.23}$$

where <> denotes a time average. It is convenient to form a 4 element vector using the stokes parameters to describe the state and degree of light. This vector has the form:

$$\begin{bmatrix} I \\ Q \\ U \\ V \end{bmatrix} \tag{2.24}$$

Some examples of Stokes vectors and the light they describe are:

$$\begin{bmatrix} 1 \\ 0 \\ 0 \\ 0 \end{bmatrix} \text{ Unpolarized} \quad \begin{bmatrix} 1 \\ 1 \\ 0 \\ 0 \end{bmatrix} \text{ Linearly Polarized along } \hat{e}_1 \quad \begin{bmatrix} 1 \\ -1 \\ 0 \\ 0 \end{bmatrix} \text{ Linearly Polarized along } \hat{e}_2$$

$$\begin{bmatrix} 1 \\ 0 \\ 1 \\ 0 \end{bmatrix} \text{ Linearly Polarized along } \frac{1}{\sqrt{2}}(\hat{e}_1 + \hat{e}_2) \quad \begin{bmatrix} 1 \\ 0 \\ 0 \\ 1 \end{bmatrix} \text{ Right Circularly Polarized} \tag{2.25}$$

A plane wave propagates continuously unless disturbed by a change in the properties of the surrounding medium. The encountered medium may have a different dielectric constant or it may contain particles characterized by different optical properties. When a change in the medium occurs, the propagation of the light can be altered; the light is scattered. Light scattering is a process whereby light is reradiated by a sample. Light is incident upon a sample (a particle, ensemble of particles, or fluid medium). The light excites the sample by causing local oscillations of the electric charges that compose the sample. These oscillating charges radiate. If the

oscillations, and hence the emitted radiation, have the same frequency (energy) as the incident light t! ,n this process of reradiation is called elastic scattering. In order to describe the scattered wave we must determine its electric field vector. We will assume the following properties within the scattering particles:

$$\vec{D} = \varepsilon_m \vec{E} + \overleftrightarrow{\varepsilon} \cdot \vec{E} \quad \vec{B}=\vec{H}, \tag{2.26}$$

where ε_m is the dielectric constant of the surrounding medium and $\overleftrightarrow{\varepsilon}$ is a tensor. Assuming that the temporal component of the field (which we will suppress) is still $e^{-i\omega t}$, the combination of the curl Maxwell equations gives:

$$\vec{\nabla} \times \vec{\nabla} \times \vec{E} - \frac{\omega^2}{c} \vec{D} = 0 \tag{2.27}$$

Writing $\vec{E}$ as $\frac{\vec{D}}{\varepsilon_m}\vec{E} - \frac{\overleftrightarrow{\varepsilon}}{\varepsilon_m} \cdot \vec{E}$ gives:

$$\nabla^2\vec{D} + k^2\vec{D} = -\vec{\nabla} \times \vec{\nabla} \times \overleftrightarrow{\varepsilon} \cdot \vec{E}, \tag{2.28}$$

where $k^2 = \frac{\varepsilon_m \omega^2}{c^2}$ Equation 2.28 is a wave equation with the source $\vec{\nabla} \times \vec{\nabla} \times \overleftrightarrow{\varepsilon} \cdot \vec{E}$. This equation has the integral form [65]

$$\vec{D} = \vec{D}^0 + \int dV \overleftrightarrow{G} \cdot \vec{\nabla} \times \vec{\nabla} \times \overleftrightarrow{\varepsilon} \cdot \vec{E}, \tag{2.29}$$

where $\overleftrightarrow{G}$ is the tensorial Green function, the integral is taken over the volume of the particle(s), and $\vec{D}^0$ refers to the initial electric displacement. We assume that the scattering is detected at a distance far from the scatterer where $\vec{D} = \varepsilon\vec{E}$. Using the appropriate Greens function Equation 2.29 becomes[66]

$$\vec{E}(\vec{r}) = \vec{E}^0(\vec{r}) + (\overleftrightarrow{1} - \hat{k}\hat{k})\, k^2 \frac{e^{i\vec{k}\cdot\vec{r}}}{r} \int dV\, e^{i\vec{k}\cdot\vec{r}} \overleftrightarrow{\alpha}_v \cdot \vec{E}(\vec{r}\,'), \tag{2.30}$$

where $\overleftrightarrow{\alpha}_v = \frac{\overleftrightarrow{\varepsilon}-\overleftrightarrow{1}}{4\pi}$ is the polarizability tensor per unit volume, and $\hat{k}\hat{k}$ refers to the outer product of the propagation vectors. The resultant field , $\vec{E}(\vec{r})$, is thus equal to the incident wave $\vec{E}^0$ plus the scattered wave. The scattered wave consists of a

spherical wave, $\frac{e^{i\vec{k}\cdot\vec{r}}}{r}$, multiplied by a scattering amplitude. The scattering amplitude results from the integration over the scattering particle(s) and incorporates (through the polarizability tensor) the properties of the scatterer. The electric field that appears within the integral over the volume of the particle refers to the internal electric field, that is the electric field within the scatterer. The scattered field can thus be viewed as the radiation field resulting from the sum of field amplitudes over the points (dipoles) within the particle. The term $\overleftrightarrow{I} - \hat{k}\hat{k}$ insures the transversality of the scattered wave.

Note that Equation 2.30 does not constitute a solution to Maxwells' equations. The electric field appears on both sides of the equation. The electric field inside the particle, the internal field, $\vec{E}(\vec{r})$ must be determined. The internal field is composed of a component due to the incident wave plus a component due to the reradiation from other points from within the particle. The simplest approach is to assign the internal electric field to be equal to the incident electric field. This assignment is known as the first Born approximation. The first Born approximation ignores the component of the internal field that results from reradiation from one part of the particle to another; it ignores secondary radiation and interactions within the particle. The first Born approximation is generally valid when the polarizability of the particle is relatively small. In this case the contribution to the internal field from internal radiation is small so the incident field dominates. The scattered field at a distance r from an incident plane wave using the first Born approximation is:

$$\vec{E}^s(\vec{r}) = k^2 \frac{e^{ikr}}{r} \int_{v'} \overleftrightarrow{\alpha}_v(\vec{r}\,') \cdot \vec{E}^0 \, e^{-i(\vec{k}-\vec{k}^0)\cdot\vec{r}\,'} \, dV', \qquad (2.31)$$

where $\vec{E}^0$ is the incident electric field vector, $\vec{k}$ and $\vec{k}^0$ are the propagation vectors

of the scattered and incident fields, and the transversality condition has been suppressed. We will continue to suppress the transversality condition from now on.

A more rigorous approach would include internal radiation. One such approach is the coupled dipole approximation. The coupled dipole approximation models a particle as a finite sum of point polarizable group or dipoles. The field from Equation 2.30 thus becomes:

$$\vec{E}^s(\vec{r}) = \vec{E}^0(\vec{r}) + \frac{e^{i\vec{k}\cdot\vec{r}}}{r}\sum_{j}^{N} e^{i\vec{k}_j\cdot\vec{r}_j}\overleftrightarrow{\alpha}_j \cdot \vec{E}_j, \tag{2.32}$$

where $\overleftrightarrow{\alpha}$ is the polarizability tensor with units of volume, N is the total number of dipoles and j is the index for each dipole. Each dipole is excited by the internal field and reradiates. The field at each dipole is equal to the incident field plus the field resulting from internal dipolar radiation due to the other dipoles. The field at the dipole i is given by: [40]

$$\vec{E}_i = \vec{E}_i^0\, e^{ikr_i} + \sum_{j\neq i}^{N} a_{ij}\overleftrightarrow{\alpha}_j\vec{E}_j + b_{ij}(\overleftrightarrow{\alpha}_j\vec{E}_j\cdot\hat{n}_{ij})\hat{n}_{ij}, \tag{2.33}$$

where

$$a_{ij} = \frac{e^{ikr_{ij}}}{r_{ij}}\left(k^2 - \frac{1}{r_{ij}^2} + \frac{ik}{r_{ij}}\right),$$

$$b_{ij} = \frac{e^{ikr_{ij}}}{r_{ij}}\left(-k^2 + \frac{3}{r_{ij}^2} - \frac{3ik}{r_{ij}}\right),$$

and r_{ij} is the distance between the i^{th} and j^{th} dipoles. When internal radiation is ignored then only the first term in Equation 2.33 need be included. This is equivalent to the first Born approximation applied to a set of point polarizable groups. To distinguish this application of the first Born approximation from that to a continuous structure we will refer henceforth to the independent dipole and continuous Born Models. The scattered field of Equation 2.32 can be rewritten in a

compact matrix form:

$$\vec{E}^s(\vec{r}) = \frac{k^2}{r} e^{ikr}(1 - \hat{k}\hat{k}) \sum_{ab}^{N} \overleftrightarrow{\Gamma}_{ab} \cdot \vec{E}_b \, e^{-i(\vec{k}\cdot\vec{r}_b - \vec{k}^0\cdot\vec{r}_a)}, \tag{2.34}$$

where

$$\overleftrightarrow{\Gamma}_{ab} = \overleftrightarrow{\alpha}_a \delta_{ab} + (1 - \delta_{ab}) \sum_{c=1}^{N} \overleftrightarrow{\alpha}_a \cdot \overleftrightarrow{\Gamma}_{ac} \cdot \overleftrightarrow{\Gamma}_{cb},$$

$$\overleftrightarrow{\Gamma}_{ac} = \frac{e^{ikr_{ac}}}{r_{ac}^3} [(1 - \hat{u}_{ac}\hat{u}_{ac})\,(kr_{ac})^2 + (3\hat{u}_{ac}\hat{u}_{ac} - 1)\,(1 - ikr_{ac})],$$

and $\hat{u}_{ac}$ is the unit distance vector from the a^{th} to the c^{th} dipole.

We refer to the formalism that accounts for interaction between dipoles as the coupled-dipole model. If a particle is modelled by N dipoles, 3xN linear equations must be solved simultaneously in order to determine the net electric field at each dipole location. The solution of the simultaneous equations to find the electric field at each dipole is the limiting problem with the coupled-dipole method. If the object is modelled by a large number of dipoles (more than 200) or averaging over many orientations of a given particle is desirable, a fast computer such as the CRAY is required. On the other hand, the calculations required for the first Born approximation can be done on a desk-top computer. The first Born approximation, however, does not include interactions between the dipoles. The importance of the interaction effects is determined by the interaction matrices, $\overleftrightarrow{\Gamma}_{ab}$.

A particle described by a set of point polarizable groups is characterized by the polarizability tensor at each point. A particle modelled by a continuous polarizability is characterized by a polarizability tensor that is a continuous function of position. This is equivalent to a description using an infinite number of point polarizable groups. The polarizability tensor is a 3x3 matrix that describes how the point polarizable groups respond to an external field. The polarizability tensor determines the

strength and direction of the induced dipole moment, $\vec{\mu}_d$.

$$\vec{\mu}_d = \overleftrightarrow{\alpha} \cdot \vec{E} \tag{2.35}$$

In the simplest case, the dipole moment will be parallel to the applied electric field. In this case the polarizability tensor is always diagonal and can be replaced by a scalar quantity. In general, a set of axes can always be found such that the polarizability tensor is diagonal along these axes. These are the principal axes of the polarizabilty. If the unit vectors along the principal axes ($\hat{t}$, $\hat{n}$, $\hat{p}$), are written in cartesian coordinates then the polarizabilty tensor will have be of the form

$$\alpha_{tt}\hat{t}\hat{t} + \alpha_{nn}\hat{n}\hat{n} + \alpha_{pp}\hat{p}\hat{p} \tag{2.36}$$

in cartesian coordinates where α_{tt}, α_{nn}, and α_{pp} are the polarizability strengths along each axis.

A dipole does not have dimensions in physical space. We have described a model where a set of dipoles represents a real particle. It is useful to imagine the particle as consisting of discrete subunits, each of which can be represented by a point polarizable group. This formulation is valid as long as the subunit is sufficiently small with respect to the wavelength. When the subunit becomes too big, it will no longer radiate in a manner similar to that of a single dipole. It is necessary to determine the polarizability tensor associated with each subunit. The most general smooth particle is an ellipsoid. The major and minor axes of the ellipsoid correspond to the principal axes of the polarizability. The strength of the polarizability along each principal axis depends on the shape and nature of the material it represents. If the material that makes up the subunit has an inherent isotropic polarizabilty then any anisotropy in the polarizability of the subunit will be due to its shape. For an ellipsoidal subunit composed of optically isotropic material,

$$\alpha_i = 4\pi\, p_{nn}\, p_{pp}\, p_{tt}\, \frac{\varepsilon_r}{3 + 3\, L_i\, \varepsilon_r} \qquad i = tt,\ nn,\ pp \tag{2.37}$$

where p_{nn} p_{pp} and p_{tt} are the lengths of the semi-minor and semi-major axes of the ellipsoid, and L_i is a geometrical factor defined by:[40]

$$L_i = \frac{p_{nn}\, p_{pp}\, p_{tt}}{2} \int_0^\infty \frac{dq}{(p_i^2 + q) f(q))} \qquad i = tt,\ nn,\ pp, \tag{2.38}$$

with

$$f(q) = [\ \sum_i (q + p_i)^2\ ]^{1/2}.$$

ε_r is related to the effective dielectric constant of the subunit, ε, and that of the surrounding medium ε_m by the relation:

$$\varepsilon_r = \frac{\varepsilon - \varepsilon_m}{\varepsilon_m}. \tag{2.39}$$

One must calculate the effective dielectric constant of the prolate ellipsoidal subunit. This quantity depends on the the bulk dielectric constant of the particle, ε_{avg}, that of the surrounding medium, ε_m, and the geometry of the subunit.[1,14]

$$\varepsilon_{avg} = \frac{(1-f)\, \varepsilon_m + f\beta\varepsilon}{1 - f + f\beta} \tag{2.40}$$

where

$$\beta = \frac{\varepsilon_m}{3} \sum_j \frac{1}{\varepsilon_m + L_j\, (\varepsilon - \varepsilon_m)} \qquad i = tt,\ nn,\ pp, \tag{2.41}$$

and f is a volumetric factor equal to $\pi/6$ for ellipsoids.

In practice, given ε_m, ε_{avg}, and the dimensions of the subunit, one solves Equations 2.40 and 2.41 for the effective dielectric constant of the subunit, ε. With this value the polarizability components can be calculated for each subunit from Equation 2.37. Changing the ratio $\varepsilon_{avg}/\varepsilon_m$ does not affect the calculated polarizabilities. Thus α_i is a function of the size and shape of the subunits, and the bulk dielectric

constant of the particle relative to the surrounding medium.

When the subunit is spherical, all the polarizability strengths are equal and α is of the form:

$$\overleftrightarrow{\alpha} = \begin{bmatrix} \alpha_s & 0 & 0 \\ 0 & \alpha_s & 0 \\ 0 & 0 & \alpha_s \end{bmatrix} = \alpha_s \overleftrightarrow{I}. \tag{2.42}$$

If the subunit is a prolate spheroid with the major axis along the $\hat{t}$ direction, then $p_{nn} = p_{pp} \rightarrow \alpha_{nn} = \alpha_{pp}$. If the material within the subunit is not optically isotropic Equation 2.37 must be modified. For an optically anisotropic sphere,

$$\alpha_j = 4\pi a_s^3 \frac{\varepsilon_j - \varepsilon_m}{\varepsilon_j + 2\varepsilon_m}, \; j = tt, \; nn, \; pp, \tag{2.43}$$

where ε_j is the strength of the dielectric constant along a principal axis. Thus an anisotropy in the polarizability tensor can arise due to a geometrically anisotropic subunit or a subunit composed of inherently optically anisotropic material.

In order to describe how the scattering process alters the polarization state of light it is useful to resolve the electric field into components that are parallel and perpendicular to the scattering plane. The scattering plane is defined by the incident and scattered propagation vectors. For a wave travelling in the z direction,

$$E^0 = (E_l^0 \hat{e}_l^0 + E_r^0 \hat{e}_r^0) e^{(ikz - i\omega t)}, \tag{2.44}$$

where $\hat{e}_l^0$ and $\hat{e}_r^0$ are unit vectors parallel and perpendicular to the scattering plane, k is the wave number and ω is the frequency of the incident light.

$$\hat{e}_r^0 = \frac{\hat{k} \times \hat{k}^0}{|\hat{k} \times \hat{k}^0|}, \quad \hat{e}_l^0 = \hat{k}^0 \times \hat{e}_r^0. \tag{2.45}$$

The relationship between the scattered and incident fields can be described by,

$$\begin{bmatrix} E_l^s \\ E_r^s \end{bmatrix} = \frac{e^{ik(r-z)}}{-ikr} \begin{bmatrix} S_2 & S_3 \\ S_4 & S_1 \end{bmatrix} \begin{bmatrix} E_l^0 \\ E_r^0 \end{bmatrix}, \tag{2.46}$$

where r is the distance from the scatterer to the detector and S_i (i = 1,2,3,4) define the scattering amplitude matrix.

$$\begin{bmatrix} E_l^s \\ E_r^s \end{bmatrix} = \begin{bmatrix} \hat{e}_l^s \\ \hat{e}_r^s \end{bmatrix} \cdot E^s, \tag{2.47}$$

where $\hat{e}_r^s = \hat{e}_r^0$ and $\hat{e}_l^s = \hat{k} \times \hat{e}_r^s$. It is more convenient to describe the scattering in terms of intensities. The Mueller scattering matrix relates the Stokes vectors of the incident and scattered light. This matrix is a property of the scattering medium and describes how the intensity and polarization state of light will be altered as a function of angle upon scattering. It is written as follows:

$$\begin{bmatrix} I^s \\ Q^s \\ U^s \\ V^s \end{bmatrix} = \frac{1}{k^2 r^2} \begin{bmatrix} S_{11} & S_{12} & S_{13} & S_{14} \\ S_{21} & S_{22} & S_{23} & S_{24} \\ S_{31} & S_{32} & S_{33} & S_{34} \\ S_{41} & S_{42} & S_{43} & S_{44} \end{bmatrix} \begin{bmatrix} I^i \\ Q^i \\ U^i \\ V^i \end{bmatrix}. \tag{2.48}$$

The Mueller matrix elements can be expressed as sums of products of the scattering amplitude matrix elements. The simple relationships between these quantities is given elsewhere.[40] Different elements of the Mueller scattering matrix are useful in describing various attributes of the scatterers, including symmetry, structure, chirality, optical properties, and orientation, in particular:

S11 - measure of the total scattered intensity for unpolarized incident light; gives general size information;

S12,S21 - measure of linear polarization parallel and perpendicular to the scattering plane; also gives size information;

S14 - measures depolarization of circular-polarized light or the differential scattering of right *vs* left circularly polarized light; indicates chirality or

orientation effects in the medium;

S13 - measure of linear polarization at 45° to the scattering plane, differential scattering of diagonally polarized light; indicates chirality or orientation effects in the medium;

S24 - measures transformation of circularly-polarized light to linearly-polarized light that is parallel or perpendicular to the scattering plane;indicates chirality or orientation effects in the medium;

S22, S44 - deviation of S22 from unity or S44 from S33 is indicative of non-spherical symmetry;

S34 - strongly dependent on size and complex refractive index of the particle, is a measure of changing circularly-polarized light to linearly-polarized light that is 45° to the scattering plane.

Optical symmetry is a function of composition as well as shape. Thus, it is possible to have an optically active or linearly birefringent sphere that does not have spherical symmetry with respect to the incident light. As the particle deviates from spherical symmetry, the complexity of the scattering matrix and its angular dependence increase. The Mueller matrix associated with a particular suspension of particles can be used to describe those particles. The simplest scattering matrix applies for particles much smaller than the wavelength of light or weakly-scattering particles

composed of isotropic material (*i.e.* the scattering is described by the Rayleigh or Rayleigh-Debye approximation). The off-diagonal elements with the exception of S12 and S21 of this matrix are zero:

$$\begin{bmatrix} S_{11} & S_{12} & 0 & 0 \\ S_{12} & S_{22} & 0 & 0 \\ 0 & 0 & S_{33} & 0 \\ 0 & 0 & 0 & S_{44} \end{bmatrix} \tag{2.49}$$

Perrin showed that, for an ensemble of randomly oriented particles (regardless of size), the elements in the off-diagonal blocks , S_{13}, S_{14}, S_{23}, and S_{24} and their transposes, are zero unless the particles contain some degree of chirality.[6] An ensemble of non-chiral particles will have no S_{14} (for example) unless there is some degree of partial orientation. The Mueller matrix of an ensemble of randomly oriented non-chiral particles will have the form:

$$\begin{bmatrix} S_{11} & S_{12} & 0 & 0 \\ S_{12} & S_{22} & 0 & 0 \\ 0 & 0 & S_{33} & S_{34} \\ 0 & 0 & -S_{34} & S_{44} \end{bmatrix} \tag{2.49}$$

The off-diagonal block elements are sensitive to the chiral properties of a sample and have thus been named helical domain elements.[38] They are thus well suited to the study of helical structures such as chromosomes.

III. Light Scattering from Helices

A. Introduction

In this chapter we evaluate the similarities, advantages, and disadvantages of a formalism based on the first Born approximation applied to a continuous helix *vs* formalisms that use a helix made of point polarizable groups when interactions between groups are either included or ignored. The comparisons are made for single helices at various orientations with respect to the incident light. The method involving the first Born approximation for the continuous helix is based on previous work by Bustamante et al.[27] These authors calculated the matrix elements S_{11} and S_{14} for single, continuous, thin helices either parallel or perpendicular to the incident light and for a collection of thin helices composed of point polarizable groups. Non-zero S_{14} resulted from using anisotropic polarizabilities. In the present work, all sixteen Mueller matrix elements are calculated, using the first Born approximation, for a single, continuous, thin helix at any orientation to the incident light. The results are compared to the those using the coupled dipole approximation method based on calculations by Singham *et al.*[41,43]

Using the coupled-dipole approximation, Singham *et al.* showed that modelling a single helix can be accomplished using spherical or prolate (anisotropic) subunits with equivalent results.[43] These authors also showed that, under certain conditions, interactions between dipoles can be ignored and a simpler theory, the first Born approximation could be used. In the present work, the conditions under which the interaction between dipoles can be ignored are further explored. In addition, the use of a continuous helix as a model, rather than one composed of individual dipoles, allows us to evaluate the number of dipoles necessary to accurately describe a helix.

We will begin with a generalized derivation of the Mueller scattering matrix in terms of the incident and scattered fields. The scattered electric field will then be calculated for a continuous helix using the First Born approximation. This model will be referred to henceforth as the continuous-Born model. We will compare the continuous-Born model to models that describe the helix by point-polarizable groups. When interactions between subunits are included the model is called the coupled-dipole model and when these interactions are ignored we will refer to the model as the independent-dipole model.

B. First Born Approximation on a Continuous Helix

For a continuous helix, we have from Equation 2.31:

$$\vec{E}_s(\vec{r}) = \frac{k^2}{r} e^{ikr} \int_v \overleftrightarrow{\alpha}(\vec{r}\,') \cdot \vec{E}^0 e^{-i(\vec{k}-\vec{k}^0)\cdot\vec{r}\,'} dV', \tag{3.1}$$

where the integral is taken over the volume of the particle. The helix, shown in Figure 3.1, is described by

$$\vec{r}\,' = a\cos(\theta)\,\hat{x} + a\sin(\theta)\,\hat{y} + \frac{P\theta}{2\pi}\,\hat{z}, \tag{3.2}$$

where a is the radius and P is the pitch. The polarizability tensor is defined in terms of components with unit vectors tangent (t), parallel(p), and perpendicular(n) to the helix:

$$\overleftrightarrow{\alpha} = \alpha_{tt}\,\vec{t}\vec{t} + \alpha_{nn}\,\vec{n}\vec{n} + \alpha_{pp}\,\vec{p}\vec{p}, \tag{3.3}$$

where,

$$\begin{aligned}
\vec{t} &= -\left(\frac{a}{M}\right)\sin(\theta)\,\hat{x} + \left(\frac{a}{M}\right)\cos(\theta)\,\hat{y} + \left(\frac{P}{2\pi M}\right)\hat{z} \\
\vec{p} &= \left(\frac{P}{2\pi M}\right)\sin(\theta)\,\hat{x} - \left(\frac{P}{2\pi M}\right)\cos(\theta)\,\hat{y} + \left(\frac{a}{M}\right)\hat{z} \\
\vec{n} &= \cos(\theta)\,\hat{x} + \sin(\theta)\,\hat{y}
\end{aligned} \tag{3.4}$$

with,

$$M = (a^2 + \frac{P^2}{4\pi^2})^{\frac{1}{2}}. \tag{3.5}$$

The integral in Equation (3.1) to be performed is then,

$$\int_0^{2\pi l} \vec{\alpha} \cdot \vec{E}^0 \, e^{i(\vec{k}-\vec{k}^0).\vec{r}'} \, d\theta \tag{3.6}$$

where the volume integral has been converted to an integral over the parameter θ, which, thru Equation (3.2), defines the position along the helix. For a randomly oriented helix, we must rotate $\vec{\alpha}$ and $\vec{r}'$:

$$\vec{r} \rightarrow \vec{r}(\vec{\omega}) = \vec{\vec{R}}(\vec{\omega}).\vec{r}' \text{ and } \vec{\alpha} \rightarrow \vec{\alpha}(\vec{\omega}) = \vec{\vec{R}}.\vec{\alpha}.\vec{\vec{R}}^{-1}, \tag{3.7}$$

where $\vec{\vec{R}}(\vec{\omega})$ is the Euler rotation matrix defined by the Euler angles represented by $\vec{\omega}$. Let this be written:

$$\vec{\vec{R}}(\vec{\omega}) = \begin{bmatrix} a_1 & a_2 & a_3 \\ b_1 & b_2 & b_3 \\ c_1 & c_2 & c_3 \end{bmatrix}. \tag{3.8}$$

The exponential term, $(\vec{k}-\vec{k}^0).\vec{r}'$ can be written as

$$\begin{aligned} &[(aa_1\cos(\theta) + aa_2\sin(\theta) + \frac{P\theta}{2\pi}a_3)(k_x - k_x^0)] + \\ &[(ab_1\cos(\theta) + ab_2\sin(\theta) + \frac{P\theta}{2\pi}b_3)(k_y - k_y^0)] + \\ &[(ac_1\cos(\theta) + ac_2\sin(\theta), + \frac{P\theta}{2\pi})(k_z - k_z^0)]. \end{aligned} \tag{3.9}$$

The integrand then becomes,

$$\vec{\alpha}(\vec{\omega}) \cdot \vec{E}^0 \, f(\theta) \tag{3.10}$$

where

$$\begin{aligned} f(\theta) &= e^{i(\rho\cos(\theta) + \sigma\sin(\theta) + \tau\theta)}, \\ \rho &= a(a_1(k_x - k_x^0) + b_1(k_y - k_y^0) + c_1(k_z - k_z^0)), \\ \sigma &= a(a_2(k_x - k_x^0) + b_2(k_y - k_y^0) + c_2(k_z - k_z^0)), \end{aligned} \tag{3.11}$$

$$\text{and } \tau = \frac{P}{2\pi}(a_3(k_x - k_x^0) + b_3(k_y - k_y^0) + c_3(k_z - k_z^0)).$$

Let's define :

$$\tan(\Lambda) = \frac{\sigma}{\rho} \text{ and } L^2 = \rho^2 + \sigma^2. \tag{3.12}$$

Then the integrand becomes,

$$\overleftrightarrow{\alpha}(\varpi) \cdot \vec{E}^0 \, g(\theta) \tag{3.13}$$

where

$$g(\theta) = e^{i(L\cos(\Lambda - \theta) + \tau\theta)} \tag{3.14}$$

We can expand the exponential term as a sum of Bessel functions. Using

$$e^{A\cos(\theta)} = \sum_{n=-\infty}^{\infty} J_n(A)\, e^{-in(\theta - \frac{\pi}{2})} \tag{3.15}$$

we can write the integral as,

$$\sum_{n=-\infty}^{\infty} J_n(L)\, e^{-in(\Lambda - \frac{\pi}{2})} \int_0^{2\pi l} \overleftrightarrow{\alpha}(\varpi) \cdot \vec{E}^0 \, e^{i(n+\tau)\theta} \, d\theta, \tag{3.16}$$

where J_n is the nth order Bessel function.

The integral of Equation (3.16) is straight-forward and has been carried out using Mathematica. The Mathematica code, Int, available from Dr. Arlon Hunt at Lawrence Berkeley Laboratory, carries out this integral. The evaluated integral can be used to calculate the Jones matrix elements (Equation 2.46). A direction is chosen for the incoming and scattered fields with components with respect to the scattering plane. This leads to the solution of Equation (2.46). The Jones Matrix elements lead directly to the Mueller matrix elements.

A fortran code was written to calculate the Mueller matrix elements using the formalism developed above. This code, Ghel is available from Dr. Arlon Hunt at

Lawrence Berkeley Laboratory. The input parameters are the euler angles defining the orientation of the helix, the length, pitch, the polarizabilities (α_{tt},$\alpha_{nn} = \alpha_{pp}$), and radius of the helix and the wavelength of the light. The output is the Mueller matrix elements as function of angle. The results for S_{11} and S_{14} agreed with those published previously for a helix oriented perpendicular to the incident light.[28,29] The asymmetry in these elements for $\phi \neq \pi/2$ observed by Bustamante *et al.* (the phenomenon known as anomalous scattering) was also seen to occur in the other matrix elements. Anomalous scattering occurs when the wavelength of light is within an absorption band of the scatterer. The phenomenon is observed in x-ray crystallography as an asymmetry in the diffraction pattern above and below the equator about the forward direction.[67]. With the scattering geometry described in Figure 3.2, light scattered off of the equator (the y-z plane) is described by an angle $\phi \neq \pi/2$. When ϕ is a constant $\neq$ an integer multiple of $\pi/2$, then the scattered light traces out a cone as a function of ψ (see Figure 3.2). The Mueller matrix elements are asymmetrical about the direction defined by $\psi = 0$ when measured on this cone. This is illustrated in Figure 3.3 For the rest of the calculations presented in this work, the azimuthal angle is set to $\pi/2$ for all the results shown, so that the Mueller matrix elements are calculated *vs* scattering angle.

C. Comparison of the Continuous Model and the Discrete Model

The calculation based on the continuous helix using the first Born approximation, can be used to evaluate the number of dipoles needed to accurately describe a given helix in the discrete case. Different results from this approach, referred to henceforth as the continuous-Born model, and those from a model using non-

interacting dipoles, the independent-dipole model, are due to an insufficient number of dipoles used in describing the helix. Figure 3.4 shows that as the number of dipoles on the helix increases, there is eventual convergence between the continuous-Born model, and the independent-dipole model. We have found that the continuous-Born and the independent-dipole models always converge when a sufficient number of dipoles are used in the discrete case. (The agreement in Figure 3.4 between the independent-dipole model and the coupled dipole model shows that for this case, interaction between dipoles need not be included). In order to use a comparison between these two models to evaluate the number of dipoles necessary to model the helix, several factors have to be considered. The ends of the continuous helix must coincide with the ends of the first and last subunit of the discrete helix. The subunits must be evenly placed along the helix although small spaces between the subunits does not produce a large effect. When modelling a helix with multiple turns, the subunits on each turn should be in phase with those on the next turn. The normalized [by S_{11}] matrix elements calculated from both models using the Born approximation are unaffected by a change in the absolute magnitude of the polarizability. Therefore, these two models need only use polarizability components that have the same ratio α_{tt}/α_{nn} as that used in the coupled-dipole approximation. Singham *et al.* have established that the number of subunits be such that their width be one tenth and their length be one fifth the incident wavelength or smaller.[43] We find these conditions to be applicable in most, but not all, cases. For helices large compared to the wavelength, stricter conditions apply.

The differences between the results from the continuous-Born and the independent-dipole models may incorrectly be interpreted as differences between an

infinitely thin and a thicker helix. In the independent and coupled-dipole models, the helix is modelled by placing prolate spheroidal subunits end to end along the helical lattice. The thickness of the helix is given by the width of the subunit. Using longer subunits results in modelling a thinner helix. In order to fit more subunits on a given lattice, smaller subunits must be used. Therefore, a helix made of subunits with a particular aspect ratio (d/w) is thinner when more subunits are used. This implies that the continuous helix, which could be interpreted to be composed of an infinite number of subunits, is infinitely thin. In fact, the thickness of the helix, for all the models, is related to the components of the polarizability perpendicular to the helix as shown in equations 27-31. The assignment of a polarizability perpendicular to the helix results in modelling a helix of a particular thickness. An infinitely thin helix is one that has a polarizability that is defined only tangent to the helix. The falsity in the contention that differences in the predictions made from the independent-dipole and continuous-Born models is due to differences in the thickness of the helix modelled is illustrated in Figure 3.4. The two models show reasonable agreement for a helix that is 50 nm thick (1/20 the wavelength of light), and excellent agreement for a helix 25 nm thick. If the continuous helix truly represents an infinitely thin helix, it is surprising that it is equivalent to helices of such large thicknesses compared to the wavelength of light. Figure 3.5 shows the results of calculations using the three approaches for a much thinner helix than the one used for Figure 3.4. The helix used in Figure 3.5 is composed of subunits that are about 200 times longer than they are wide, whereas in Figure 3.4, the subunits used are 4 times longer than they are wide. The length of the sub units used for both figures are the same. It might be expected that, since the helix in Figure 3.5 is so thin, that there would

always be agreement between the continuous-Born and the independent-dipole models. In Figure 3.5b the subunits used are 1 nm thick (1/1000 the wavelength of light) yet the difference between the two Born models is comparable to that in Figure 3.4b where the helix is fifty times thicker. We therefore conclude that differences between the two Born models are due to an insufficient number of dipoles used to model the helix and not due to a difference in the thickness of the helix.

Among the three models, the continuous-Born model may be best suited to describe the light scattering from helices that are larger than the wavelength of light, given current computer technology. Figure 3.6 shows scattering intensities from calculated for a helix that that has a radius and pitch that is 5 times the wavelength of light. The subunits used are about 1/10 the wavelength in length and 1/2000 the wavelength in width. When the helix is oriented at 45° to the incident light, calculations using the continuous-Born and discrete models differ significantly (Figure 3.6a). These differences are not seen when the incident light is perpendicular to the helix (Figure 3.6b). If the number of dipoles used for Figure 3.6 (360) is increased, the results of the discrete model calculations converge very slowly to those of continuous-Born model. The results shown in Figures 3.4 and 3.5, where the geometrical parameters of the helix are about equal to the wavelength of light, are consistent with these conditions set forth by Singham *et al.* that the subunits be less than or equal to 1/10 in width and 1/5 in length the wavelength of light. Figure 3.6a demonstrates, however, that these conditions do not always apply to larger helices.

D. The Necessity of Including Interactions

As stated at the end of section III, the importance of including dipolar interactions is determined by the interaction matrix $\overleftrightarrow{\Gamma}_{ab}$. Dipolar interactions need not be considered when $\overleftrightarrow{\Gamma}_{ab}$ calculated with the inclusion of these interactions is not significantly different from $\overleftrightarrow{\Gamma}_{ab}$ calculated when these interactions are ignored. It would be very difficult to calculate an analytical expression for the interaction matrices of a system composed of numerous dipoles. To investigate the importance of including dipolar interactions we have calculated the interaction matrices for a system composed of two dipoles. We use the result of the analytical expression obtained in this calculation to establish practical guidelines for the importance of including dipolar interactions when calculating the Mueller matrix for helices. The two dipoles, having polarizabilities whose strengths along the principle axes are given by (p1,p2,p3) and (q1,q2,q3) respectively, are placed on the z axis a distance d apart. The directions of the principal axes of the polarizabilities are chosen to be parallel to the coordinate system axes. For this system, there are four 3 x 3 interaction matrices, $\overleftrightarrow{\Gamma}_{11}$, $\overleftrightarrow{\Gamma}_{12}$, $\overleftrightarrow{\Gamma}_{21}$, and $\overleftrightarrow{\Gamma}_{22}$. Let the interaction matrices that are calculated when dipolar interactions are ignored be denoted as $\overleftrightarrow{\Gamma}^0_{ab}$ and those that allow for dipolar interactions be denoted $\overleftrightarrow{\Gamma}^1_{ab}$. Then the inclusion of dipolar interactions is unnecessary when $\overleftrightarrow{\Gamma}^0_{ab} \cong \overleftrightarrow{\Gamma}^1_{ab}$. We find that subtracting these two matrices gives terms of the form:

$$\delta \frac{\kappa}{(1-\kappa)}, \tag{3.17}$$

where

$$\kappa = p_j \frac{q_j}{d^6} \; (\; 1 + F(iKd) \;); \tag{3.18}$$

j = 1-3; δ is a multiplicative factor approximately equal to d^3, p_i or q_i; and F(iKd) is

a polynomial in terms of iKd. The condition for ignoring interaction becomes $\kappa << 1$. Since Kd must be small (that is a subunit must be smaller than the wavelength) we find that dipolar interactions can be ignored when

$$\frac{p_j^{max}}{d^3} \ll 1, \tag{3.19}$$

where p_j^{max} is the largest component of the polarizabilities.

The condition derived above (Equation 3.19) serves to quantify the contributions of dipolar interactions. Computations of $\alpha_{tt}(p_j^{max})$ using the formalism described in section V show that for longer subunits the denominator in the ratio of Equation 3.19, d^3, increases faster than the numerator. Thus Equation 3.19 can always be satisfied as long as sufficiently long subunits are used. Therefore, the inclusion of dipolar interactions is unnecessary when sufficiently long subunits are used to model a single stranded helix. The ratio in Equation 3.19 is a function of $\varepsilon_{avg}/\varepsilon_m$, and the shape of the subunits used. For each value of $\varepsilon_{avg}/\varepsilon_m$, a minimum aspect ratio (length/width) of the spheroidal subunits can be defined where interaction can be ignored. Singham *et al.* found that when $\varepsilon_{avg}/\varepsilon_m$ is 0.4 or less that the subunits must be at least 4 times longer than their width in order to ignore interactions. Singham's results translate into the condition .

$$\frac{\alpha_{tt}}{d^3} \leq 0.002, \tag{3.20}$$

when applied to Equation 3.19. Using this criterion and the ratio in Equation 3.19, we found approximate values of the minimum aspect ratio of the subunits needed to ignore dipolar interactions. The results are shown in Table 3.1 This table provides guidelines for deciding whether dipolar interactions are necessary when conducting light scattering calculations on helices.

Conditions for Ignoring Dipolar Interactions	
$\varepsilon_{avg}/\varepsilon_m$	Minimum Aspect Ratio
1.1	2:1
1.2	3:1
1.4	4:1
1.6	5:1
1.8	6:1

Table 3.1 The minimum aspect ratios are shown for the subunits used to model a helix when dipolar interactions could be ignored as a function of relative dielectric constant.

Figure 3.7 illustrates that dipolar interactions can be ignored for a given aspect ratio of the subunits used to describe the helix when a smaller relative dielectric constant is used. When $\varepsilon_{avg}/\varepsilon_m$ = 1.4 and subunits with an aspect ratio of 2:1 are used, dipolar interactions must be included to accurately calculate the Mueller matrix elements (Figure 3.7a). In these plots, a sufficient number of dipoles were used so that the calculations from the two Born models agree reasonably well. Even when the number of subunits is doubled, there are still significant differences between the coupled-dipole formalism and the Born models when the relative dielectric constant is 1.4 (Figure 3.7a S_{14}/S_{11} plot). When a lower relative dielectric constant is used for a similar helix, dipolar interactions become less important (Figure 3.7b). **E. Discussion**

The entire Mueller matrix has been calculated for a continuous helix using the first Born approximation. Results are shown for S_{14}, S_{11}, S_{34}, and S_{12} but the results for the other twelve elements are calculated in our fortran code. The analytical solution can be applied to a single helix at any orientation with respect to the incident light. Differences in the results from calculations using this continuous-Born model and the independent-dipole model reflect an insufficient number of discrete subunits used to represent the helix. A comparison between these models can therefore be used to determine how many dipoles are needed to describe different helices. For large helices compared to the wavelength of light, many dipoles are needed to accurately calculate the Mueller matrix elements. The limit of the number of dipoles using current supercomputers is 2000 when dipolar interactions are included. Therefore, when the pitch and radius of the helix are larger than the wavelength of light, the continuous-Born model may yield the best results. In general, the continuous-Born model is least computer intensive. The coupled-dipole model, by including dipolar interactions, is the most rigorous solution. When computational power is not a consideration, the coupled-dipole approximation will always yield the best results.

The importance of including dipolar interactions when calculating the Mueller matrix elements of a single stranded helix is dependent on the relative dielectric constant of the helix and the aspect ratio of the subunit used to model the helix. For larger relative dielectric constants, larger aspect ratios are necessary to ignore interactions. This results in being limited to modelling thinner helices in order to guarantee that the dimensions of the subunits of the helix be sufficiently small relative to the wavelength of light. For small relative dielectric constants, where the aspect ratio can be 2:1 without the need to include dipolar interactions, one can ade-

quately model a helix 1/10 the wavelength of light in thickness without having to include dipolar interactions. Table 1 gives a practical guide to the minimum aspect ratio, and hence maximum thickness, of a helix that can be modelled without including interactions.

Dipolar interactions become more important when modelling thicker structures. A helix that is of a thickness of the order of the wavelength of the light must be modelled with several strands. Attempts made in this investigation to define triaxial polarizabilities to compensate for dipolar interactions between strands in the same way that biaxial polarizabilities compensate for interactions along a single strand did not work. Unfortunately, the number of subunits needed per strand to accurately describe the helix probably does not decrease as more strands are introduced. Thus, the application of the coupled-dipole approximation to thicker helices requires a lot of computer power.

It is known that for any ensemble of randomly-oriented particles, S_{34}, S_{13}, S_{23} and their transposes are zero in the first Born approximation.[33] S_{34} appeared to agree well in all our comparisons between first Born approximation models and the coupled-dipole formalism made for thin helices. This implies that S_{34} will be zero in the orientational average for these single stranded helices even when dipolar interactions are included. Dipolar interactions contribute to the light scattering from thicker helices for a given relative dielectric constant. S_{34} may therefore be largely dependent on the thickness of a particle. This is consistent with the sucess of using S_{34} to size bacteria populations.[56]

In summary, we find that as the number of subunits increases the results of calculations using the independent-dipole model approach those using the continuous-

Born model. The continuous Born model could thus be used to evaluate the number of dipoles needed to accurately describe a helix. When dipolar interactions are found unnecessary, a comparison between the continuous-Born model and the coupled-dipole approximation could be used to determine the necessary number of dipoles. Equations 3.19 and Equation 3.20 describe the importance of including dipolar interactions. Table 3.1 can be used to establish when dipolar interactions can be ignored for materials with different dielectric constants and thicknesses. These results provide useful information that can be used towards a working theory of polarized light scattering from helices.

IV. The Nephelometer

In this chapter we will describe the instrument used to measure the Mueller matrix elements, the angular scanning, polarization-modulation nephelometer. This instrument was developed in 1973.[16] A sketch of the apparatus is shown in Figure 4.1. An argon-ion laser operates at wavelengths of 457, 488, and 514 nm. The laser produces a beam that is reflected by two mirrors and then traverses a polarizer followed by the photoelastic modulator (PEM). The beam is then incident upon the sample. Scattered light is detected by a photomultiplier tube mounted on a movable arm. Various analyzers housed in the arm allow all of the Mueller matrix elements to be measured.

The two mirrors are concave-spherical and can be rotated in three dimensions so that the height of the horizontal beam can be adjusted. A diaphragm is placed before the housing of the scattering cell to reduce the beam size. The Stokes vectors for the light after passing though the polarizer oriented at 0° and 45° with respect to the scattering plane are:

$$\begin{bmatrix}1\\1\\0\\0\end{bmatrix} \text{ and } \begin{bmatrix}1\\0\\1\\0\end{bmatrix} \tag{4.1}$$

giving horizontally and diagonally polarized light.

The heart of the instrument is the photoelastic modulator. It consists of piezoelectric quartz crystal fused to a piece of amorphous quartz. The piezoelectric crystal is driven by an electric field at a characteristic frequency (50 KHz). The amorphous quartz is stressed at this frequency. The photoelastic modulator thus acts like a retarder whose strain is modulated at 50 Khz. In one set up, (Set Up 1) hor-

izontally polarized light traverses the modulator oriented at 45° to the scattering plane. This yields:

$$\begin{bmatrix} 1 \\ \cos(\delta_s) \\ 0 \\ \sin(\delta_s) \end{bmatrix} = \begin{bmatrix} 1 & 0 & 0 & 0 \\ 0 & \cos(\delta_s) & 0 & -\sin(\delta_s) \\ 0 & 0 & 1 & 0 \\ 0 & \sin(\delta_s) & 0 & \cos(\delta_s) \end{bmatrix} \begin{bmatrix} 1 \\ 1 \\ 0 \\ 0 \end{bmatrix} \tag{4.2}$$

where we have normalized the Stokes vectors by their total intensity, and δ_s is the strain of the retarder. Here,

$$\delta_s = A_s \sin(\omega_p t), \tag{4.3}$$

where A_s is the amplitude of the strain, dependent on the thickness of the quartz, the stress of the quartz, and the wavelength of light and ω_p is the frequency of modulation. The light emerging from the photoelastic modulator can be described by (writing only the first terms in a Bessel series expansion):

$$\begin{bmatrix} 1 \\ J_0(A_s) + 2\, J_2(A_s)\cos(2\omega_p t) + \cdots \\ 0 \\ 2\, J_1(A_s)\sin(\omega_p t) + \cdots \end{bmatrix} \tag{4.4}$$

A horizontal and vertical polarizer are used as analyzers to eliminate the J_0 term. The measured intensities,with these analyzers, are:

$$1+J_0(A_s) + 2\, J_2(A_s)\cos(2\omega_p t) + \cdots \quad \text{and} \quad 1-J_0(A_s) + 2\, J_2(A_s)\cos(2\omega_p t) + \cdots \tag{4.5}$$

The signal from the photomultiplier tube is sent to a lockin amplifier set at $2\omega_p$. A feedback circuit acts to keep the DC current constant. The lock-in signals are then:

$$\frac{2\, J_2(A_s)\cos(2\omega_p t)}{1 + J_0(A_s)} \quad \text{and} \quad \frac{2\, J_2(A_s)\cos(2\omega_p t)}{1 - J_0(A_s)}. \tag{4.6}$$

The amplitude of the strain, A_s, is adjusted so that the two signals from cross polarizers are equal; $J_0(A_s) \rightarrow 0$. When no analyzer is used, and A_s is so adjusted, a scattering measurement gives:

$$S_{11} + 2\,S_{12}\,J_2(A_s)\cos(2\omega_p t) + 2\,S_{14}\,J_1(A_s)\sin(\omega_p t) + \cdots \quad (4.7)$$

Using the feedback circuit and setting the lock-in amplifier at ω_p gives the signal $\frac{2\,S_{14}\,J_1(A_s)}{S_{11}}$. Setting the lock-in at $2\omega_p$ gives $\frac{2\,S_{12}\,J_2(A_s)}{S_{11}}$. Measuring the DC signal from the PMT gives S_{11}. The other elements are obtained in combination with the above with the use of several analyzers. For example, using a diagonal polarizer, and setting the lock-in amplifier to ω_p, gives the signal $\frac{2\,(S_{14} + S_{34})\,J_1(A_s)}{S_{11} + S_{31}}$. In order to obtain a measurement of S_{34} a deconvolution must be carried out with S_{14} and S_{31}. When horizontally polarized light is incident on the modulator oriented at 45°, one can measure S_{11}, S_{12}, S_{14}, S_{22}, S_{24}, S_{32}, S_{34}, S_{42}, and S_{44}.

The elements in the third column of the Mueller matrix can be measured by sending diagonally polarized light through a horizontal photoelastic modulator. The intensity of scattered light, when no analyzer is used, can be written

$$S_{11} + 2\,S_{13}\,J_2(A_s)\cos(2\omega_p t) + 2\,S_{14}\,J_1(A_s)\sin(\omega_p t) + \cdots \quad (4.8)$$

Thus, in this set up (Set up 2), the elements in the third column of the Mueller matrix are measured in the same way as those in the second column when the modulator is at 45°.

Three normalization constants are required: one for DC measurements, one for measurements at ω_p and one at $2\omega_p$. The DC normalization, used for S_{11}, is obtained by measuring the DC signal from the light scattered by carbon disulfide at a scattering angle of 90° for a given voltage across the photomultiplier tube. Carbon disulfide is a liquid that, due to its high density and asymmetric geometry scatters quite efficiently. Its availability makes it a good standard. The normalization for the $2\omega_p$ elements is taken by using a horizontal or vertical polarizer as an analyzer.

The gain and sensitivity are set and the value of the signal on the lock-in set at $2\omega_p$ recorded. This value is the value of S_{12} of a perfect linear polarizer, that is it is 100% of S_{11}. The ω_p elements are normalized in a similar way except the lock-in is set at ω_p and the analyzer used is a circular polarizer (a 1/4 wave plate followed by a vertical polarizer).

Several treatments of problems arising in polarized light scattering and related measurements have been given.[64,68-70] If the angle of the photoelastic modulator or the initial polarizer is not set carefully, measurements of mixed elements will result. We have found that internal reflections within the PEM element cause unwanted mixing of the measured Mueller matrix elements. These reflections can be avoided by rotating the PEM about 15° about the vertical direction. Other artifacts arise due to a strain induced by the front window of the scattering cell. This can be compensated for by placing a strain plate such as a microscope slide after the modulator. With proper alignment most of these artifacts can be minimized.

Proper alignment of the nephelometer begins with the examination of the polarization state of the light. The polarization state of the light exiting the initial polarizer can be checked using cross polarizers as analyzers. The polarization state of the modulated light is checked at ω_p and $2\omega_p$. The angle of the modulator head can be adjusted to minimize unwanted polarizations. When horizontally polarized light is passed through the modulator at 45° (Set Up 1), the desired polarization state is of the form $(1, A\cos(2\omega_p t), 0, B\sin(2\omega_p t))$. Thus when the lock-in amplifier is set at $2\omega_p$, there should be no signal when a diagonal polarizer, or a circular polarizer are used as an analyzer. When the lock-in amplifier is set at ω_p, there should be no signal when a vertical or diagonal polarizer is used as an analyzer. There should

never be any signal from the lock-in amplifier when no analyzer is used. Unfortunately, due to residual strain in the PMT, discussed previously,[69] unwanted polarizations are always present to some degree. In our instrument we have made the following measurements on the lock-in amplifier for Set Up 1:

analyzer	**lock-in setting**	**reading**
vertical	$2\omega_p$	0.96
diagonal	$2\omega_p$	0.01
circular	$2\omega_p$	0.02
none	$2\omega_p$	0.02
vertical	ω_p	0.001
diagonal	ω_p	0.003
circular	ω_p	0.54
none	ω_p	0.0002

The results tabulated above give a minimum amount of Mueller matrix element mixing that can occur during measurement. When the lock-in amplifier is set at $2\omega_p$, the normalization constant is 0.96. There will be a mixing of $\frac{0.01}{0.96}$ of third column elements when measuring second column elements. Thus when measuring S_{12} (no analyzer present), about 1% of S13 will be mixed in. This is not a large artifact since S_{13} is much smaller than S_{12}. The mixing when the lock-in amplifier is set at ω_p is not as great as when it is set at $2\omega_p$. Thus when S_{14} is measured, only about 0.2% of S_{12} is mixed in. It may be more desirable to measure small Mueller matrix elements, such as those in the helical domain, with the lock-in set at ω_p rather than $2\omega_p$. Using Set Up 2, the small element, S_{13}, is measured at $2\omega_p$. If this set up is

modified so that circularly polarized rather than diagonally polarized light is used then S_{13} can be measured at ω_p.

The instrument's alignment is tested by taking measurements on standard samples such as latex spheres. These measurements can be compared to theoretical predictions from Mie theory. It is desirable to make measurements on both Rayleigh and larger size spheres. The measured S_{14} on 0.497μ spheres should be zero. In our measurements, reported in the next chapter, the S_{14} from these spheres was less than 0.3%. Thus our measurements of S_{14} have an uncertainty of 0.3%. Comparisons of measurements using our instrument made on spheres and calculations based on Mie theory are reported elsewhere.[53,71]

V. Determination of the Direction of DNA in the Octopus Sperm Head

A. Introduction

Polarized light scattering has been in use as a biophysical tool for many years.[17,26] In particular, the Mueller scattering matrix element, S_{14}, (also known as circular intensity differential scattering, CIDS) promised to be useful to study helical structures.[23] Yet the lack of good data combined with the complexity of the theory of polarized light scattering from helices has limited its application to specific questions in structural biology. Very few attempts have been made to compare theoretical predictions with measured results of polarized light scattering from helical structures. Mie calculations, which offer an exact solution for spherical particles, show good agreement with experimental data taken on samples of spherical marine algae.[53] Unfortunately, there is no exact solution that describes polarized light scattering from helical structures.

A reasonably successful study involving both measurements and theoretical predictions of polarized light scattering from helices was carried by Wells et al.[64] This group compared a relatively simple theory based on the first Born approximation to measurements of S_{14} on octopus sperm heads, of the species *Eledone cirrhosa*. The large S_{14} of this sample was originally discovered by Maestre *et al.*[54] Despite the success of the Wells group to model S_{14}, we will show that the Born approximation does not predict some of the other Mueller scattering matrix elements for the sperm head as well. For example, S_{34} is predicted to be identically zero when the Born approximation is used, even though a significant S_{34} is measured.[33] Furthermore, the first Born approximation can not be used characterize the polarizability of the material being modelled. All normalized Mueller matrix elements,

calculated in the first Born approximation, depend only on the degree of anisotropy of the polarizability, not on its absolute strength. Thus it is difficult to ascertain the polarizability strength of a material when using calculations based on the first Born approximation. When the polarizability is isotropic, calculations involving the first Born approximation predict a null S_{14}. Helical structures are modelled using anisotropic polarizabilities whenever the first Born approximation is used in order to obtain non-zero values of S_{14} which are theoretically predicted and experimentally measured for these structures.[28] The anisotropy applied in this way does not necessarily represent an inherent anisotropy in the polarizability of the material being modeled. Finally, the first Born approximation cannot be applied to thick structures. Due to the limitations of the first Born approximation we have used the coupled-dipole approximation to model polarized light scattering data from the sperm heads. This application allows us to determine the direction of an inherent anisotropy in the polarizability in the sperm head and hence determine the direction of the DNA.

In this chapter we apply a formulation of the coupled-dipole approximation in the orientation average [34] to model measurements made on the helical octopus head. An inherent anisotropy in the polarizability allows for an investigation of the nature of DNA packing. The model is limited by the computational power necessary to model a structure composed of many subunits. The sperm head is approximated by a single turn of a helical fiber composed of spherical subunits. The thickness of the fiber in the model is significantly thinner than a corresponding chromatin fiber in the sperm head. Despite the limitations of the model, reasonable agreement with experimental measurements is obtained. The results indicate that the 2 nm DNA double helices are packed with the their axes perpendicular to the thick, chromatin fiber of

the octopus sperm head.

B. Experimental Measurements

The scanning polarization-modulation nephelometer used for these measurements was similar to that developed by one of the authors,[16] and is described in chapter 4. At each angle, S_{ij} was divided by the total intensity matrix element, S_{11}. Henceforth, $\mathbf{S}_{ij}$ (bold type face) will refer to the normalized matrix element. Baselines for $\mathbf{S}_{14}$ were measured using 0.49 μm latex spheres. The deviation of $\mathbf{S}_{14}$ from zero for these spheres provides a measure of the uncertainty in $\mathbf{S}_{14}$, which indicates that measurements of $\mathbf{S}_{14}$ are accurate to within 0.3%.

Samples of octopus sperm, *Eledone cirhossa* were obtained in dried form from Prof. J.A. Subirana, Dept. of Chemical Engineering, Polytechnique University at Catalonia, Barcelona Spain. A small portion of the sample was placed in normal saline buffer and adjusted to pH 7.0. An image of the helical sperm head obtained from scanning electron microscopy is shown in Figure 5.1. The sample was sonicated for about twenty hours. Sonication caused the sperm tails to separate from the helical heads and break into small pieces. Figure 5.2 shows a transmission electron micrograph of the sperm head. This figure suggests that the sperm head is composed of a thick electron dense helical fiber surrounded by a thin membrane. We hypothesize that the sperm head fiber is a DNA-protein complex that dominates light scattering from the sperm head. The dimensions of the sperm head are: pitch = 675-700 nm, radius = 250-300 nm, and length approximately 43 μm. [64] The radius quoted above is an outer radius. The electron micrograph in shown in Figure 5.2 indicates that the radius of the helical sperm head fiber is about 200 nm and is about 100 nm thick.

Measurements of several matrix elements are shown in Figure 5.3. S_{11} is plotted on a log scale. The scattering angle is multiplied by sin(θ) in order to normalize by the scattering volume. The measurement shown for S_{14}, taken at 457 nm., is very similar to that previously measured on a different instrument for a different preparation of the sample at 488 nm by Wells *et al.*[64] Both measurements are characterized by a large positive peak at around 30°. The previous measurements of S_{14} show a stronger peak at 90° than the measurement in Figure 5.3 as well as a negative peak at 135°. These slight discrepancies between these the measurements are probably due to a larger contamination in our sample by Rayleigh scattering from sperm tail fragments. Wells *et al.* removed sperm tail fragments from their sample by centrifugation.[64] We were not successful in doing this. Since the sperm heads are strong forward scatterers, small tail fragments in our sample would have a larger relative contribution to the total light scattering away from the forward direction. The S_{14} of the non-helical sperm heads is zero, but they diminish the measured S_{14} by contributing to S_{11}. The normalized S_{14} would become $\frac{S_{14}}{S_{11_h}+S_{11_t}}$, where S_{11_h} and S_{11_t} refer to the S_{11} due to the heads and tail fragment respectively. Thus the sperm tails would tend to reduce the measured, normalized S_{14} particularly away from the forward direction. Reflections in our scattering cell discussed previously [64] may also explain the difference in our results in the back-scattering region. In general there is good agreement between our results and those of Wells *et al.*

C. Born Approximation in the Orientation Average

Before using the coupled-dipole approximation to model the light scattering

data obtained from octopus sperm heads, we calculate the Mueller matrix elements in the orientation average for a helix using the first Born approximation. It is found that S_{34} is zero. Since this does not agree with experiment, we will turn to the coupled dipole approximation to model polarized light scattering from octopus sperm. For thinner or smaller particles, the Born approximation may apply.

Many authors have addressed the problem of predicting the scattering matrix elements for helices averaged over orientation.[31,34,42] In particular, Bustamante's group used the first Born approximation to calculate the orientation average of S14 and S_{11} for wire helices with point polarizable groups.[31] In what follows, this calculation was extended to include all 16 Mueller matrix elements. Our derivation follows that of Bustamante *et al.* closely. In addition, the case of a continuous helix, rather than one defined by point polarizable groups, is discussed.

The rotational average of any function is given by

$$\langle F(\alpha_e,\beta_e,\gamma_e)\rangle = \left(\frac{1}{8\pi^2}\right) \int_0^{2\pi}\int_0^{\pi}\int_0^{2\pi} F(\alpha_e,\beta_e,\gamma_e)\,\sin(\beta_e)\,d\alpha_e\,d\beta_e\,d\gamma_e \qquad (5.1)$$

where α_e, β_e, and γ_e are the Euler angles defining the following counter-clockwise rotations: a rotation around the z-axis, around the new y-axis, and around the new z-axis. Since the Mueller matrix elements are expressed in terms of products of scattering amplitude matrix elements, we compute the averages for these quantities. Each product will be a combination of factors involving scalar products of the polarizability vectors and the distance vector between point polarizable groups, $\vec{r}_{ij}$. In addition, the term $e^{i(\vec{k}-\vec{k}^0).\vec{r}_{ij}}$ will be present. This term is difficult to integrate over since it involves terms in the laboratory and the reference particle frames. To simplify this problem, the laboratory and particle frames are defined carefully. In the

laboratory frame, defined by unit vectors, $\hat{a}$, $\hat{b}$, and $\hat{c}$, $\vec{k}$ and $\vec{k}^0$ are defined in the b-c plane with their difference vector along c. The particle frame, defined by $\hat{i}$, $\hat{j}$, and $\hat{k}$, has the distance unit vector , $\hat{u}_{ij} = \frac{\vec{r}_{ij}}{r_{ij}}$ along the k direction. With these definitions, the exponent in the integral only involves the polar angle, β_e . To further simplify the calculation, the polarizability vector of the ith particle is defined in the i-k plane while that of the jth particle has three components. After averaging, this introduces no loss of generality. Thus,

$$\vec{k} = \cos(\zeta)\,\hat{b} + \sin(\zeta)\,\hat{c} \text{ and } \vec{k}^0 = \cos(\zeta)\,\hat{b} - \sin(\zeta)\,\hat{c}, \tag{5.2}$$

where ζ is twice the scattering angle. With these definitions, the unit vectors parallel and perpendicular to the scattering plane, defined in in Equations 2.45 and 2.47, are

$$\hat{e}_l^s = -\sin(\zeta)\,\hat{b} + \cos(\zeta)\,\hat{c},\ \hat{e}_l^0 = \sin(\zeta)\,\hat{b} + \cos(\zeta)\,\hat{c}, \text{ and } \hat{e}_r^0 = \hat{e}_r^s = \hat{a}. \tag{5.3}$$

Evaluating Equation 2.46, the scattering amplitude matrix elements are written:

$$\begin{aligned} S_2 &= \Gamma \sum_i e^{i(\vec{k}-\vec{k}^0)\cdot\vec{r}_i}\, w_i \overleftrightarrow{w}_i\, \hat{e}_l^s \cdot \hat{e}_l \text{sup} 0 \\ S_3 &= \Gamma \sum_i e^{i(\vec{k}-\vec{k}^0)\cdot\vec{r}_i}\, w_i \overleftrightarrow{w}_i\, \hat{e}_l^s \cdot \hat{a} \\ S_4 &= \Gamma \sum_i e^{i(\vec{k}-\vec{k}^0)\cdot\vec{r}_i}\, w_i \overleftrightarrow{w}_i\, \hat{e}_l^0 \cdot \hat{a} \\ S_1 &= \Gamma \sum_i e^{i(\vec{k}-\vec{k}^0)\cdot\vec{r}_i}\, w_i \overleftrightarrow{w}_i\, \hat{a} \cdot \hat{a} \end{aligned} \tag{5.4}$$

where $w_i \overleftrightarrow{w}_i$ is the outer product of the polarizability vector of the ith particle and Γ is a proportionality constant that divides out upon normalization. The expressions for the jth particle are exactly the same with j replacing i. The quantities to be averaged are products of the scattering amplitude matrix elements such as $S_{2_i} S_{3_j}{}^*$. The polarization vectors, $\vec{w}_i$ and $\vec{w}_j$, are written:

$$\vec{w}_i = s_i\,\hat{i} + l_i\,\hat{k}, \text{ and } \vec{w}_j = s_j\,m\,\hat{i} + s_j\,n\,\hat{j} + l_j\,\hat{k}. \tag{5.5}$$

The parameters l_i, l_j, s_i, s_j , m, and n can be written in terms of scalar and vector products of $\vec{e}_i$, $\vec{e}_j$, and $\hat{R}_{ij}$.

$$\begin{gathered} l_i = \hat{w}_i \cdot \hat{u}_{ij}, \quad l_j = \hat{w}_j \cdot \hat{u}_{ij}, \\ s_i = |\hat{w}_i \times \hat{u}_{ij}|, \quad s_j = |\hat{w}_i \times \hat{u}_{ij}| \\ n = \frac{(\hat{w}_i \times \hat{w}_j) \cdot \hat{u}_{ij}}{s_i s_j} \quad m = \frac{(\hat{w}_i \times \hat{u}_{ij}) \cdot (\hat{w}_j \times \hat{u}_{ij})}{s_i s_j} \end{gathered} \tag{5.6}$$

MATHEMATICA was used to generate the entire Mueller matrix for the first Born approximation for the orientation average. The Mueller matrix elements are sums of products of the scattering amplitude matrix elements. These relationships between these quantities are given elsewhere.[40] For example

$$S_{34} = \mathrm{Im}(S_2 S_1^* + S_4 S_3^*), \tag{5.7}$$

where Im denotes the imaginary part. The products of scattering amplitude matrix elements, necessary to calculate all the Mueller matrix elements, are given in Appendix I for a helix in the orientation average. The Mueller matrix elements are simple combinations of these products. The results for un-normalized S14 and S24 are presented below:

$$\begin{aligned} S_{14} = \sum_i \sum_j & (8\, j_2/q\, l_i\, l_j\, n\, \pi^2\, s_i\, s_j + 2\, j_1\, m\, n\, \pi^2\, s_i^2\, s_j^2 \\ & - 2\, j_2/q\, m\, n\, \pi^2\, s_i^2\, s_j^2\,)\,(\,\sin(\zeta) + \sin(\zeta)^3\,) \\ S_{24} = \sum_i \sum_j & (8\, j_2/q\, l_i\, l_j\, n\, \pi^2\, s_i\, s_j + 2\, j_1\, m\, n\, \pi^2\, s_i^2\, s_j^2 \\ & - 2\, j_2/q\, m\, n\, \pi^2\, s_i^2\, s_j^2\,)\,(\,\sin(\zeta) - \sin(\zeta)^3\,) \end{aligned} \tag{5.8}$$

where j_1 and j_2 are first and second order Bessel functions with argument $q = 4\,\pi / \lambda \sin(\zeta)\, r_{ij}$. The result for S14 is identical to that published earlier.[31] Examination of the scattering amplitude products given in Appendix I reveals that the following are all real : $S_1S_1^*$, $S_2S_2^*$, $S_3S_3^*$, $S_4S_4^*$, $S_1S_2^*$, $S_3S_4^*$, $S_2S_1^*$, and $S_4S_3^*$, the

following are all imaginary : $S_2S_3^*$, $S_1S_4^*$, $S_2S_4^*$, $S_1S_3^*$,$S_3S_1^*$. Thus, the following elements were found to be identically zero : S34, S13, S23, S43, S31, and S32. This is consistent with calculations made previously by McClain et al.[33] These expressions are general results for a given structure defined by point polarizable particles with a distance unit vector, $\hat{u}_{ij}$, and polarizability vectors $\hat{w}_i$ and $\hat{w}_j$. A helix can be defined like that in Figure 3.1 with point polarizable groups along the wire at points defined by θ_i and θ_j. The double sums can be converted to integrals over $d\theta_i$ and $d\theta_j$, which can be evaluated numerically. Since the Mueller matrix elements under this formalism are only functions of $\theta_i - \theta_j$, the double integral can be converted to a single one by making the following change of variable $\theta_i - \theta_j \rightarrow u$ and $\theta_i + \theta_j \rightarrow v$. The required numerical integrals over one variable can be carried out on any small computer. Modelling a continuous helix is advantageous because one need not worry about the number of point polarizable groups necessary to describe the helix and helices with large dimensions can be accommodated.

D. The Coupled-Dipole Approximation

We have modeled the angular dependence of several scattering matrix elements from octopus sperm using the coupled-dipole approximation. Equation 2.33 represents the scattered electric field using the coupled-dipole approximation. In the coupled-dipole approximation, the electric field at each subunit is equal to the incident field plus the electric field due to radiation from all the other subunits. If a particle is modelled by N dipoles, 3N linear equations must be solved simultaneously in order to determine the net electric field at each dipole location. The solution of the simultaneous equations to find the electric field at each dipole is a limiting problem with the coupled-dipole method. Since this requires the inversion of a large

matrix, a large computer must be employed to carry out calculations involving particles composed of many subunits. Although this limitation does not apply to calculations using the first Born approximation, the coupled-dipole approximation is a more rigorous theory that can be applied to thicker particles and allows for a realistic study of the polarizability.

The present work uses a formulation of the coupled-dipole approximation in the orientation average based on one described previously.[34,36] The sperm head was modelled by subunits placed along a helix defined by:

$$\vec{r}' = a\cos(\theta_h)\,\hat{x} + a\sin(\theta_h)\,\hat{y} + \frac{P\theta_h}{2\pi}\,\hat{z}, \tag{5.9}$$

where a is the radius, P is the pitch and θ_h runs from 0 to $2\pi l$ with l indicating the number of helix turns. The polarizability tensor is defined in terms of a local coordinate system to the helix:

$$\overleftrightarrow{\alpha} = \alpha_{tt}\,\hat{t}\hat{t} + \alpha_{nn}\,\hat{n}\hat{n} + \alpha_{pp}\,\hat{p}\hat{p}, \tag{5.10}$$

where $\hat{n}$, $\hat{p}$, and $\hat{t}$ are locally defined mutually orthogonal unit vectors. These unit vectors are usually defined in terms of the tangent, normal and binormal of the helix.[28,43] In this work, since we want to investigate the direction of the polarizability tensor, these unit vectors were defined so that they can be rotated with respect to the tangent, normal and binormal directions. The unit vectors $\hat{n}$, $\hat{p}$, and $\hat{t}$ are defined as

$$\begin{aligned}
\hat{n} &= \cos(\zeta_1)\sin(\zeta_2)\hat{n}' + \sin(\zeta_1)\sin(\zeta_2)\hat{p}' + \cos(\zeta_2)\hat{t}' \\
\hat{t} &= \cos(\zeta_1)\cos(\zeta_2)\hat{n}' + \sin(\zeta_1)\cos(\zeta_2)\hat{p}' - \sin(\zeta_2)\hat{t}' \\
\hat{p} &= -\sin(\zeta_1)\hat{n}' + \cos(\zeta_2)\hat{p}'
\end{aligned} \tag{5.11}$$

where the angles ζ_1 and ζ_2 define the rotation of the local coordinate system defined by,

$$\hat{t}' = -(\frac{a}{M})\sin(\theta_h)\,\hat{x} + (\frac{a}{M})\cos(\theta_h)\,\hat{y} + (\frac{P}{2\pi M})\,\hat{z}$$
$$\hat{p}' = (\frac{P}{2\pi M})\sin(\theta_h)\,\hat{x} - (\frac{P}{2\pi M})\cos(\theta_h)\,\hat{y} + (\frac{a}{M})\,\hat{z} \qquad (5.12)$$
$$\hat{n}' = \cos(\theta_h)\,\hat{x} + \sin(\theta_h)\,\hat{y}$$

with,

$$M = (a^2 + \frac{P^2}{4\pi^2})^{\frac{1}{2}}.$$

The model for the octopus sperm head was a single turn of a helical fiber composed of about 40 spherical subunits about 35 nm thick. Because the fortran code used in this work requires an enormous amount of memory, the number of subunits incorporated into our model was severely limited. Earlier work indicated that, for accurate results, the thickness of a subunit should not exceed one tenth the wavelength of light.[43] The use of only a single turn of a helix is adequate to model the normalized matrix elements because our results indicate that these do not change much as a function of the number of turns. Only S_{11} is strongly dependent on the number of turns of a helix. This is true as long as each subunit on each successive turn is placed in phase with those below it; for example, if a subunit is placed at $\theta_h = \frac{\pi}{8}$, then one must also be placed at $\theta_h = \frac{9\pi}{8}$. If the subunits on a multiple turn helix are not placed in this manner, all the normalized Mueller matrix elements are dependent on the number of turns of the helix (Although this dependence disappears for a large number of turns or subunits). The independence of S_{14} to the number of turns is demonstrated in Figure 5.4 for a single helix oriented parallel to the incoming light. S_{14} is the same for one and two turns of this helix. S_{11} is shown normalized by its magnitude at 0°. Figure 5.4 shows that S_{11} depends on the number of turns. The changes in S_{11} demonstrate that as the number of turns

increases the helix becomes more forward scattering. We have also observed the independence of all the Mueller matrix elements normalized by S_{11} for helices modelled as a continuous dielectric using the first Born approximation. The use of a single turn to model the octopus sperm is justified because the normalized matrix elements are not greatly affected by the number of turns of the helix..

E. Results

The S_{14} calculated using spherical subunits with isotropic polarizability did not result in S_{14} with a magnitude equal to the measured values. The largest calculated S_{14} found assuming an isotropic polarizabilty was less than 1.5% with $\alpha_s = 5{,}233\ nm^3$. In general the calculated S_{14} should be larger than the measured one since other scatterers in the sample will reduce the measured S_{14} by contributing to S_{11}. We therefore found it necessary to assume that modelled helical fiber was composed of material with an inherently anisotropic polarizability. This inherent anisotropy could correspond to ordered packing of the DNA in the sperm head.

S_{34} was most sensitive to the absolute strength of the polarizability. The absolute magnitude of the polarizabilty was originally set at a value computed by the theory outlined in chapter 2 (Equations 2.37-2.43) with the dielectric constant of the material set at 2.0 and that of the medium at 1.8. The magnitude of the polarizability was then refined by comparisons of the magnitude of calculated S_{34} with the measured magnitudes. When calculations were attempted with a polarizability that was too large, poor agreement of S_{12} and S_{14} with measured values resulted. When the polarizability is too large, the coupled dipole approximation breaks down because the interaction between subunits becomes too large.

Mueller matrix elements were calculated for a wavelength in the medium (index of refraction = 1.3) of 352 nm. The following parameters in the model were varied in an attempt to replicate the measured Mueller matrix elements (S_{14}, S_{12}, S_{34}): pitch, radius, degree of anisotropy of the polarizability and the direction of the principle axes of the polarizability with respect to the helix. The best fit (Figure 5.5a) was obtained using a pitch = 650 nm, radius = 190 nm, and polarizability strengths α_{tt} = 6,433 nm^3, $\alpha_{pp} = \alpha_{nn}$ = 2,617 nm^3, The direction of the principle axis of polarizability for α_{tt} was 9° from the tangent to the helical fiber. The anisotropy ratio $\frac{\alpha_{tt} - nn}{\alpha_{tt} + \alpha_{nn}}$ was 42%.

The largest strength of the polarizability is close to tangent to the helix. Figures 5.5b and 5.5c show the calculated matrix elements when that strength is placed along the normal or binormal. Comparison with the experimental results shown in Figure 5.3 points out the superiority of orienting the large polarizability close to the tangent of the helical fiber.

Lack of agreement between the measured and calculated results may be partially due to the presence of Rayleigh scatterers in the sample, such as sperm tail fragments. To investigate this possibility, the calculations were repeated with a correction for the presence of Rayleigh scatterers. Rayleigh scatterers are characterized by the following Mueller matrix elements:

$$S_{14} = S_{34} = 0,\ S_{11} = \gamma(1 + \cos^2(\theta)),\ S_{12} = \gamma(\cos^2(\theta) - 1), \qquad (5.13)$$

where γ corresponds to the amount of Rayleigh scatterers present. The corrected values of the Mueller matrix elements are calculated by adding the calculated matrix element for the helical sperm head fiber to that of the Rayleigh scatterer:

$$S_{ij} \rightarrow S_{ij_c} + S_{ij_r} \tag{5.14}$$

where S_{ij_c} and S_{ij_r} are the matrix elements from the original calculation for the helical fiber and the Rayleigh scatterers. Thus for S_{12},

$$\frac{S_{12}}{S_{11_h}} \rightarrow \frac{S_{12_c} + S_{12_r}}{S_{11_c} + S_{11_r}}. \tag{5.15}$$

The amount of scattering due to Rayleigh scatterers was determined by comparison with experiment. The results of this correction for an amount of Rayleigh scatterers such that they scatter as much as the helical sperm fibers at 90° is shown in Figure 5.6a. Figure 5.6b shows S_{11_c} calculated for one turn of the helix.

E. Discussion

We have modelled the polarized light scattering from octopus sperm using the coupled-dipole approximation. Modelling several Mueller matrix elements simultaneously aids in limiting the combination of parameters that describe the helix. By changing one parameter the calculated S_{14} may become more like the measured value, but S_{34} may become less like the measurement. This same argument applies to the Rayleigh correction used for Figure 5.6. When the relative contribution to the scattered light from the Rayleigh scatterers is too large, the calculated S_{12} becomes less like the measured data.

Comparison of S_{11} in Figure 5.6b with the measurements shown in Figure 5.3 reveals that the measured S_{11} is much more forward scattering than is the calculated result. The thickness of the helical fiber used in the model, being significantly smaller than the apparent thickness of the real DNA-protein fiber, may have been responsible for the diminished forward scattering in the calculation. This can also be attributed to the calculation being made for only one turn of the helix. As

mentioned above, the Mueller matrix elements, normalized by the total intensity element S_{11}, do not depend heavily on the number of helix turns but S_{11} becomes more forward scattering when it is calculated for a helix having more turns. This should hold true as long as the length of the particle does not become too many times greater than the wavelength; at this point the shape of S_{11} should not change. The data shows that the sperm heads are very forward scattering. The S_{11} would have appeared even more forward scattering without the Rayleigh scatterers present. Therefore the Rayleigh scatterers in the sample may have diminished the normalized S_{14} and S_{34} even more than what is shown in Figure 5.6.

We have chosen to model S_{12}, S_{14}, and S_{34} because these elements are not difficult to measure and are representative of three classes of elements: the dipole elements (S_{12}), the helicity elements (S_{14}), and the retardation elements (S_{34}).[34,72] S_{12} is sensitive to general size parameters of a particle and is always observed for any type of particle(s). S_{14} is sensitive to the chiral nature of a particle; it is zero for an ensemble of randomly-oriented particles unless the particles are chiral. S_{34} is sensitive to size and refractive index; it is zero for small or thin particles.

Calculations using the polarizability theory outlined in Equations 2.37-2.43 applied to spherical subunits that make up the helix did not result in S_{14} as large as the measured values. It was necessary to incorporate spherical subunits with anisotropic dipoles into our model in order to best fit the data. The magnitude of S_{14} is very sensitive to the degree of anisotropy in the polarizability. The magnitude S_{34} is most sensitive to the magnitude of the polarizability. The number of nodes in S_{14} was very sensitive to the radius used in the model. This observation is consistent with an earlier one made using the first Born approximation.[28] The direction of the

polarizability affected the shape of all the Mueller matrix elements. The best results were obtained when the strongest polarizability was near tangent to the helix. Although the direction 9° from the tangent is based on somewhat subjective comparisons of calculations with measurements, Figure 5.5 shows that the the greatest polarizability lies closer to the tangent than to the normal or binormal directions. Since the polarizability of DNA is strongest in the plane of the base-pairs [73] (perpendicular to the 2 nm double helix) this result indicates that the DNA double helices in the sperm head lie perpendicular to the helical, thick sperm head fiber.

The most in-depth study of the ultra-structure of the sperm of *Eledone cirrhosa* was conducted by Maxwell.[74] This author concluded that the rigid helical structure of the sperm head is due its chromatin. That the shape of sperm head is due to the chromatin has also been suggested by other researchers for mammals, birds, insects, and annelids.[75] Maxwell found that DNA begins to form 10 nm fibers during spermiogenesis.[74] Maxwell also reported that the 10 nm fibers condensed further as spermiogenesis progressed but he did not propose an arrangement of the DNA within its final condensed form.[74]

The DNA being perpendicular to the sperm head fiber is consistent with several models of higher order DNA organization in sperm.[76-80] The 10 nm fiber referred to by Maxwell may be similar to the intermediate fiber proposed for the DNA-protamine complex formed in mammalian sperm.[76] In mammalian sperm, it is believed that a primary condensation of DNA occurs when 2 nm strands of DNA lie parallel to each other; one in the major groove of another.[76,77] The final level of organization of DNA in mammalian sperm may be similar to that in somatic cells.[77,78] The DNA intermediate fiber forms loops that are attached to a nuclear

matrix; the fibers ending up perpendicular to the axis of the larger fiber formed by the looped fibers and the nuclear matrix. The final fiber is about 840 nm thick in somatic cells, whereas the loops are about 60% smaller in sperm cells.[78] In sperm cells the DNA would be perpendicular to the chromatin fiber. An alternative model for stallion sperm DNA proposes that the DNA forms a structure similar to that of a cholesteric crystal.[79,80] In this model the DNA strands are parallel to each other within a cross section of a thick fiber. The average direction of the DNA rotates from one cross section to the next giving a characteristic pitch to the thick fiber. The DNA is perpendicular to the axis of the thick fiber in this cholesteric crystal model. Finally a model has recently been proposed by Hud, Balhorn and others (personal communication) for mammalian sperm that involves the formation of a thick fiber by a toroidal organization of DNA. The DNA winds around the perimeter of the thick fiber in a plane perpendicular to the fiber axis. Thus the DNA is perpendicular to the thick fiber in several models of DNA higher organization in sperm cells.

In summary, we have determined that the average direction of the 2 nm DNA strands are perpendicular to the thick, chromatin fiber in the octopus sperm head by comparing polarized light scattering measurements to theoretical calculations. Thus the technique of polarized light scattering can be used to obtain information in structural biology that cannot be otherwise obtained using microscopy techniques. With the extension of measurements to smaller wavelengths, where smaller structures can be studied, polarized light could become a more valuable biophysical tool.

VI. The Mueller scattering matrix of DNA Plectonemic Helices

A. Introduction

A plectonemic DNA helix is an interwound closed DNA molecule. The interwinding is known as supercoiling and is measured by writhe. A change in DNA linking number can be expressed as a change in writhe or twist (the rotation of a single DNA double helix around itself). Because supercoiling is involved in many biological processes,[81-83] a lot of attention has been focused on the study of supercoiled DNA in the form of a plectonemic helix. Many studies have been done in which energy considerations lead to models that predict the distribution of linking number in twist and writhe, the helix radius, as well as dynamic properties of the plectonemic helix.[84,85] The confirmation of these models have relied on electron and other forms of microscopy, dynamic light scattering and topological methods.[86,87] Polarized light scattering may provide a new non-intrusive method of studying DNA plectonemic helices providing information other techniques could not.

Polarized light scattering has become a useful tool in many scientific disciplines.[14,53,56,59] Polarized light scattering yields more structural information than total scattering intensity measurements.[28] In particular, it has been proposed that polarized light scattering be used to study macromolecular structure. This application has been somewhat successful in certain cases using visible light. However, more structural information is obtainable when the wavelength of light used is of the same order as the molecule being probed. With the possibility of using synchrotron radiation, it is likely that polarized light scattering can be extended to the X-UV, x-ray region and provide new insights into macromolecular structure.

The polarization effects of scattering are fully described by the elements of the 4x4 Mueller scattering matrix. The Mueller matrix has been calculated for a variety of structures using electromagnetic theory. For the study of macromolecules a lot of attention has been paid to the S_{14} matrix element (also known as circular intensity differential scattering) because of its sensitivity to the chiral parameters describing a particle. Diaspro and Nicollini calculated S_{14} from chromatin by assigning a triaxial polarizability to points along a helical contour.[60] Each point was assumed to correspond to an ellipsoidal nucleosome. The internal field caused by interactions between nucleosomes was accounted for. Patterson *et al.* calculated S_{14} for a model superhelix.[32] Their model consisted of a coiled coil. S_{14} was calculated by Patterson *et al.* using the first Born approximation where the induced internal field is ignored. Bustamante *et al.* examined the feasibility of measuring S_{14} from an ensemble of randomly oriented helices in the soft x-ray region using the first Born approximation.[88] In this work we calculate the Mueller matrix elements for a model of a DNA plectonemic helix using the coupled dipole approximation in the orientation average. The coupled dipole approximation accounts for internal interactions and retardation. We find that there would be more scattering from the DNA plectonemic helices used in our calculation in the soft x-ray region than in the UV and visible. Several matrix elements show sensitivity to the writhe of the DNA plectonemic helix.

B. The Polarizability

The polarizability tensor is defined by the directions of the principle axes and the strengths along these axes:

$$\tilde{\alpha} = \alpha_{nn}\,\hat{n}\hat{n} + \alpha_{pp}\,\hat{p}\hat{p} + \alpha_{tt}\,\hat{t}\hat{t}. \tag{6.1}$$

and

$$\alpha_j = \alpha_j' + i\,\alpha_j'', \; j = tt, nn, pp. \tag{6.2}$$

where t, n, p are directions of the principle axes. The real and imaginary parts of the polarizability can be obtained directly from absorption measurements using the following relations:[89,90]

$$\alpha_j' = A(\nu)\, 2\frac{C_1}{\pi} P\int_0^\infty \frac{\xi(x)dx}{\xi^2 - \nu^2}, \tag{6.3}$$

$$\alpha_j'' = A(\nu)\frac{-C_1\xi(\nu)}{\nu} \tag{6.4}$$

where ν is the frequency of light, P means the principle part, x is a variable of integration, ξ is the measured extinction, $C_1 = 6909c/8\pi^2N_0$, with c representing the speed of light and N_0 is Avogadro's number, and $A(\nu)$ is given by

$$A(\nu) = \frac{(n_s^2 + 2)^2}{9n_s^2}, \tag{6.5}$$

where n_s is the index of refraction of the solvent.

A base pair was represented by a single point polarizable group. The polarizability was calculated parallel and perpendicular to the base pair using the average absorption of each nucleotide. The absorption above 200 nm was completely in the base-pair plane. An isotropic absorption was assigned at 120nm to represent continuum transitions in the vacuum UV. These assignments are identical to those used previously.[91] In the x-ray region, The polarizability was assigned to each point using absorption data from benzene.[92]

C. The Model Plectonemic Helix

A three dimensional contour was defined by John E. Hearst to approximate a DNA plectonemic helix. A code written in MATHEMATICA is given in the Appendix II that generates this contour. The plectonemic helix is composed of two

interwound simple helices attached by a loop on each end. The simple helices are 180° out of phase.

Each base pair is represented by ellipsoidal polarizable groups. The principle axes of the polarizability of the ellipsoids are aligned along the tangent, normal, and binormal of the curve representing the plectonemic helix. Figure 6.1 shows the two and four turn helices used in this work. Each had 462 base-pairs. The dimensions of the two turn helix are 70 nm long, and helix radius 2.5 nm. Helix radius refers to the the radius of the helical region of the plectonemic model. The four turn helix is 62.6 nm long with a helix radius of 2.2 nm. Each dipole is about 3.42 ± 0.02 Å apart.

D. Results

In order to determine the structural information that may be obtainable from polarized light scattering measurements we have made calculations of Mueller matrix elements as a function of wavelength, writhe (or pitch), and the strength, directions and anisotropy of the polarizability. We do not report all the matrix elements here although our fortran code generates all of them. We have chosen to report the elements, S_{11}, S_{12}, S_{13}, S_{34}, and S_{14} because these represent the different categories of matrix elements. All the matrix elements are reported normalized by the total intensity element S_{11} except for S_{11} itself. We have made calculations of DNA in water. We have attempted to calculate the Mueller matrix elements at wavelengths where measurements can be made; where there is a sufficient transmission through water. We would like to have calculated the Mueller matrix elements at the carbon edge (about 4.3 nm) but this wavelength is too small compared to the width of the DNA base-pair so the coupled-dipole approximation breaks down for

our model. Therefore we have used the polarizability of the base pair at the carbon edge for calculations of the Mueller matrix elements at 20nm.

Figure 6.2 shows calculated Mueller matrix elements at different wavelengths, 633, 260, and 20 nm. The strengths of the polarizabilities in $\mathring{A}^3$ were as follows:

Wavelength	α_{tt}	α_{nn}	α_{pp}
633 nm	12.8	44	44
260 nm	15.2+0.88i	48.8+36.8i	48.8+36.8i
20 nm	0.72+0.4i	0.72+0.4i	0.72+0.4i

where $i = \sqrt{-1}$. S_{11} (plotted on a log scale in Figure 6.2) shows that our model plectonemic helices scatter most at 20 nm. The other matrix elements in Figure 6.2 are plotted as a relative intensity; they are normalized by S_{11}. The normalized S_{13} and S_{34} elements are zero when the wavelength is 633 nm on the scales used in Figure 6.2. S_{34} and S_{13} are largest at 20 nm.

As part of a preliminary investigation of the information obtainable from polarized light scattering we have compared Mueller matrix elements calculated for a two and four turn plectonemic helix (Figure 6.3). The structure of the total intensity element S_{11} is not very sensitive to a change in the writhe of the helices (Figure 6.3). S_{14} shows the most change with respect to the number and position of nodes, maxima, and minima for the calculation conducted at 20nm.

The excitations at the carbon edge involve the core carbon electrons. The polarizability is thus mainly isotropic. However, there are resonant excitations to the π and σ molecular orbitals.[93] These resonances result in an anisotropy in the polarizability parallel (π) or perpendicular (σ) to the DNA 2 nm strand. We have investi-

gated the sensitivity of the Mueller matrix of our model plectonemic helices to an anisotropy in the polarizability at 20 nm. Several matrix elements are shown in Figure 6.4 where the following polarizability strengths in $\mathring{A}^3$ were used:

Curve	α_{tt}	α_{nn}	α_{pp}
———	0.8+0.48i	0.64+0.32i	0.64+0.32i
.....	0.64+0.32i	0.8+0.48i	0.8+0.48i

S_{13} and S_{12} did not show much sensitivity to anisotropy in the polarizability. Of those shown in Figure 6.4, S_{11} is least sensitive to polarizability anisotropy.

E. Discussion

With recent advances in optical elements and a little ingenuity all of the Mueller matrix elements should be measurable in the soft x-ray region using synchrotron radiation. The elements S_{11}, S_{12}, and S_{13} could be measured using two detectors that move along two perpendicular scattering planes. Light emitted from a synchrotron is highly polarized in the plane of the accelerator ring. In order to measure S_{12} the two scattering planes should be parallel and perpendicular to the plane of the accelerator. Relative to the scattering plane that is perpendicular to the ring, the incident light is vertically polarized, and relative to the scattering plane that is parallel to the ring, the incident light is horizontally polarized. The intensities of the scattered light detected at the two perpendicular planes would be proportional to $S_{11} + S_{12}$ and $S_{11} - S_{12}$. Thus S_{12} is the difference of these measured intensities and S_{11} would be their sum. S_{13} can be measured in the same way with the two mutually perpendicular scattering planes being rotated 45°. A chopper that alternately blocks light to one of the two detectors would allow for a modulation of the

difference signal between the two detectors. New developments in the use of multilayer devices[94,95] could be used to measure the other elements in the second and third columns of the Mueller matrix. Thus, for example, if vertical polarizers were installed in front of the detectors that move in the planes parallel and perpendicular to the ring, the detected intensities would be $S_{11} + S_{12} + S_{21} + S_{22}$ and $S_{11} - S_{12} + S_{21} - S_{22}$. The difference between these measured intensities and the subtraction of the previously measured element gives S_{22}. Using diagonal polarizers and a combination of polarizers and 1/4 wave plates allows the measurement of the third and fourth row elements. In order to measure the elements in the fourth column, the incident light must be varied from right to left circularly polarized. One method of doing this would be to use right and left elliptically polarized light from above and below the ring plane. This would allow for measurement of the the fourth row Mueller matrix elements in the same way that they are measured conventionally.[16,40]

A more accurate determination of structure using polarized light scattering is obtained by comparing measurements with calculations for several Mueller matrix elements than a single one. For example different structures may produce the similar S_{34} but have entirely different S_{14}. The most commonly measured element, S_{11}, is least sensitive to structure. Thus, if light scattering is to be used to uncover new information regarding the structure of plectonemic helices, the investigation should involve several Mueller matrix elements.

The model used here to approximate DNA plectonemic helices differs in many respects to those obtainable experimentally. Whereas the DNA molecules in water would undergo various internal motions, our model is rigid. A sample prepared in

the lab would not be 100% homogeneous with respect to its linking number. A better model would account for internal motions and inhomogeneity of the sample. We have investigated scattering at the carbon edge by using polarizabilities calculated from benzene absorption data at 4.3 nm (at the C-edge) for calculations conducted at 20 nm. The calculations could be performed at 4.3 nm if more than one point polarizable group is used to represent a single base-pair. The addition of point polarizable groups, however, increases the time and memory requirements of the computer. We have found this calculation to be too intensive for the computer facilities available to us. Nevertheless, it is not too intense for existing supercomputers and will probably be more easily accomplished in the future.

Despite the model's limitations several useful observations can be made. The wavelength dependence of the total intensity element, S_{11}, shows that more scattering would be produced at the carbon edge than in the UV and visible. If the calculation were done at 4.3 nm instead of at 20 nm, more scattering would be expected since the intensity of scattering increases as the wavelength decreases. The larger S_{13} in the x-ray region makes it a good candidate for measurement, especially since it has an interesting angular dependence. A non-zero S_{13} results from either anisotropic polarizabilities or interaction along a chiral structure. The interaction between point polarizable groups must have been responsible for the S_{13} in the x-ray region when the polarizabilities were isotropic (Figure 6.2).

The Mueller matrix elements calculated for model plectonemic helices were sensitive to writhe in the visible, ultra-violet, and x-ray regions. The sensitivity of to writhe at 633 nm is consistent with experiments conducted by Nicollini *et al.* on supercoiled DNA.[61] The sensitivity to polarizability anisotropy in the carbon edge

could aid in structural determination by doing near edge polarized light scattering spectroscopy.

VII Polarized Light Scattering from Dinoflagellates

A. Introduction

In this chapter the measurement of a Mueller matrix element, S_{14}, is used to study the chromosomes of dinoflagellates. The S_{14} of a single immobilized dinoflagellate is compared to that from single inorganic particles. The S_{14} from several species of dinoflagellates are compared with damaged and preserved chromosomes. Finally, the S_{14} from live dinoflagellates is investigated as a function of cell cycle.

As a result of symmetry considerations, the S_{14} signal of most collections of randomly oriented particles is zero.[96] However, S_{14} signals can be non-zero for media containing optically-active material such as a collection of randomly-oriented helices.[31] The symmetry relationships that result in zero S_{14} for particles that are in suspension do not necessarily hold for single particles. Although particles with spherical symmetry have a zero S_{14}, other single particles such as an obliquely oriented cylinder can produce a non-zero S_{14} .[40] A helical structure is capable of producing highly circularly-polarized light from incident unpolarized light. For light incident along the longitudinal axis whose wavelength matches the pitch of the helix, one sense of circularly-polarized light is transmitted and the other is reflected.[30,96,97] Thus one expects a helix to be capable of producing very large S_{14} signals.

Large, angle-dependent S_{14} signals have been measured from single suspended cells of the dinoflagellate, *Prorocentrum micans*.[59] It was suggested that these signals are due to the helical nature of the dinoflagellate chromosomes. The exact

structure of the chromosomes of *P. micans* has yet to be agreed upon, but almost all proposed models involve some kind of helical structure.[99] One strongly confirmed model is Bouligand's liquid crystal model.[100-102] In the cholesteric crystal model, the DNA fibers are parallel to each other in each horizontal plane. The average direction of the fibers rotates as you move vertically along the chromosome. A cross section, as would be seen in a thin section in electron microscopy, reveals an arched pattern. The chromosome has a helical pitch of about 250 nm and produces a significant circular dichroism.[50] We examine whether the observed S_{14} produced in light scattering from *P. micans* is due to a helical structure or whether a similar signal can be induced by a single, non-helical, irregularly-shaped particle. In order to carry out this investigation scattering measurements were taken from single dinoflagellate cells and from single inorganic particles suspended in a transparent gel. The S_{14} is compared for different species of dinoflagellates at different wavelengths. Measurements are also taken from single dinoflagellates with damaged chromosomes. In addition, measurements are taken from live dinoflagellates in suspension at different times of the day.

B. Materials and Methods

The scanning polarization-modulation nephelometer used for these measurements was described in Chapter 4. The $S_{14}(\theta)$ was normalized by the total intensity element, $S_{11}(\theta)$. Henceforth, S_{14} will refer to the normalized matrix element. Any contribution that the gel makes to S_{11} decreases the observed S_{14}. In the calculation of the average S_{14}, this contribution was eliminated by multiplying the measured S_{14} signal by the ratio of the intensities of total scattered light to the scattering of the

particle alone. This yields a S_{14} signal normalized only by the total intensity of scattered light due to the particle.

Fixed samples of *C. cohnii* (CCOHNII(D)) and *G. polyedra* (GP60E) were generously provided by Bigelow Laboratory for single cell measurements. A strain of the dinoflagellate *P. micans* (LB1993) was grown in an enriched Erdschreiber's medium in Erlenmeyer flasks. The culture medium was made as follows: 1 liter sea water + 100ml distilled water + 50ml soil extract + 10ml Na_2HPO_4 (2g/l). Sea water from Bodega Bay, CA was filtered through Whatmans filter paper and autoclaved for 35 minutes. A soil extract was prepared by dissolving 50g of soil in 250cc of sea water and autoclaved for 120 minutes. After filtering using a Buechner funnel, the extract is autoclaved three times for 10 minutes and kept at 4° Celsius. A vitamin solution consisted of 0.06 mg biotin, 0.1 mg B_{12}, and 5 mg thiamin in 100ml distilled water. A metal solution was prepared by dissolving 0.750g Na_2 EDTA in 1 liter of distilled water and adding the following: 0.097g $FeCl_3$–$6H_20$, 0.041g $MnCl_2$–$4H_20$, 0.002g $CoCl_2$–$6H_20$, 0.005g $ZnCl_2$, 0.004g Na_2MO_4. An innoculant of 10ml of medium was added to 100ml of fresh medium: 2ml vitamin solution, 0.6ml metal solution, and 97.4ml culture medium. The dinoflagellates were kept at about 20° Celsius receiving light from cool fluorescent bulbs for 12 hours a day. Fresh air was circulated from a refrigerated room. The dinoflagellates were routinely observed in a light microscope and kept in logarithmic growth. These dinoflagellates are shaped like apple seeds and are approximately 50 μm in diameter. Their nucleii are about 15 μm in diameter and contain about 100-200 chromosomes.

The cells were fixed before being suspended in the gels. Cells were fixed in a

mixture of 1 part 6% glutaraldehyde solution to 1 part 0.4 molar phosphate buffer (ph 7.1) and to 1 part 7% NaCl solution. This primary fixation was continued for 2 hours at 0° Celsius. They were then washed three times and overnight in the cleaning solution: 1 part buffer to 1 part 4% NaCl solution. Post fixation was carried out with a 1% OsO_4 solution, 0.1M phosphate buffer, and 2.5% NaCl. After being rinsed for 3 x 20 minutes in the cleaning fluid the cells were dehydrated in 30%, 50%, 80% alcohol. Some of these cells were further dehydrated in 100% ethanol and suspended in epon resin for observation using a Zeiss 109 electron microscope. Thin sections were stained with lead citrate and uranyl acetate.

Two types of alumina particles were used: Linde A alumina particles normally used as a polishing powder, and Linde sapphire bouls ground to approximately -400 mesh. The particles were examined using an ISI-DS130 dual stage scanning electron microscope operated at 15 kV. The particles were coated with a 30 nm layer of platinum. A scanning electron micrograph of the particles is shown in Figure 7.1. The particle distributions, based on the electron micrographs, are presented in Figure 7.2. Particles were suspended in distilled water before suspension in the gels.

The immobilization technique has been described previously.[59] Cells and inorganic particles were stirred into silica alcogels just prior to gelation. An alcogel that forms in about two hours is composed of 16ml of TEOS (tetraethylorthosilicate) and 27.5ml ethanol prepared in one flask and 27.5 ml ethanol, 28ml distilled water, 0.5ml ammonium fluoride and 0.09 ml ammonium hydroxide prepared in a separate flask and then mixed. The gels were bathed in solutions of ethanol and water with increasing glycerol concentrations. The first bath had 27% water, 56% ethanol, and 17% glycerol. Four intermediate baths were used. The gel remained in the bath

until it equilibrated as evidenced by the clarity of the solution upon stirring. The final bath was 92% glycerol, 4% water, and 4% ethanol. The index of refraction of this liquid bath (1.48) was adjusted to nearly match that of the silica in the gel, thereby minimizing the gel scattering so that the scattering is dominated by immobilized particles.

The substituted gels were placed in a large scattering cell containing the final bath solution. Various parts of the gel were studied with the aid of a moveable x-y-z stage. To further reduce the scattering from the gel, the beam diameter and aperture size were minimized. A particle was centered in the laser beam using a Zeiss stereo microscope and the total intensity maximized at 90°. Angular measurements were taken from about 5° to 165° and the data was recorded on a Hewlet-Packard data acquisition system and interface. The background scattering from the gel was measured by moving the stage so that the particle being studied was just out of the beam. Only a small fraction of the inorganic particles scattered sufficient light to dominate the scattering from the gel and the particle. Therefore scattering could be measured from the larger particles only.

Some measurements were taken on live dinoflagellates in suspension. Live cultures of *Prorocentrum micans* were poured into a cylindrical scattering cell. The detector was set at 90° and $\mathbf{S}_{14}$ was measured as a function of time. Lighting conditions were matched to those used in the culture facility. The laser was incident on the sample only for the minimal time required to conduct a measurement.

C. Results

P. micans vs inorganic particles

S_{11} and S_{14} were measured from ten single, different alumina particles and three *P. micans* cells. The results for one dinoflagellate and several alumina particles are shown in Figure 7.3. The S_{14} signal of each particle is displayed immediately to the right of the corresponding S_{11} plot. The lower, smooth curve shown in the S_{11} graphs represents the background scattering from the gel. All measurements were highly reproducible.

The S_{14} signals from the dinoflagellates were significantly larger than those from the scattering from the inorganic particles. The S_{14} peaks in the scattering from the dinoflagellates attain 50% whereas those from a single inorganic particle do not exceed 30%. In the past S_{14} peaks as high as 60% were measured for single dinoflagellates.[59]

Only the largest inorganic particles produced S_{14} signals over 20%. The inorganic particles had a wide size range, from about 1 to 50 μm. Although it was difficult to determine the size of the scattering particles during the measurement, larger particles have larger S_{11} signals. Therefore the S_{11} is an indicator of the relative size of the particles. The plots of S_{11} and S_{14} in Figure 7.3 suggest that smaller particles produce smaller S_{14} signals.

The above argument is made more quantitative with aid of Figure 7.4. Plotted on the vertical axis of this graph is the average of the three highest S_{14} peaks for each particle. Each point represents one particle. The intensities of these peaks were corrected for the contribution of the gel to the S_{11} signal. The average S_{11} signal (also corrected for the scattering of the gel) corresponding to the three peaks used in calculating the S_{14} average is plotted on the horizontal axis for each particle. For particles that are large compared to the wavelength of incident light, as these

inorganic particles are, the intensity of scattered light is approximately proportional to the cross-sectional area of the particle. If the radius of the largest particle shown in Figure 7.4 is 50 μm (the largest size observed in the electron micrograph), then the radii corresponding to the other values of S_{11} for the inorganic particles in Figure 4 are approximately 15,18,19,21, and 45 μm.

Figure 7.4 shows that smaller alumina particles produce smaller $\mathbf{S}_{14}$ signals. For smaller inorganic particles, the $\mathbf{S}_{14}$ signal appears to be proportional to the size of the particle. $\mathbf{S}_{14}$ for larger particles approaches 30% asymptotically. Particles with more spherical shapes would be expected to give smaller $\mathbf{S}_{14}$ signals. This is probably the case for particles falling far below the curve. The $\mathbf{S}_{14}$ signal due to the five smallest particles measured is below 15% ; far below the $\mathbf{S}_{14}$ signal produced by the dinoflagellates.

Comparison of different species

$\mathbf{S}_{14}$ was measured and compared for single immobilized dinoflagellates of the species *P. micans, C. cohnii,* and *G. polyedra.* Measurements were conducted for several individual cells of each species at various orientations. As a result of poor fixation, one batch of *C. cohnii* and *G. Polyedra* had damaged chromosomes as evidenced by electron microscopy. Transmission micrographs of chromosomes from the samples used in this study are shown in Figure 7.5. Plots of the angular distribution of S_{11} and $\mathbf{S}_{14}$ are shown in Figure 7.6.

In order to compare the relative scattering from the different species, the integral of the absolute value of each $\mathbf{S}_{14}(\theta)$ measurement was calculated. The average of these integrals, in arbitrary units, for each species is shown in Table 7.1. Also

shown is the average number of S_{14} peaks for each plot that were greater than or equal to 50%. *P. micans* had the largest average absolute S_{14}. *C. cohnii* produced larger S_{14} than *G. polyedra* and those with well-preserved chromosomes produced larger signals than those with damaged chromosomes. Only the *P. micans* and *C. cohnii* with intact chromosomes were capable of producing signals larger than 50%.

Summary of Results of Scattering from Single Dinoflagellates		
Dinoflagellate	**Average SUM of S_{14}**	**Average # peaks>0.5**
P. micans	26.	0.25
C. cohnii (Intact)	20.	2.5
C. cohnii (Damaged)	17.	0.
G. polyedra (Intact)	15.	0.
G. polyedra ("Damaged")	16.	0.

Table 7.1. Comparison of S_{14} from different species of dinoflagellates. The sum of the absolute value of each angular scan of S_{14} (such as those shown in Figure 7.6) was calculated. The average of 3 to 5 sums was taken for each species and is represented in the second column. The third column shows the average number of S_{14} peaks greater than or equal to 50% .

The wavelength dependence of S_{14} for a single *P. micans* was investigated. S_{14} was measured at wavelengths 457, 488 and 514nm. The absolute sum was calculated for each scan at the three wavelengths. The results are shown in Table 7.2. The largest S_{14} was measured at 514 nm.

Wavelength Dependence of a single *P. micans*	
Wavelength	Sum of S_{14}
457	13.5
488	19.4
514	23.3

Table 7.2. The wavelength-dependence of $\mathbf{S}_{14}$ of a single *P. micans*. The absolute sum is compared for each wavelength.

Suspension Measurements of live *P. micans*

The time dependence of the $\mathbf{S}_{14}$ signal was measured at 90° as described above. The data from two such measurements taken at noon and midnight of a single day are shown in Figure 7.7a. The time dependence of the signal is probably due to scattered light from a single dinoflagellate traversing the laser beam. At such times the light scattering from this single dinoflagellate dominates the total light scattered into the detector. Light scattering from single immobilized dinoflagellates demonstrates that when the traversing dinoflagellate is of a particular orientation it could produce a large $\mathbf{S}_{14}$ signal at 90°. $\mathbf{S}_{14}$ at 90° from a suspension of 0.497 micron spheres is also shown (Figure 7.7a). Here, the signal is significantly smaller.

If the observed peaks are caused by scattering from single dinoflagellates traversing the beam, then varying the beam size should affect the size of the peaks. For a wider beam, the contribution of the surrounding media to the total light scattered into the detector would be larger and the measured $\mathbf{S}_{14}$ from the dinoflagellate would be smaller. In the case of a narrow beam, the light scattered into the detector would be dominated more by the scattering from the dinoflagellate and the measured

S_{14} would be larger. To test these predictions, measurements were taken with various beam sizes with the use of lenses. The results are shown in Figure 7.7b. The measurements reveal that the variation of the measured S_{14} with beam size is as predicted.

The measured S_{14} produced by live dinoflagellates at 90° is a function of the time of day. Measurements were taken every two hours for consecutive days. The results were quantified by calculating the variance (the square of the standard deviation) over the measured time and multiplying by a constant. The variance of the signal is plotted against time of day in Figure 7.8. The signal is diurnal with a peak near midnight. These measurements have been repeated several times with similar results.

D. Discussion

The data clearly show that the S_{14} signal generated by irregularly-shaped alumina particles is significantly smaller than the S_{14} signal produced by the dinoflagellates. At present, *P. micans* produces the largest S_{14} signals yet observed from a single particle. The inorganic particles have large, flat, smooth surfaces that together with their intrinsic birefringence might explain their S_{14} signals. The fact that the dinoflagellates do not have such surfaces yet can generate larger S_{14} signals reinforces the view that helical structures, which have been shown to produce large S_{14} signals in other systems, are responsible for the dinoflagellate S_{14} signals. This hypothesis is strengthened by observations pertaining to the dinoflagellate chromosome infrastructure. The pitch of the *P. micans* chromosome is about 250 nm. The wavelength of the light used to measure the dinoflagellate S_{14} signal was about 310

nm in the gel from the 457 nm band of the argon-ion laser. Since diffraction from periodic structures is generally strongest when the periodicity matches the wavelength, it is not surprising to observe such strong effects on circular polarization in the light scattering from a dinoflagellate.

Our data show that small-irregularly shaped particles (those with dimensions of approximately 15 μm) produce small S_{14} signals. The chromosomes of *P. micans* are about 1x5 μm. Thus it is possible that the chromosomes of *P. micans* produce S_{14} signals over several times those produced by structures of significantly larger size.

Measurements on different species of single immobilized dinoflagellates show that all three species studied, *P. micans, G. polyedra,* and *C. cohnii,* are all capable of producing large S_{14} signals. The largest signals may have been caused by helically-structured chromosomes. As mentioned in the introduction, helical structures are theoretically capable of large differential scattering of circularly-polarized light. The data shows that those dinoflagellates with known helically-structured chromosomes (*P. micans* and *C. cohnii*) yield larger S_{14} than the *G. polyedra.* The *P. micans* produce larger S_{14} than the *C. cohnii* and they also have about ten-fold as much DNA. Finally, *C. cohnii* with intact chromosomes produced larger S_{14} than those with damaged chromosomes.

The suspension measurements reveal that *P. micans* produce a high-frequency S_{14} signal. This signal is diurnal with a peak around midnight. The increase in the signal may be due to an altered chromosome structure resulting from DNA synthesis. Bhaud and Soyer showed that *P. micans* grown on a 12:12 light:dark cycle undergo DNA synthesis between 10PM and 2AM.[103] Preliminary flow cytometry

measurements show a correlation between the presence of S-phase cells and an increased variance in S_{14}. A structural change in the chromosomes that would result in a helical pitch that is closer to the wavelength of light is expected to cause a larger S_{14} .

VIII Concluding Remarks

We have examined various applications of polarized light scattering to the study of chromosome structure. The Mueller scattering matrix contains several elements which constitute the helical domain. These elements are well suited to the study of chromosome structure due to their sensitivity to chiral parameters that are related to the chromosomes. In Chapter 3 we examined and developed light scattering theory from helices that could be used to describe the Mueller matrix measured from chromosomes. In Chapter 5 we used polarized light scattering measurements and theory to obtain new insight into DNA packing in the sperm head of the octopus head *Eledone cirrhosa*. This study of the sperm head was sucessful because the chiral parameters of the sperm DNA fiber are of the same order of magnitude as those of the light that was used for the study. Thus the wavelength of light used to study a DNA structure must be chosen so that it is close to the dimensions of the chiral parameter being studied. This notion is reinforced by the results of the examination of polarized light scattering from DNA plectonemic helices in Chapter 6. The most fruitful polarized light scattering measurements on DNA plectonemic helices would be in the X-ray water window.

Dinoflagellate chromosomes have a superhelical pitch of the order of a few hundred nm. We have thus been able to study them using visible light. Our efforts lead to the detection of a S14 signal that seemed to vary with the cell cycle of the dinoflagellates. A problem associated with studying live cells is that not only the chromosomes scatter light. Thus the measured S_{14} that is normalized by the total scattered light intensity element S_{11} is diminished. Such a problem should not be as serious in the water window if macromolecules are studied in solution in the absence

of other particles.

Polarized light scattering has been hailed as a useful biophysical tool for over twenty years but its contribution to furthering knowledge in structural biology has been limited. Perhaps the availability of synchrotron radiation in the UV, soft X-ray region will allow for more extended applications of polarized light scattering in structural biology.

References

1. M. Kerker, *The Scattering of Light and other Electromagnetic Radiation*, Academic Press, New York, 1969.

2. K.A. Stacey, *Light Scattering in Physical Chemistry*, Academic Press, London, 1956.

3. G.G. Stokes, "On the Composition and Resolution of Streams of Polarized Light from Different Sources," *Trans. Cam. Phil. Soc.*, 9, 399, 1852. Reprinted in *Mathematical and Physical Papers*, G.G. Stokes, Volume 3, University Press, Cambridge, 233-258, 1901.

4. Lord Rayleigh, "On the Electromagnetic Theory of Light," *Phil. Mag.*, Series 5, 12(73), 81-101, 1881.

5. M.P. Solleilet, Sur les Parametres Caracterisant la Polarisation Partielle de la Lumiere Dans les Phenomenes de Fluorescence," *Ann. de Physique*, series 10 vol. 12, 24-97, 1929.

6. F. Perrin, "Polarization of Light Scattered by Isotropic Opalescent Media," *J. Chem. Phys.*, 10, 415-427, 1942.

7. R. Clark Jones, "A New Calculus for the Treatment of Optical Systems," *J. Opt. Soc. Am.*, 37(2), 107-112, 1947.

8. H. Mueller, "The Foundation of Optics," *Proc. Opt. Soc. Am.*, 38, 661, 1948.

9. B. Zimm, "Apparatus and Methods for Measurement and Interpretation of the Angular Variation of Light Scattering; Preliminary Results on Polystyrene Solutions," *J. Chem. Phys.*, 16, 1099-1116, 1948.

10. B.A. Brice, M. Halwer, and R. Speiser, "Photoelectric Light-Scattering Photometer for Determining High Molecular Weights," *J. Opt. Soc. Am.*, 40(11), 768-778, 1950.

11. P. Horn and H. Benoit, "Etude Experimentale de la Lumiere Diffusse par des Battonets Anisotropes," *J. Poly. Sci*, 10(1), 29-37, 1952.

12. R.S. Krishnan, "Uber die Dispersion der Depolarisation bei der Lichtstreung in Kolloiden Systemen," *Kolloid Zeits.*, 84(1), 2-8, 1938.

13. B.J. Berne and R. Pecora, *Dynamic Light Scattering*, Wiley, 1976. Scattering," *Nature* 21, 1257-1259, 1969.

14. B.S. Pritchard and W.G. Elliot, "Two Instruments for Atmospheric Optics Measurements," *J. Opt. Soc. Am.*, 50(3), 191-202, 1960.

15. Z. Sekera, "Polarization of Skylight," *Handbuch der Physik*, 48, 228-328, 1957.

16. A.J. Hunt, and D.R. Huffman, "A New Polarization-Modulated Light Scattering Instrument," *Rev. Sci. Instrum.*, 44, 1753-1762, 1973.

17. P.J. Wyatt, "Identification of Bacteria by Differential Light Scattering," *Nature* 21, 1257-1259, 1969.

18. D.W. Urry and T.H. Ji, "Distortions in Circular Dichroism Patterns of Particulate (or Membraneous) Systems," *Arch. Biochem. Biophys.*, 128, 802-807, 1968.

19. D.W. Urry and J. Krivacic, "Differential Scatter of Left and Right Circularly Polarized Light by Optically Active Particulate Systems," *P.N.A.S.*, 65(4), 845-852, 1970.

20. A.S. Schneider, M.T. Schneider, and K. Rosenheck, "Optical Activity of Biological Membranes: Scattering Effects and Protein Conformation," *P.N.A.S.*, 66(3), 793-798, 1970.

21. L.D. Barron and A.D. Buckingham, "Rayleigh and Raman Scattering from Optically Active Molecules," *Mol. Phys.*, 20(6), 1111-1119, 1971.

22. M.F. Maestre, D.M. Gray, R.B. Cook, "MCD Study on Synthetic Polynucleitides, Bacteriophage Structure and DNAs," *Biopolymers*, 10, 2537-2553.

23. B.P. Dorman, and M.F. Maestre, "Experimental Differential Light-Scattering Correction to the Circular Dichroism of Bacteriophage T2," *P.N.A.S.*, 70(1), 255-259, 1973.

24. E.M. Purcell and C.R. Pennypacker, " Scattering and Absorption of Light by Nonspherical Dielectric Grains," *Astrophys. J.*, 186, 705-714, 1973.

25. R.A. Harris, W.M. McClain and, C.F. Sloane, "On the Theory of Polarized Light Scattering from Dilute Polymer Solutions," *J. Chem. Phys.* 28(2), 381-398, 1974.

26. W.S. Bickel, J.F. Davidson, D.R. Huffman, and R. Kilkson, "Application of Polarization Effects in Light Scattering: A New Biophysical Tool," *P.N.A.S.*, 73(2), 486-490, 1976.

27. C. Bustamante, M.F. Maestre, and I. Tinoco Jr., "Circular Intensity Differential Scattering of Light by Helical Structures. I. Theory." J. Chem. Phys., 73(9), 4273-4281, 1980.

28. C. Bustamante, M.F. Maestre, and I. Tinoco Jr., "Circular Intensity Differential Scattering of Light by Helical Structures. II. Applications," *J. Chem. Phys.*, 73(12), 6046-6055, 1980.

29. C. Bustamante, I. Tinoco Jr, and M.F. Maestre, "Circular Intensity Differential Scattering of Light by Helical Structures. III. A Generalized Polarizability Tensor and Anomalous Scattering," *J. Chem. Phys..*, 74(9), 4839-4850, 1981.

30. C. Bustamante, M.F. Maestre, D. Keller, and I. Tinoco Jr., "Differential Scattering (CIDS) of circularly-polarized light by dense particles." *J. Chem. Phys.*, 80(10), 4817-4823, 1984.

31. C. Bustamante, I. Tinoco Jr, and M.F. Maestre, "Circular Intensity Differential Scattering of Light. IV. Randomly Oriented Species," *J. Chem. Phys..*, 76(7), 3440-3446, 1982.

32. C.W. Patterson, S.B. Singham, G.C. Salzman, and C. Bustamante, "Circular Intensity Differential Scattering of Light by Hierarchial Molecular Structures," *J. Chem. Phys..*, 84(3), 1916-1921, 1986.

33. W.M. McClain, J.A. Schauerte and R.A. Harris, "Model Calculations of Intramolecular Effects in Rayleigh Scattering from Solutions of Macromolecules," *J. Chem. Phys.* 80(2) 606-616, 1984.

34. W.M. McClain, and W.A Ghoul, "Elastic Light Scattering by Randomly Oriented Macromolecules: Computation of the Complete Set of Variables," *J. Chem. Phys.*, 84(12), 6609-6622, 1986.

35. S. Zeitz, A. Belmont, and C. Nicollini, "Differential Scattering of Circularly Polarized Light as a Unique Probe of Polynucleosome Superstructures," *Cell Biophys.*, 5, 163-187, 1983.

36. W.M. McClain, D. Tian, and W.A. Ghoul, "Comparison of Numerical and Analytical Orientation Average Methods in Polymer Light Scattering," *J. Chem. Phys..*, 87(8), 4986-4994, 1987.

37. Y. Shi and W.M. McClain, "Longwave Properties of the Orientation Averaged Mueller Scattering Matrix for Particles of Arbitrary Shape. I. Dependence on Wavelength and Scattering Angle," *J. Chem. Phys.* 93(8) 5605-5615, 1990.

38. Y. Shi and W.M. McClain, "Longwave Properties of the Orientation Averaged Mueller Scattering Matrix for Particles of Arbitrary Shape. II. Molecular Parameters and Perrin Symmetry," *J. Chem. Phys.* 93(8) 5605-5615, 1990.

39. Y. Shi and W.M. McClain, "Closed-Form Mueller Scattering Matrix for a Random Ensemble of Long, Thin Cylinders," *J. Chem. Phys.* 98(2) 1695-1711, 1993.

40. C.F. Bohren, and D.R. Huffman, *Absorption and Scattering of Light by Small Particles* (Wiley, New York, 1983).

41. S.B. Singham, and G.C. Salzman, "Evaluation of the Scattering Matrix of an arbitrary particle using Coupled-Dipole Approximation," *J. Chem. Phys.*, 84(5), 2658-2667, 1986.

42. M.K. Singham, S.B. Singham, and G.C. Salzman, "The Scattering Matrix for Randomly Oriented Particles," *J. Chem. Phys.* 85(7), 3807-3815, 1986.

43. S.B. Singham, and G.C. Salzman, " Polarizabilities for Light Scattering from Chiral Particles," *J. Chem. Phys.*, 85(2), 763-770, 1986.

44. S.B. Singham, and C.F. Bohren, " Light Scattering by an Arbitrary Particle: a Physical Reformulation of the Coupled Dipole Method," *Opt. Lett.*, 12(1), 10-12, 1987.

45. S.B. Singham, and C.F. Bohren, " Light Scattering by an Arbitrary Particle: the Scattering-Order Formulation of the Coupled-Dipole Method," *Opt. Soc. Am. A*, 5(11), 1867-1872, 1988.

46. S.B. Singham, and C.F. Bohren, "Hybrid Method in Light Scattering by an Arbitrary Particle," *App. Opt.*, 28(3), 517-522, 1989.

47. S.B. Singham, "Intrinsic Optical Activity in Light Scattering from an Arbitrary Particle," *Chem. Phys. Lett.*, 130(2), 139-144, 1986.

48. C. Nicollini and F. Kendall, "Differential Light-Scattering in Native Chromatin: Corrections and Inferences Combining Melting and Dye-Binding Studies. A Two Order Superhelical Model," *Physiol. Chem. Physics*, 9, 265-283, 1977.

49. M.F. Maestre, G.C. Salzman, R.A. Tobey, and C. Bustamante, "Circular Dichroism Studies on Single Chinese Hamster Cells," *Biochem.*, 24, 5152-5157, 1985.

50. F. Livolant and M.F. Maestre, "CD Microscopy of compact forms of DNA and Chromatin *in Vivo* and *in Vitro*: Cholesteric Liquid Crystalline Phases of DNA and Single Dinoflagellate Nuclei," *Biochemistry*, 27, 3056-3068, 1988.

51. S.V. Slonitski and V. Yu. Kuptsov, "Differential Scattering of Circularly Polarized Light by DNA Solutions with Spermine," *Molekulyarnaya Biologiya*, 24(2), 328-333.

52. K.J. Voss, and E.S. Fry, "Measurements of the Mueller Matrix for Phytoplankton," *Limnol. Oceanogr.*, 30, 1322-1326, 1985

53. M.S. Quinby-Hunt, A.J. Hunt, K. Lofftus, and D. Shapiro, "Polarized-Light Scattering Studies of Marine Chlorella," *Limnol. Oceanogr.*, 34 1587-1600, 1989.

54. M.F. Maestre, C. Bustamante, T.L. Hayes, J.A. Subirana, and I. Tinoco Jr., "Differential Scattering of Circularly-Polarized Light by the Helical Sperm Head from the Octopus *Eledone cirrhosa*," *Nature*, 298, 773-774, 1982.

55. G.C. Salzman in *Rapid Methods and Automation in Microbiology and Immunology*, K.O. Haberman, ed. Springer-Verlag, Berlin, 1985 pp. 184-193 and 194-197.

56. W.P. Van de Merwe, D.R. Huffman, and B.V. Bronk, " Reproducibility and Sensitivity of Polarized Light Scattering for Identifying Bacterial Suspensions," *Appl. Opt.*, 28, 5052-5057, 1990.

57. G. Garab, S. Wells, L. Finzi, and C. Bustamante, "Helically Organized Macroaggregates of Pigment-Protein Complexes in Chloroplasts: Evidence from Circularly Intensity Differential Scattering," *Biochemistry*, 27(16), 5839-5843, 1988.

58. C.T. Gross, H. Salomon, A.J. Hunt, R. I. Macey, F. Orme, and A.T. Quintanilha "Hemoglobin Polymerization in Sickle Cells studied by Circular Polarization Light Scattering," *Biochem. Biophys. Acta.*, 1079, 152-160, 1991.

59. K.L. Lofftus, A.J. Hunt, M.S. Quinby-Hunt, F. Livolant, and M.F. Maestre, "Immobilization of Unicellular Marine Organisms for Optical Characterization: A New Method and Results," *Appl. Opt.*, 31(15), 2924-2931, 1992.

60. A. Diaspro, M. Bertolotto, L. Vergani, and C. Nicollini, "Polarized Light Scattering of Nucleosomes and Polynucleosomes- *In Situ* and *In Vitro* Studies, *IEEE Trans. Biom. Eng.*, 38(7), 670-678, 1991.

61. C. Nicollini, A. Diaspro, M. Bertolotto, P. Facci, and L. Vergani, "changes in DNA Superhelical Density Monitored by Polarized Light Scattering," *Biochem. Biophys. Res. Com.*, 177(3), 1991.

62. A. Bricaud and A. Morel, "Light Attenuation and Scattering by Phytoplanktonic cells: A Theoretical Modelling," *Appl. Opt.*, 25, 571-580, 1986.

63. R.D. Haracz, L.D. Cohen, A. Cohen, and C. Aquista, "Light Scattering from Dielectric Targets Composed of a Continuous Assembly of Circular Disks," *Appl. Opt.*, 25(23), 4386-4395, 1986.

64. K.S. Wells, D.A. Beach, D. Keller, and C. Bustamante, "An Analysis of Circular Intensity Differential Scattering Measurements: Studies on the Sperm Cell of *Eledone cirrhosa*," *Biopolymers*, 25, 2043-2064, 1986.

65. J.D. Jackson, *Classical Electrodynamics*, Wiley, New York, 1975.

66. C. Bustamante, "Circular Intensity Differential Scattering of Chiral Molecules," Thesis, University of California, Berkeley, 1980.

67. D. Sherwood, *Crystals, X-Rays, and Proteins*, (Longman, New York 1976).

68. H.P. Jensen, J.A. Schellman, and T. Troxell, "Modulation Techniques in Polarization Spectroscopy," *Appl. Spect.*, 32(2), 192-200, 1978.

69. Y. Shindo and Y. Ohmi, "Problems of CD Spectrometers. 3. Critical Comments on Liquid Crystal Induced Circular Dichroism," *J. Am. Chem. Soc.*, 107, 91-97, 1985.

70. R.G. Johnston, S.B. Singham, and G.C. Salzman, "Polarized Light Scattering," *Comments Mol. Cell Biophys.*, 5(3), 171-192, 1988.

71. M.S. Quinby-Hunt, A.J. Hunt, and D. Shapiro, "Effects of the λ–Dependent Absorption on the Polarization of Light Scattered from Marine Chlorella," *Proc. SPIE*, 1302, 269-280, 1990.

72. D Tian, W.M. McClain "Nondipole Light Scattering by Partially Oriented Ensembles. I Numerical Calculations and Symmetries," *J. Chem. Phys.*, 90(9), 4783-4794, 1989.

73. N.T. Stellwagen, "Electrooptics of Polynucleitides and Nucleic acids," in *Molecular Electroptics*, edited by C. O'Kanski, Marcell Decker, 645-1978, 1978.

74. W.L. Maxwell, "Spermiogenesis of *Eledone cirrhosa* Lamark (Cephalopoda, Octopoda)," *Proc. R. Soc. Lond. B.*, 186, 181-190, 1974.

75. D.W. Fawcett, W.A. Anderson, and D.M. Phillips, "Morphogenic Factors Influencing the Shape of the Sperm Head," *Dev. Bio.*, 26, 220-251, 1971.

76. R. Balhorn, "A Model for the Structure of Chromatin in Mammalian Sperm," *J. Cell Bio.*, 93, 298-305, 1982.

77. R.H. Getzenberg, K.J. Pienta, W.S. Ward, D.S. Coffey, "Nuclear Structure and the Three-Dimensional Organization of DNA," *J. Cell. Bio.*, 47, 289-299, 1991.

78. W.S. Ward, A.W. Partin, and D.S. Coffey, "DNA Loops in Mammalian Spermotozoa," *Chromosoma*, 98, 153-159, 1989.

79. F. Livolant, "Cholesteric Organization of DNA in the Stallion Sperm Head," *Tiss. Cell*, 16, 535-555, 1983.

80. M.L. Sipski, and T. E. Wagner, "The Total Structure and Organization of Chromosomal Fibers in Eutherian Sperm Nucleii," *Biol. Repro*, 16, 428-440, 1977.

81. S.A. Wasserman and N.R. Cozarelli, "Biochemical Topology: Applications to DNA Recombination and Replication," Science, 232, 951-960, 1986.

82. R. Craigie and K. Mizuuchi, "Role of DNA Topology in Mu Transposition: Mechanism of Sensing the Relative Orientation of Two DNA Segments," Cell, 45, 793-800, 1986.

83. M. Gellert, "DNA Topoisomerases," *Ann. Rev. Biochem.*, 50, 879-910, 1981.

84. N.G. Hunt, J.E. Hearst, "Elastic Model of DNA Supercoiling in the Infinite-Length Limit," *J. Chem. Phys.*, 95, 9329-9336, 1991.

85. T. Schlick and W.K. Olsen, " Supercoiled DNA Energetics and Dynamics by Computer Simulation," *J. Mol. Biol.*, 223, 1089-1119, 1992.

86. T.C. Boles, J.H. White, and N.R. Cozarelli, "Structure of Plectonemically Supercoiled DNA," *J. Mol. Biol.*, 213, 931, 1990.

87. J. Langowski, W. Kremer, and U. Kapp, Dynamic Light Scattering for the Study of Solution Conformation and Dynamics of Supercoiled DNA," 211, 430-448, 1992.

88. C. Bustamante, M.F. Maestre, K.S. Wells, "Recent Advances in Polarization Spectroscopy: Perspectives of the extension to the Soft X-Ray Region," *Photochemistry and Photobiology*, 44(3), 331-341, 1986.

89. H. DeVoe, "Optical Properties of Molecular Aggregates. I. Classical Model of Electronic Absorption and Refraction," *J. Chem. Phys.*, 41, 393-400, 1964.

90. H. DeVoe, "Optical Properties of Molecular Aggregates. II. Classical Theory of Refraction, Absorption and Optical Activity of Solutions and Crystals," *J. Chem. Phys.*, 43, 3199-3208, 1965.

91. C.M. Cech, "Polynucleitide Circular Dichroism Calculations: Use of All Order Polarizability Theory," Dissertation, U.C. Berkeley, 1975.

92. J. Berkowitz, *Photoabsorption, Photoionization, and Photoelectron Spectroscopy*," Academic Press, New York, 1979.

93. H. Ade, X Zhang, S. Cameron, C. Costello, J. Kirz, and S. Williams, "Chemical Contrast in X-ray Microscopy and Spatially Resolved XANES Spectroscopy of Organic Specimans," *Science*, 258, 972-975, 1992.

94. J.B. Kortwright and J.H. Underwood, "Multilayer Optical Elements for Generation and Analysis of Circularly Polarized X-rays," *Nuc. Instrum. and Meth. in Phys. Res. A*, 291, 272-277, 1990.

95. J.B. Kortwright, H. Kimura, V. Nikitin, K. Mayama, M. Yamamoto, and M Yanagihara, "Soft X-ray (97eV) Phase Retardation using Transmission Multilayers," *Appl. Phys. Lett.*, 60, 2963-2965, 1992.

96. H.C. Van de Hulst, *Light Scattering by Small Particles*. Wiley, New York,1957.

97. A.S. Marathay, "Matrix-Operator Description of the Propagation of Polarized Light through Cholesteric Liquid Crystals." *J. Opt. Soc. Amer.*, 61(10), 1363-1372, 1971.

98. H.L. DE Vries, "Rotary Power and other Optical Properties of certain Liquid Crystals." *Acta. Crysta.*, 4, 219-226, 1951.

99. D.L. Spector, *Dinoflagellates*. Academic Press, 113-135, 1984.

100. A. Gautier, L.M. Salamin, E.T. Couture, A.W. Mcdowell, and J.Dubochet, "Electron Microscopy of the Chromosomes of Dinoflagellates in Situ: Confirmation of Bouligand's Liquid Crystal Hypothesis." J. Ultra. Mol. Struc. Res., 97, 10-30, 1986.

101. Y. Bouligand, M.O. Soyer, and S. Puiseaux-Dao, "La Structure fibrillaire et l'orientation des chromosomes chez les Dinoflagelles." Chromosoma, 24, 251-287, 1968.

102. F. Livolant and Y. Bouligand, "New Observations on the twisted Arrangement of Dinoflagellate Chromosomes." *Chromosoma*, 68, 21-44, 1978.

103. Y. Bhaud, and M.S. Soyer-Gobillard, "DNA Synthesis and Cell Cycle of a Primitive Dinoflagellate, *Prorocentrum micans,*" *Prostistologica*, 22, 23-30, 1986.

Appendix

The following are products of scattering amplitude matrix elements calculated for helices composed of point polarizable groups calculated using the first Born approximation. The Mueller matrix elements are sums of these products as given in reference 40.

$$
\begin{aligned}
s1s1^* &= 12\,fac8e\,\pi + 3\,fac3a\,\pi^2 - 6\,fac3c\,\pi^2 \\
&\quad + 9\,fac3e\,\pi^2 + fac4a\,\pi^2 - 2\,fac4c\,\pi^2 + 3\,fac4e\,\pi^2 \\
&\quad + 4\,fac5c\,\pi^2 - 12\,fac5e\,\pi^2 + 4\,fac6c\,\pi^2 - 12\,fac6e\,\pi^2 \\
&\quad + 4\,fac7c\,\pi^2 - 12\,fac7e\,\pi^2 + 16\,fac9c\,\pi^2 - 48\,fac9e\,\pi^2 \\
s2s2^* &= 2\,fac8a\cos(\beta)^4 - 8\,fac8c\cos(\beta)^4 + 16\,fac8e\cos(\beta)^4 \\
&\quad + 12\,fac3e\,\pi\cos(\beta)^4 + 4\,fac4e\,\pi\cos(\beta)^4 + 4\,fac5c\,\pi\cos(\beta)^4 \\
&\quad - 16\,fac5e\,\pi\cos(\beta)^4 - 4\,fac6c\,\pi\cos(\beta)^4 - 16\,fac6e\,\pi\cos(\beta)^4 \\
&\quad + 4\,fac7c\,\pi\cos(\beta)^4 - 16\,fac7e\,\pi\cos(\beta)^4 + 16\,fac9c\,\pi\cos(\beta)^4 - 64\,fac9e\,\pi\cos(\beta)^4 \\
&\quad - 8\,fac8c\,\pi\cos(\beta)^2\sin(\beta)^2 + 32\,fac8e\,\pi\cos(\beta)^2\sin(\beta)^2 - 8\,fac3c\,\pi^2\cos(\beta)^2\sin(\beta)^2 \\
&\quad + 24\,fac3e\,\pi^2\cos(\beta)^2\sin(\beta)^2 - 8\,fac4c\,\pi^2\cos(\beta)^2\sin(\beta)^2 + 8\,fac4e\,\pi^2\cos(\beta)^2\sin(\beta)^2 \\
&\quad - 4\,fac5a\,\pi^2\cos(\beta)^2\sin(\beta)^2 + 12\,fac5c\,\pi^2\cos(\beta)^2\sin(\beta)^2 - 32\,fac5e\,\pi^2\cos(\beta)^2\sin(\beta)^2 \\
&\quad - 4\,fac6a\,\pi^2\cos(\beta)^2\sin(\beta)^2 + 12\,fac6c\,\pi^2\cos(\beta)^2\sin(\beta)^2 - 32\,fac6e\,\pi^2\cos(\beta)^2\sin(\beta)^2 \\
&\quad - 4\,fac7a\,\pi^2\cos(\beta)^2\sin(\beta)^2 + 12\,fac7c\,\pi^2\cos(\beta)^2\sin(\beta)^2 - 32\,fac7e\,\pi^2\cos(\beta)^2\sin(\beta)^2 \\
&\quad + 32\,fac9c\,\pi^2\cos(\beta)^2\sin(\beta)^2 - 128\,fac9e\,\pi^2\cos(\beta)^2\sin(\beta)^2 + 12\,fac8e\,\pi\sin(\beta)^4 \\
&\quad - 6\,fac3c\,\pi^2\sin(\beta)^4 + 9\,fac3e\,\pi^2\sin(\beta)^4 + 1\,fac4a\,\pi^2\sin(\beta)^4 - 2\,fac4c\,\pi^2\sin(\beta)^4 \\
&\quad + 3\,fac4e\,\pi^2\sin(\beta)^4 + 4\,fac5c\,\pi^2\sin(\beta)^4 - 12\,fac5e\,\pi^2\sin(\beta)^4 + 4\,fac6c\,\pi^2\sin(\beta)^4 \\
&\quad - 12\,fac6e\,\pi^2\sin(\beta)^4 + 4\,fac7c\,\pi^2\sin(\beta)^4 - 12\,fac7e\,\pi^2\sin(\beta)^4 + 16\,fac9c\,\pi^2\sin(\beta)^4 \\
&\quad + 3\,fac3a\,\pi^2\sin(\beta)^4 - 48\,fac9e\,\pi^2\sin(\beta)^4 \\
s3s3^* &= 4\,fac8c\,\pi\cos(\beta)^2 - 16\,fac8e\,\pi\cos(\beta)^2 + 4\,fac3c\,\pi^2\cos(\beta)^2 - 12\,fac3e\,\pi^2\cos(\beta)^2 \\
&\quad - 4\,fac4e\,\pi^2\cos(\beta)^2 - 4\,fac5c\,\pi^2\cos(\beta)^2 + 16\,fac5e\,\pi^2\cos(\beta)^2 - 4\,fac6c\,\pi^2\cos(\beta)^2 \\
&\quad + 16\,fac6e\,\pi^2\cos(\beta)^2 - 4\,fac7c\,\pi^2\cos(\beta)^2 + 16\,fac7e\,\pi^2\cos(\beta)^2 + 4\,fac9a\,\pi^2\cos(\beta)^2 \\
&\quad - 20\,fac9c\,\pi^2\cos(\beta)^2 + 64\,fac9e\,\pi^2\cos(\beta)^2 + 4\,fac8e\,\pi\sin(\beta)^2 + 1\,fac3a\,\pi^2\sin(\beta)^2 \\
&\quad - 2\,fac3c\,\pi^2\sin(\beta)^2 + 3\,fac3e\,\pi^2\sin(\beta)^2 - 1\,fac4a\,\pi^2\sin(\beta)^2 + 2\,fac4c\,\pi^2\sin(\beta)^2 \\
&\quad + 1\,fac4e\,\pi^2\sin(\beta)^2 - 4\,fac5e\,\pi^2\sin(\beta)^2 - 4\,fac6e\,\pi^2\sin(\beta)^2 - 4\,fac7e\,\pi^2\sin(\beta)^2 \\
&\quad + 8\,fac9c\,\pi^2\sin(\beta)^2 - 16\,fac9e\,\pi^2\sin(\beta)^2 \\
s4s4^* &= 4\,fac8c\,\pi\cos(\beta)^2 - 16\,fac8e\,\pi\cos(\beta)^2 + 4\,fac3c\,\pi^2\cos(\beta)^2 - 12\,fac3e\,\pi^2\cos(\beta)^2 \\
&\quad - 4\,fac4e\,\pi^2\cos(\beta)^2 - 4\,fac5c\,\pi^2\cos(\beta)^2 + 16\,fac5e\,\pi^2\cos(\beta)^2 - 4\,fac6c\,\pi^2\cos(\beta)^2 \\
&\quad + 16\,fac6e\,\pi^2\cos(\beta)^2 - 4\,fac7c\,\pi^2\cos(\beta)^2 + 16\,fac7e\,\pi^2\cos(\beta)^2 + 4\,fac9a\,\pi^2\cos(\beta)^2 \\
&\quad - 20\,fac9c\,\pi^2\cos(\beta)^2 + 64\,fac9e\,\pi^2\cos(\beta)^2 + 4\,fac8e\,\pi\sin(\beta)^2 + 1\,fac3a\,\pi^2\sin(\beta)^2
\end{aligned}
$$

$$- 2\,fac3c\,\pi^2\sin(\beta)^2 + 3\,fac3e\,\pi^2\sin(\beta)^2 - 1\,fac4a\,\pi^2\sin(\beta)^2 + 2\,fac4c\,\pi^2\sin(\beta)^2$$
$$+ 1\,fac4e\,\pi^2\sin(\beta)^2 - 4\,fac5e\,\pi^2\sin(\beta)^2 - 4\,fac6e\,\pi^2\sin(\beta)^2 - 4\,fac7e\,\pi^2\sin(\beta)^2$$
$$+ 8\,fac9c\,\pi^2\sin(\beta)^2 - 16\,fac9e\,\pi^2\sin(\beta)^2$$

$$s2s3^* = i[8\,facld\,\pi^2\sin(\beta)^3 + 2\,fac2b\,\pi^2\sin(\beta)^3 - 2\,fac2d\,\pi^2\sin(\beta)^3]$$

$$s1s4^* = i[-8\,facld\,\pi^2\sin(\beta) - 2\,fac2b\,\pi^2\sin(\beta) + 2\,fac2d\,\pi^2\sin(\beta)]$$

$$s2s4^* = i[-8\,facld\,\pi^2\sin(\beta)^3 - 2\,fac2b\,\pi^2\sin(\beta)^3 + 2\,fac2d\,\pi^2\sin(\beta)^3]$$

$$s1s3^* = i[8\,facld\,\pi^2\sin(\beta) + 2\,fac2b\,\pi^2\sin(\beta) - 2\,fac2d\,\pi^2\sin(\beta)]$$

$$s1s2^* = 4\,fac8c\,\pi\cos(\beta)^2 - 16\,fac8e\,\pi\cos(\beta)^2 + 4\,fac3c\,\pi^2\cos(\beta)^2 - 12\,fac3e\,\pi^2\cos(\beta)^2$$
$$+ 4\,fac4c\,\pi^2\cos(\beta)^2 - 4\,fac4e\,\pi^2\cos(\beta)^2 + 16\,fac5e\,\pi^2\cos(\beta)^2 + 16\,fac6e\,\pi^2\cos(\beta)^2$$
$$+ 4\,fac7a\,\pi^2\cos(\beta)^2 - 12\,fac7c\,\pi^2\cos(\beta)^2 + 16\,fac7e\,\pi^2\cos(\beta)^2 - 16\,fac9c\,\pi^2\cos(\beta)^2$$
$$+ 64\,fac9e\,\pi^2\cos(\beta)^2 - 4\,fac8e\,\pi\sin(\beta)^2 - 1\,fac3a\,\pi^2\sin(\beta)^2 + 2\,fac3c\,\pi^2\sin(\beta)^2$$
$$- 3\,fac3e\,\pi^2\sin(\beta)^2 - 3\,fac4a\,\pi^2\sin(\beta)^2 + 6\,fac4c\,\pi^2\sin(\beta)^2 - 1\,fac4e\,\pi^2\sin(\beta)^2$$
$$- 4\,fac5c\,\pi^2\sin(\beta)^2 + 4\,fac5e\,\pi^2\sin(\beta)^2 - 4\,fac6c\,\pi^2\sin(\beta)^2 + 4\,fac6e\,\pi^2\sin(\beta)^2$$
$$- 4\,fac7c\,\pi^2\sin(\beta)^2 + 4\,fac7e\,\pi^2\sin(\beta)^2 + 16\,fac9e\,\pi^2\sin(\beta)^2$$

$$s3s4^* = 4\,fac8c\,\pi\cos(\beta)^2 - 16\,fac8e\,\pi\cos(\beta)^2 + 4\,fac3c\,\pi^2\cos(\beta)^2 - 12\,fac3e\,\pi^2\cos(\beta)^2$$
$$- 4\,fac4e\,\pi^2\cos(\beta)^2 - 4\,fac5c\,\pi^2\cos(\beta)^2 + 16\,fac5e\,\pi^2\cos(\beta)^2 - 4\,fac6c\,\pi^2\cos(\beta)^2$$
$$+ 16\,fac6e\,\pi^2\cos(\beta)^2 - 4\,fac7c\,\pi^2\cos(\beta)^2 + 16\,fac7e\,\pi^2\cos(\beta)^2 + 4\,fac9a\,\pi^2\cos(\beta)^2$$
$$- 20\,fac9c\,\pi^2\cos(\beta)^2 + 64\,fac9e\,\pi^2\cos(\beta)^2 - 4\,fac8e\,\pi\sin(\beta)^2 - 1\,fac3a\,\pi^2\sin(\beta)^2$$
$$+ 2\,fac3c\,\pi^2\sin(\beta)^2 - 3\,fac3e\,\pi^2\sin(\beta)^2 + 1\,fac4a\,\pi^2\sin(\beta)^2 - 2\,fac4c\,\pi^2\sin(\beta)^2$$
$$- 1\,fac4e\,\pi^2\sin(\beta)^2 + 4\,fac5e\,\pi^2\sin(\beta)^2 + 4\,fac6e\,\pi^2\sin(\beta)^2 + 4\,fac7e\,\pi^2\sin(\beta)^2$$
$$- 8\,fac9c\,\pi^2\sin(\beta)^2 + 16\,fac9e\,\pi^2\sin(\beta)^2$$

$$s2s1^* = 4\,fac8c\,\pi\cos(\beta)^2 - 16\,fac8e\,\pi\cos(\beta)^2 + 4\,fac3c\,\pi^2\cos(\beta)^2 - 12\,fac3e\,\pi^2\cos(\beta)^2$$
$$+ 4\,fac4c\,\pi^2\cos(\beta)^2 - 4\,fac4e\,\pi^2\cos(\beta)^2 + 4\,fac5a\,\pi^2\cos(\beta)^2 - 12\,fac5c\,\pi^2\cos(\beta)^2$$
$$+ 16\,fac5e\,\pi^2\cos(\beta)^2 + 4\,fac6a\,\pi^2\cos(\beta)^2 - 12\,fac6c\,\pi^2\cos(\beta)^2 + 16\,fac6e\,\pi^2\cos(\beta)^2$$
$$- 16\,fac7e\,\pi^2\cos(\beta)^2 - 16\,fac9c\,\pi^2\cos(\beta)^2 + 64\,fac9e\,\pi^2\cos(\beta)^2 - 4\,fac8e\,\pi\sin(\beta)^2$$
$$- 1\,fac3a\,\pi^2\sin(\beta)^2 + 2\,fac3c\,\pi^2\sin(\beta)^2 - 3\,fac3e\,\pi^2\sin(\beta)^2 - 3\,fac4a\,\pi^2\sin(\beta)^2$$
$$+ 6\,fac4c\,\pi^2\sin(\beta)^2 - 1\,fac4e\,\pi^2\sin(\beta)^2 - 4\,fac5c\,\pi^2\sin(\beta)^2 + 4\,fac5e\,\pi^2\sin(\beta)^2$$
$$- 4\,fac6c\,\pi^2\sin(\beta)^2 + 4\,fac6e\,\pi^2\sin(\beta)^2 - 4\,fac7c\,\pi^2\sin(\beta)^2 + 4\,fac7e\,\pi^2\sin(\beta)^2$$
$$+ 16\,fac9e\,\pi^2\sin(\beta)^2$$

$$s4s3^* = 4\,fac8c\,\pi\cos(\beta)^2 - 16\,fac8e\,\pi\cos(\beta)^2 + 4\,fac3c\,\pi^2\cos(\beta)^2 - 12\,fac3e\,\pi^2\cos(\beta)^2$$
$$- 4\,fac4e\,\pi^2\cos(\beta)^2 - 4\,fac5c\,\pi^2\cos(\beta)^2 + 16\,fac5e\,\pi^2\cos(\beta)^2 - 4\,fac6c\,\pi^2\cos(\beta)^2$$
$$+ 16\,fac6e\,\pi^2\cos(\beta)^2 - 4\,fac7c\,\pi^2\cos(\beta)^2 + 16\,fac7e\,\pi^2\cos(\beta)^2 + 4\,fac9a\,\pi^2\cos(\beta)^2$$
$$- 20\,fac9c\,\pi^2\cos(\beta)^2 + 64\,fac9e\,\pi^2\cos(\beta)^2 - 4\,fac8e\,\pi\sin(\beta)^2 - 1\,fac3a\,\pi^2\sin(\beta)^2$$

$$+ 2\,fac3c\,\pi^2\sin(\beta)^2 - 3\,fac3e\,\pi^2\sin(\beta)^2 + 1\,fac4a\,\pi^2\sin(\beta)^2 - 2\,fac4c\,\pi^2\sin(\beta)^2$$

$$- 1\,fac4e\,\pi^2\sin(\beta)^2 + 4\,fac5e\,\pi^2\sin(\beta)^2 + 4\,fac6e\,\pi^2\sin(\beta)^2 + 4\,fac7e\,\pi^2\sin(\beta)^2$$

$$- 8\,fac9c\,\pi^2\sin(\beta)^2 + 16\,fac9e\,\pi^2\sin(\beta)^2$$

$$s3s1^* = i[-8\,fac1d\,\pi^2\sin(\beta) - 2\,fac2b\,\pi^2\sin(\beta) + 2\,fac2d\,\pi^2\sin(\beta)]$$

where

$$fac2a = m\,n\,si^2sj^2\,J_0(q),\quad fac2b = m\,n\,si^2sj^2\,J_1(q),$$

$$fac2c = m\,n\,si^2sj^2\,\frac{J_1(q)}{q},\quad fac2d = m\,n\,si^2sj^2\,\frac{J_2(q)}{q},$$

$$fac2e = m\,n\,si^2sj^2\,\frac{J_2(q)}{q^2},\quad fac1a = li\,lj\,n\,si\,sj\,J_0(q),$$

$$fac1b = li\,lj\,n\,si\,sj\,J_1(q),\quad fac1c = li\,lj\,n\,si\,sj\,\frac{J_1(q)}{q},$$

$$fac1d = li\,lj\,n\,si\,sj\,\frac{J_2(q)}{q},\quad fac1e = li\,lj\,n\,si\,sj\,\frac{J_2(q)}{q^2},$$

$$fac9a = li\,lj\,m\,si\,sj\,J_0(q),\quad fac9b = li\,lj\,m\,si\,sj\,J_1(q),$$

$$fac9c = li\,lj\,m\,si\,sj\,\frac{J_1(q)}{q},\quad fac9d = li\,lj\,m\,si\,sj\,\frac{J_2(q)}{q},$$

$$fac9e = li\,lj\,m\,si\,sj\,\frac{J_2(q)}{q^2},\quad fac3a = m^2\,si^2\,sj^2\,J_0(q),$$

$$fac3b = m^2\,si^2\,sj^2\,J_1(q),\quad fac3c = m^2\,si^2\,sj^2\,\frac{J_1(q)}{q},$$

$$fac3d = m^2\,si^2\,sj^2\,\frac{J_2(q)}{q},\quad fac3e = m^2\,si^2\,sj^2\,\frac{J_2(q)}{q^2},$$

$$fac4a = n^2\,si^2\,sj^2\,J_0(q),\quad fac4b = n^2\,si^2\,sj^2\,J_1(q),$$

$$fac4c = n^2\,si^2\,sj^2\,\frac{J_1(q)}{q},\quad fac4d = n^2\,si^2\,sj^2\,\frac{J_2(q)}{q},$$

$$fac4e = n^2\,si^2\,sj^2\,\frac{J_2(q)}{q^2},\quad fac5a = li^2\,n^2\,sj^2\,J_0(q),$$

$$fac5b = li^2\,n^2\,sj^2\,J_1(q),\quad fac5c = li^2\,n^2\,sj^2\,\frac{J_1(q)}{q},$$

$$fac5d = li^2\,n^2\,sj^2\,\frac{J_2(q)}{q},\quad fac5e = li^2\,n^2\,sj^2\,\frac{J_2(q)}{q^2},$$

$$fac6a = li^2\,m^2\,sj^2\,J_0(q),\quad fac6b = li^2\,m^2\,sj^2\,J_1(q),$$

$$fac6c = li^2\,m^2\,sj^2\,\frac{J_1(q)}{q},\quad fac6d = li^2\,m^2\,sj^2\,\frac{J_2(q)}{q},$$

$$fac6e = li^2\,m^2\,sj^2\,\frac{J_2(q)}{q^2},\quad fac7a = lj^2\,si^2\,J_0(q),$$

$$fac7b = lj^2\,si^2\,J_1(q),\quad fac7c = lj^2\,si^2\,\frac{J_1(q)}{q},$$

$$\text{fac7d} = \text{lj}^2\ \text{si}^2\ \frac{J_2(q)}{q}, \quad \text{fac7e} = \text{lj}^2\ \text{si}^2\ \frac{J_2(q)}{q^2},$$

$$\text{fac8a} = \text{li}^2\ \text{lj}^2\ J_0(q), \quad \text{fac8b} = \text{li}^2\ \text{lj}^2\ J_1(q),$$

$$\text{fac8c} = \text{li}^2\ \text{lj}^2\ \frac{J_1(q)}{q}, \quad \text{fac8d} = \text{li}^2\ \text{lj}^2\ \frac{J_2(q)}{q},$$

$$\text{fac8e} = \text{li}^2\ \text{lj}^2\ \frac{J_2(q)}{q^2};$$

Appendix II.

The contour is defined in terms of the parameter u. n is the number of turns for a single, simple helix. The following equations define the contour of the two turn plectonemic helix. The four turn helix is defined with n=4 and d=0.8. The Display command creates an image file, "3dg", that can be plotted. This Mathematica code is readily to other computer languages.

```
n = 2
d = 1.6
a3 = 14
a := (n*d + 1)/2
b := (n*d)/2
del = 4
DNAaxe1[u_] := {a*Sin[(n*Pi*(u + 1 - 1/(2*n)))/a], Sin[n*Pi*u], f3[u]}

f3[u_] := 8*a3*Sum[Cos[((2*j - 1)*Pi*(u - d/2))/(1 + d)]/(Pi*(2*j - 1))^2,
   {j, 1, del}]



DNAaxe2[u_] := {-Cos[n*Pi*u], Sin[n*Pi*u], f3[u]}

DNAaxe3[u_] := {-(a*Sin[(n*Pi*(u + 1/(2*n)))/a]), Sin[n*Pi*u], f3[u]}

DNAaxe4[u_] := {-(a*Sin[(n*Pi*(u + 1/(2*n)))/a]), b*Sin[(n*Pi*u)/b], f3[u]}


DNAaxe5[u_] := {-(a*Sin[(n*Pi*(u + 1/(2*n)))/a]), Sin[n*Pi*(u - d)], f3[u]}

DNAaxe6[u_] := {Cos[n*Pi*(u - d)], Sin[n*Pi*(u - d)], f3[u]}

DNAaxe7[u_] := {a*Sin[(n*Pi*(u - 1 - d + 1/(2*n)))/a], Sin[n*Pi*(u - d)],
  f3[u]}

DNAaxe8[u_] := {a*Sin[(n*Pi*(u - 1 - d + 1/(2*n)))/a],
  b*Sin[(n*Pi*(u - 1 - d))/b], f3[u]}
xh = {1,0,0}
yh = {0,1,0}
zh = {0,0,1}
f[u_] :=
Which[u<(-1+(1/(2n))),DNAaxe1[u].xh,
u<(-(1/(2n))),DNAaxe2[u].xh,
u<0,DNAaxe3[u].xh,
u<d,DNAaxe4[u].xh,
u<(d+(1/(2n))),DNAaxe5[u].xh,
u<(1+d-(1/(2n))),DNAaxe6[u].xh,
u<(1+d),DNAaxe7[u].xh,
u<=(1+2d),DNAaxe8[u].xh,True,0]
```

```
g[u_] :=
Which[u<(-1+(1/(2n))),DNAaxe1[u].yh,
u<(-(1/(2n))),DNAaxe2[u].yh,
u<0,DNAaxe3[u].yh,
u<d,DNAaxe4[u].yh,
u<(d+(1/(2n))),DNAaxe5[u].yh,
u<(1+d-(1/(2n))),DNAaxe6[u].yh,
u<(1+d),DNAaxe7[u].yh,
u<=(1+2d),DNAaxe8[u].yh,True,0]
h[u_] :=
Which[u<(-1+(1/(2n))),DNAaxe1[u].zh,
u<(-(1/(2n))),DNAaxe2[u].zh,
u<0,DNAaxe3[u].zh,
u<d,DNAaxe4[u].zh,
u<(d+(1/(2n))),DNAaxe5[u].zh,
u<(1+d-(1/(2n))),DNAaxe6[u].zh,
u<(1+d),DNAaxe7[u].zh,
u<=(1+2d),DNAaxe8[u].zh,True,0]
Display["./3dg", ParametricPlot3D[{f[u],g[u],h[u]}, {u,-1,(1+2d)} ]]
Quit
```

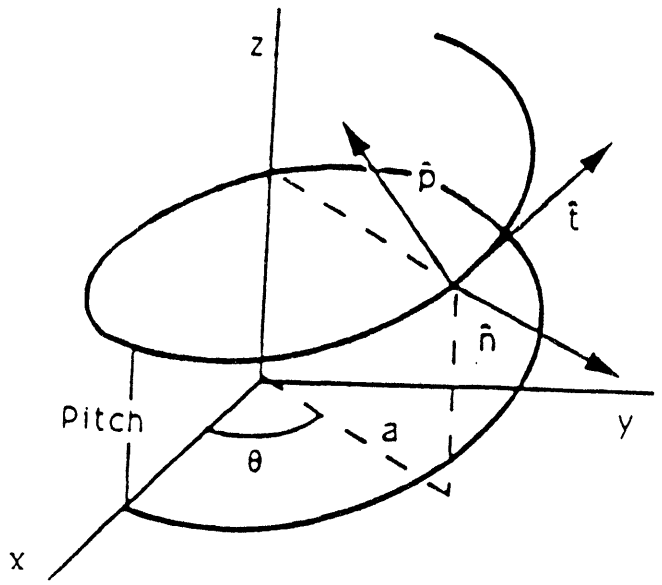

Figure 3.1 The continuous helix. The helix is characterized by a radius, a, and pitch, P. The components of the polarizability parallel($\hat{p}$), perpendicular ($\hat{n}$) , and tangent ($\hat{t}$) to the helix are shown.

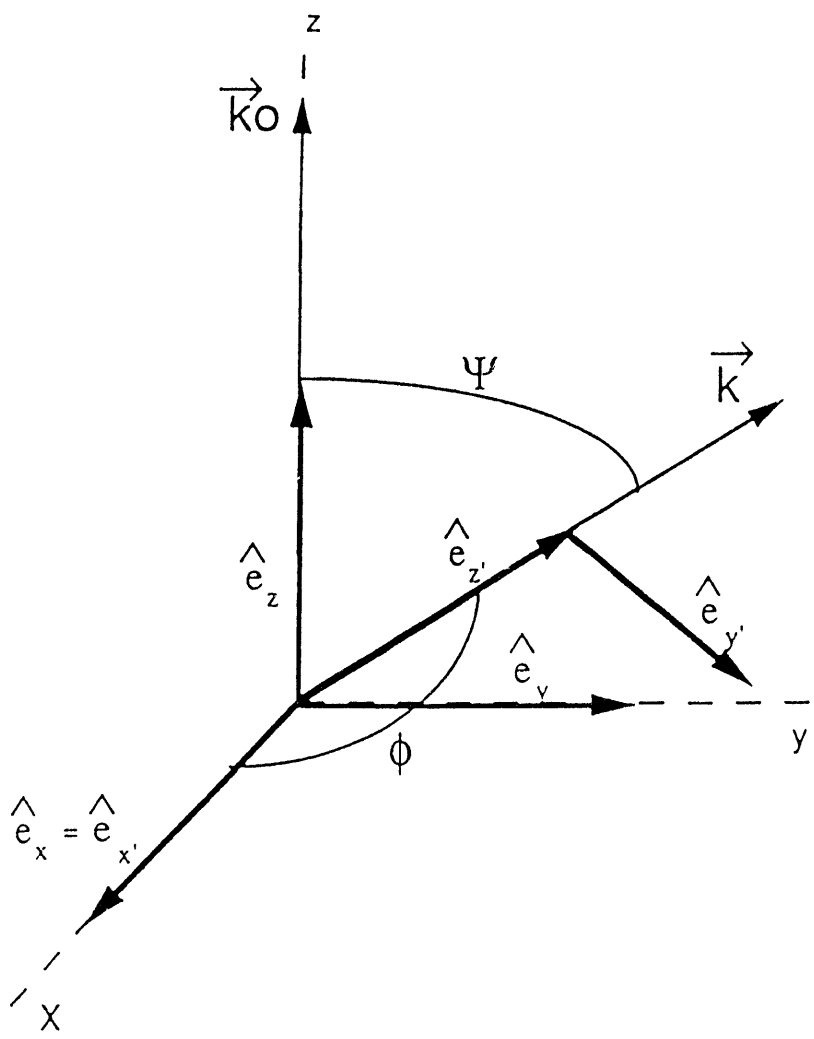

Figure 3.2 The coordinate systems of the incidence frame and observation frames. The incidence frame is set along an arbitrary laboratory-fixed frame x,y,z. The incident light described by by the propagation vector $\vec{k}_o$, is shown along the z axis. The scattered light, described by the propagation vector $\vec{k}$, is defined by the angles ψ and ϕ. ϕ is the angle between the x-axis and $\vec{k}$. ψ is is the angle between the z-axis and the projection of $\vec{K}$ onto the z-y plane. When $\phi = \pi/2$, (as shown) the scattering is observed in the y-z plane as a function of the scattering angle = ψ.

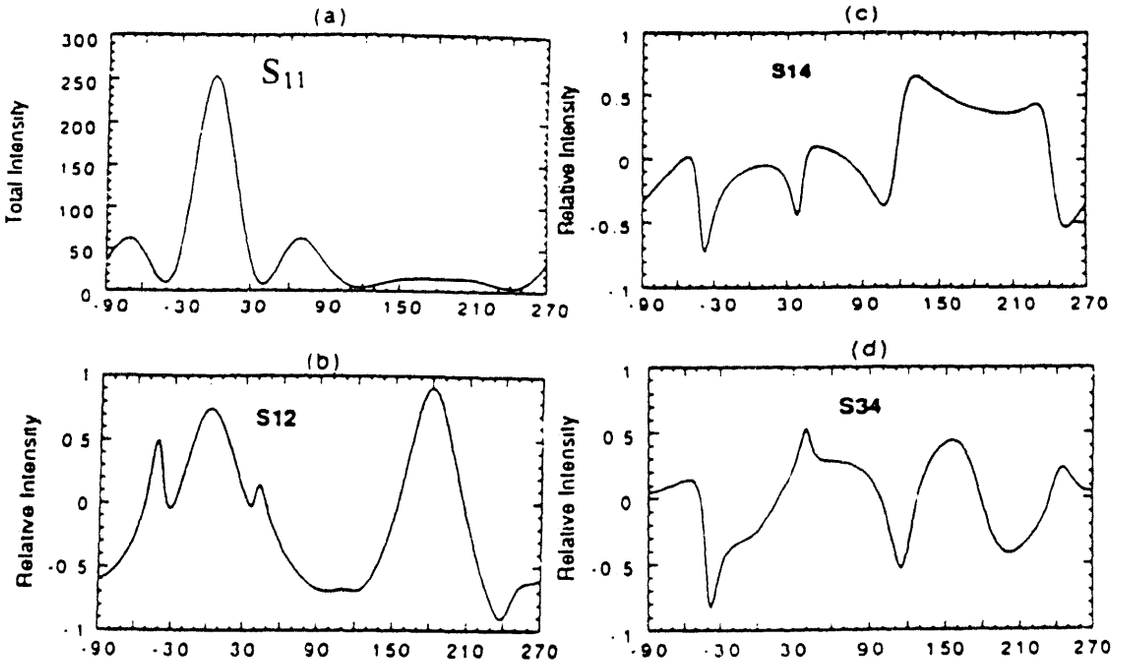

Figure 3.3 Scattering predicted for a single helix with length = 20, radius = pitch = 1, and light incident perpendicular to the helix with wavelength = 2 for a generalized polarizability when $\phi \neq \pi/2$. The predicted intensities are plotted over 360°. $\phi = 1$ radian.

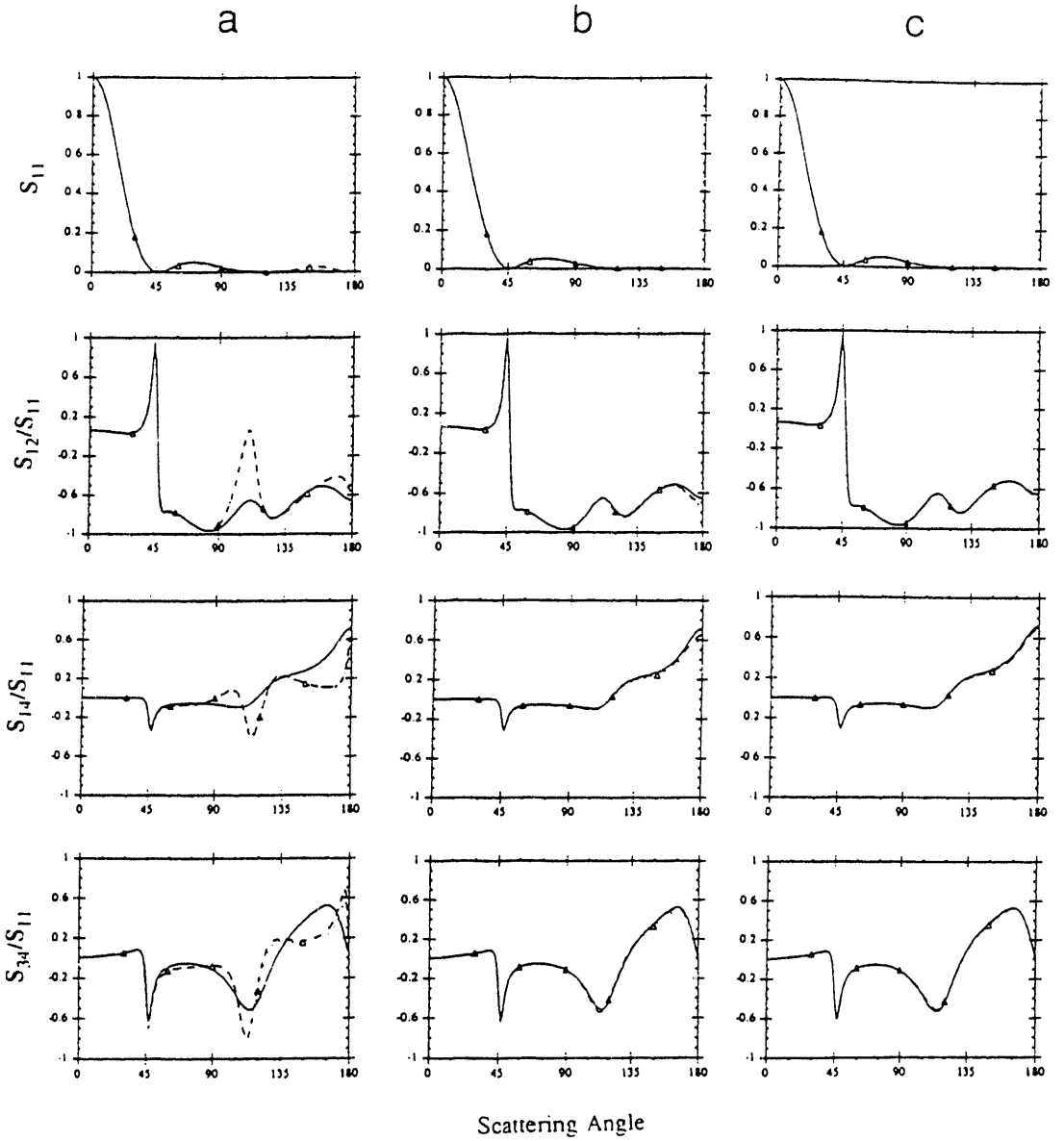

Figure 3.4 Mueller matrix elements for a single stranded helix with varying number of subunits. —— Continuous-Born , ···△··· Independent-Dipole, ------- Coupled-Dipole. The helix is oriented at 45 ° with respect to the scattering plane in the x-z plane. Helix pitch, radius and length = 500 nm and λ = 1000 nm. Dielectric constant ε_{avg} = 1.4, ε = 1. The spheroidal subunits are four times longer in the tangential direction than they are in the parallel, and perpendicular direction (Aspect ratio = 4). For the continuous helix α_{tt} = 1.348 x 10^5 nm^3 and $\alpha_{nn} = \alpha_{pp}$ = 1.026 x 10^5 nm^3 in a, b, and c. (a) 7 subunits are used for the calculations involving point polarizable groups. The subunits are 100 nm thick so that α_{tt} = 1.348 x 10^5 nm^3 and $\alpha_{nn} = \alpha_{pp}$ = 1.026 x 10^5 nm^3. (b) 15 subunits, 50 nm thick, α_{tt} = 1.684 x 10^4 nm^3 and $\alpha_{nn} = \alpha_{pp}$ = 1.283 x 10^4 nm^3. (c) 31 subunits, 25 nm thick, α_{tt} = 2.105 x 10^3 nm^3 and $\alpha_{nn} = \alpha_{pp}$ = 1.604 x 10^3 nm^3.

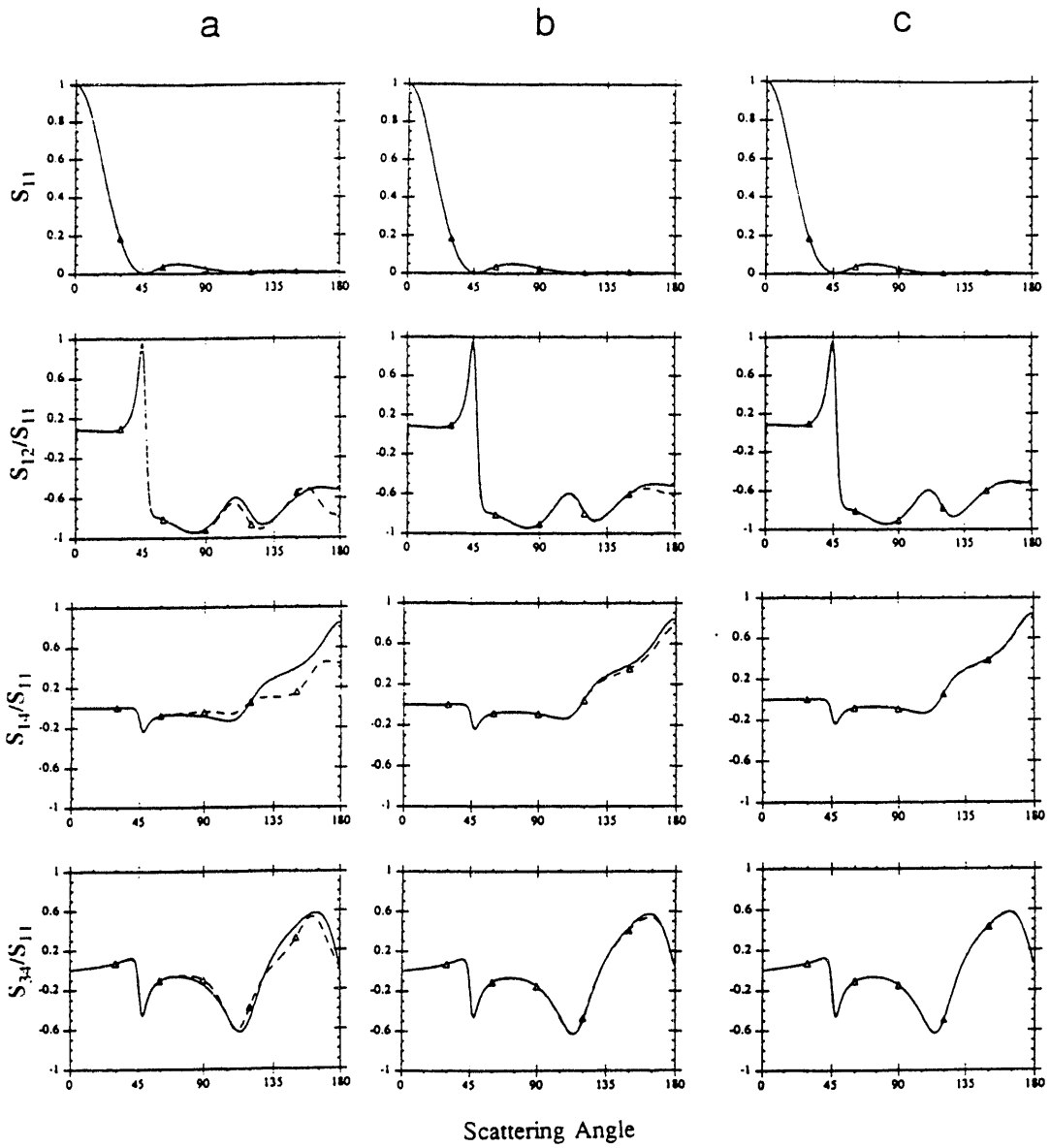

Figure 3.5 Mueller matrix elements for a thin helix with varying number of subunits. —— Continuous-Born , ···△··· Independent-Dipole, ------- Coupled-Dipole. The helix is oriented at 45 ° with respect to the scattering plane in the x-z plane. Helix pitch, radius and length = 500 nm and λ = 1000 nm. Dielectric constant ε_{avg} = 1.4, ε = 1. Aspect ratio of the subunits = 198.8. For the continuous helix $\alpha_{tt} = 5.665 \times 10^{1}$ nm^3 and $\alpha_{nn} = \alpha_{pp} = 3.969 \times 10^{1}$ nm^3 in a, b, and c. (a) 8 subunits are used for the calculations involving point polarizable groups. The subunits are 2 nm thick so that $\alpha_{tt} = 5.665 \times 10^{1}$ nm^3 and $\alpha_{nn} = \alpha_{pp} = 3.969 \times 10^{1}$ nm^3. (b) 16 subunits, 1 nm thick, $\alpha_{tt} = 7.081$ nm^3 and $\alpha_{nn} = \alpha_{pp} = 4.962$ nm^3. (c) 31 subunits, 0.5 nm thick, $\alpha_{tt} = 0.8852$ nm^3 and $\alpha_{nn} = \alpha_{pp} = 0.6202$ nm^3.

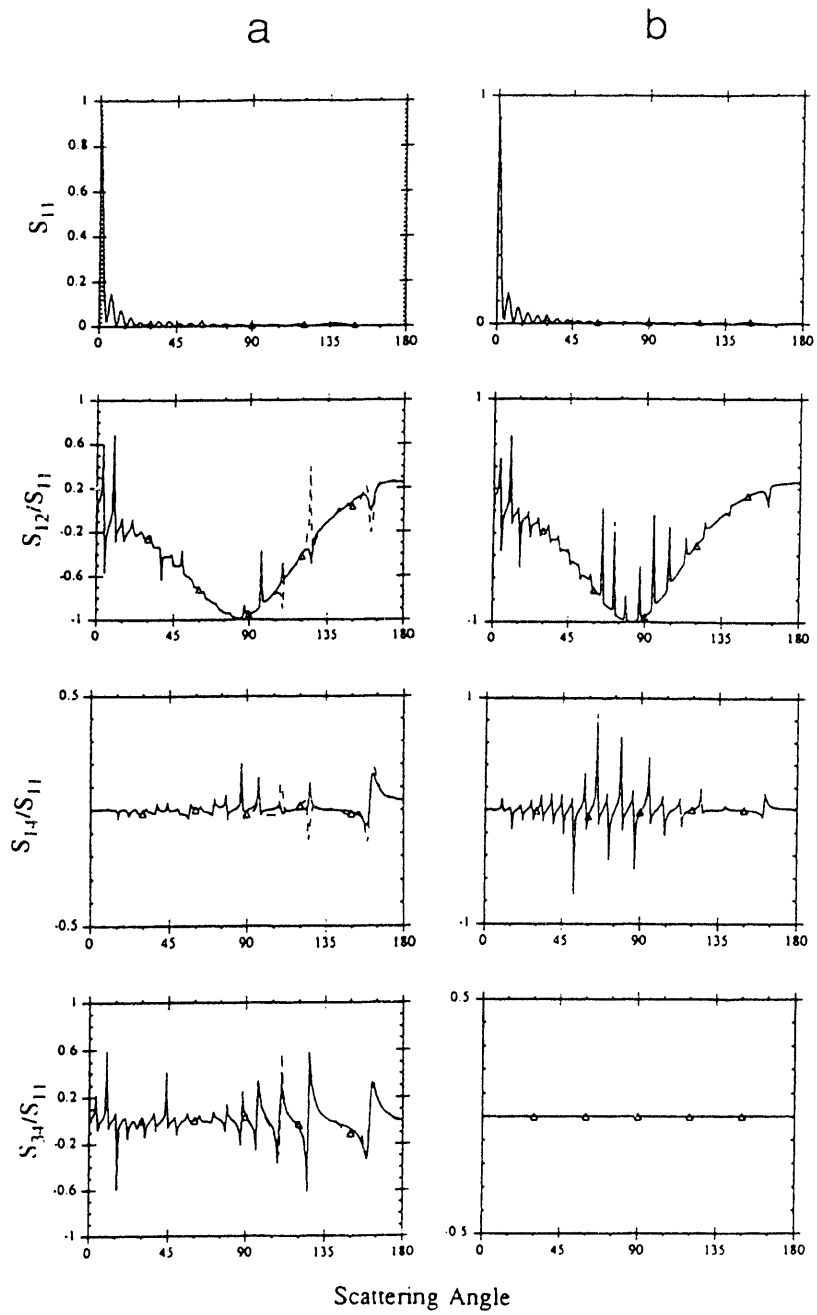

Figure 3.6 Mueller matrix elements for a large helix at different orientations. ——— Continuous-Born , ···△··· Independent-Dipole, ------- Coupled-Dipole. Helix pitch, radius and length = 500 nm and λ = 100 nm. Dielectric constant ε_{avg} = 1.36, ε = 1. Aspect ratio of the subunits = 198.8. 320 subunits are used for the calculations involving point polarizable groups. The subunits are 0.05 nm thick so that $\alpha_{tt} = 5.301 \times 10^{-3}$ nm^3 and $\alpha_{nn} = \alpha_{pp} = 4.016 \times 10^{-3}$ nm^3. These same values for α are used for the continuous helix. (a) The helix is oriented at 45 ° with respect to the scattering plane in the x-z plane. (b) The helix is oriented along the z-axis.

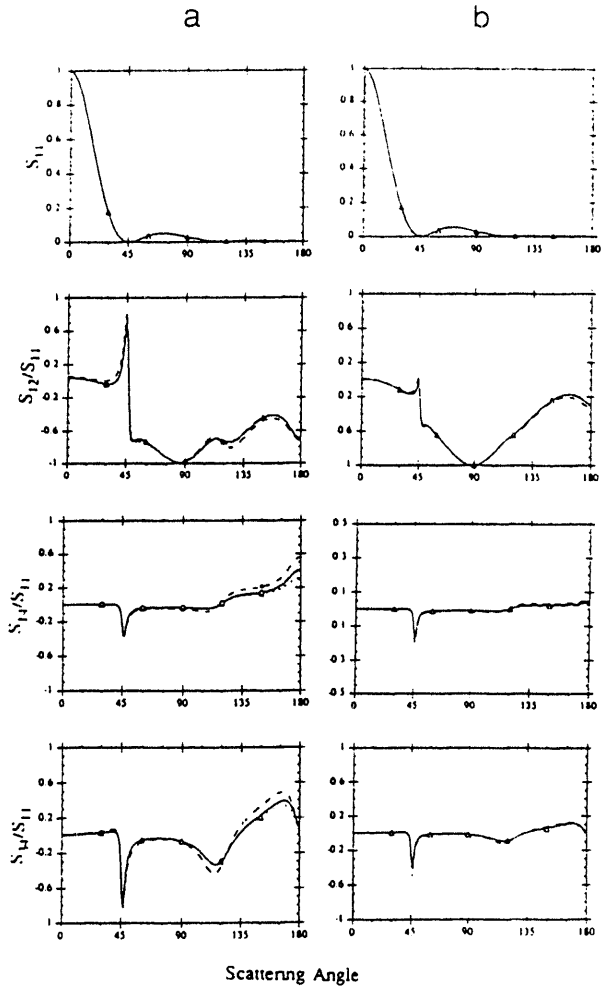

Figure 3.7 Mueller matrix elements of a helix for different values of ε. ——— Continuous-Born , ··△·· Independent-Dipole, ------- Coupled-Dipole. Helix pitch, radius and length = 500 nm and λ = 1000 nm. The helix is oriented at 45 ° with respect to the scattering plane in the x-z plane. Aspect ratio of the subunits = 2. (a) Dielectric constant ε_{avg} = 1.4 in a medium with ε = 1. 15 subunits are used for the calculations involving point polarizable groups. The subunits are 100 nm thick, $\alpha_{tt} = 6.274 \times 10^4$ nm^3 and $\alpha_{nn} = \alpha_{pp} = 5.315 \times 10^4$ nm^3. These same values for α are used for the continuous helix. Two additional curves are shown in the plot of S_{14}, where 31 subunits 50 nm wide are used with $\alpha_{tt} = 7.842 \times 10^3$ nm^3 and $\alpha_{nn} = \alpha_{pp} = 6.644 \times 10^3$ nm^3. ··◇·· Independent-Dipole, -◇- Coupled-Dipole. (b) Dielectric constant ε_{avg} = 1.1, ε = 1. 15 subunits, 100 nm thick, $\alpha_{tt} = 1.587 \times 10^4$ nm^3 and $\alpha_{nn} = \alpha_{pp} = 1.518 \times 10^4$ nm^3. These same values for α are used for the continuous helix.

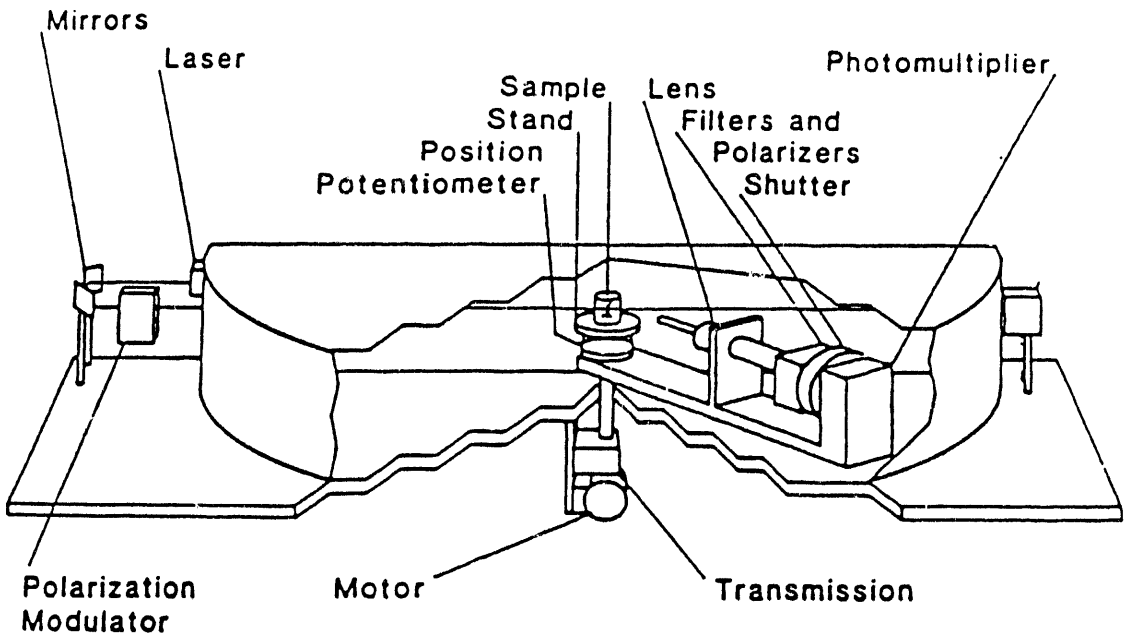

Figure 4.1 The scanning polarization-modulation nephelometer. The Argon-ion laser produces a beam that is reflected by two mirrors and then traverses a polarizer followed by the photoelastic modulator. The beam is then incident upon the sample. Scattered light is detected by a photomultiplier tube mounted on a movable arm. Various analyzers housed in the arm allow all of the Mueller matrix elements to be measured.

Figure 5.1 A scanning electron micrograph of the sperm head of the octopus *Eledone cirrhosa*. Bar is 1 μm.

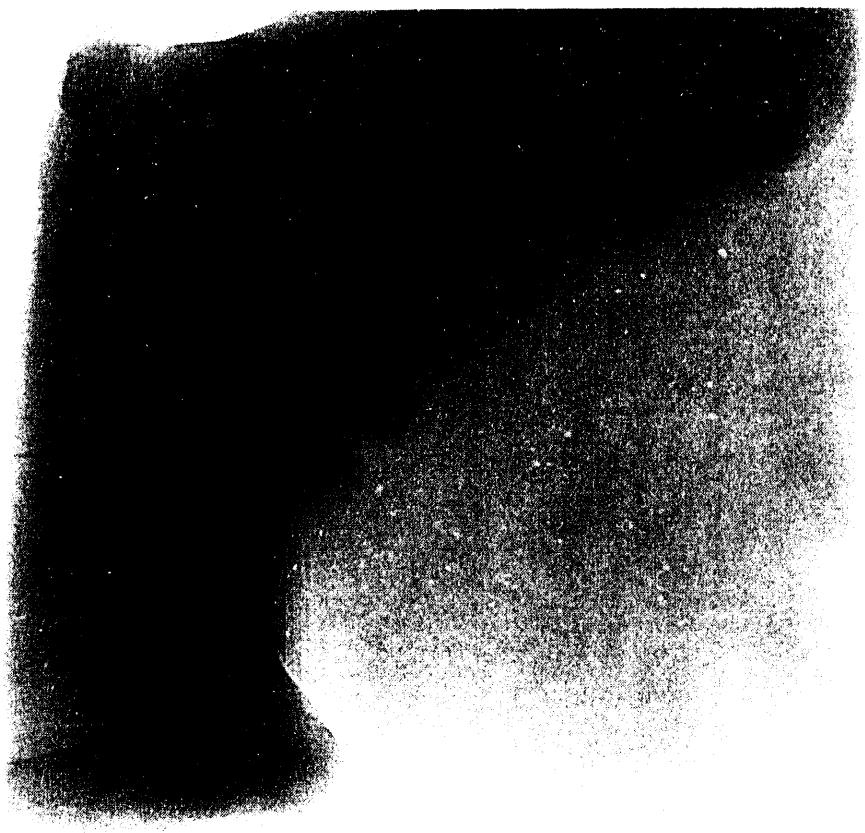

Figure 5.2 A transmission electron micrograph of the sperm head of the octopus *Eledone cirrhosa*. Magnification 320,000. A dense fiber is seen within the screw-like octopus head.

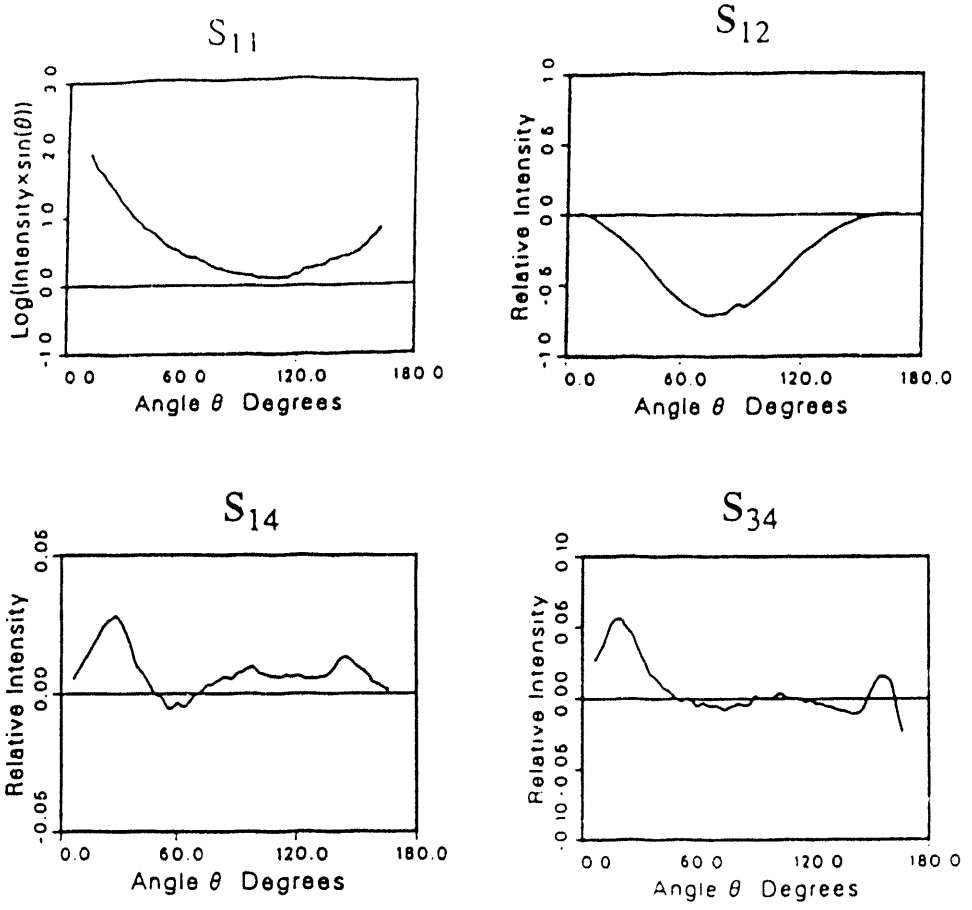

Figure 5.3 Measurements of the Mueller matrix elements from *Eledone cirrhosa*. S_{11} is shown normalized by the intensity of scattering from carbon disulfide at a scattering angle of 90°. The other matrix elements are normalized by S_{11}.

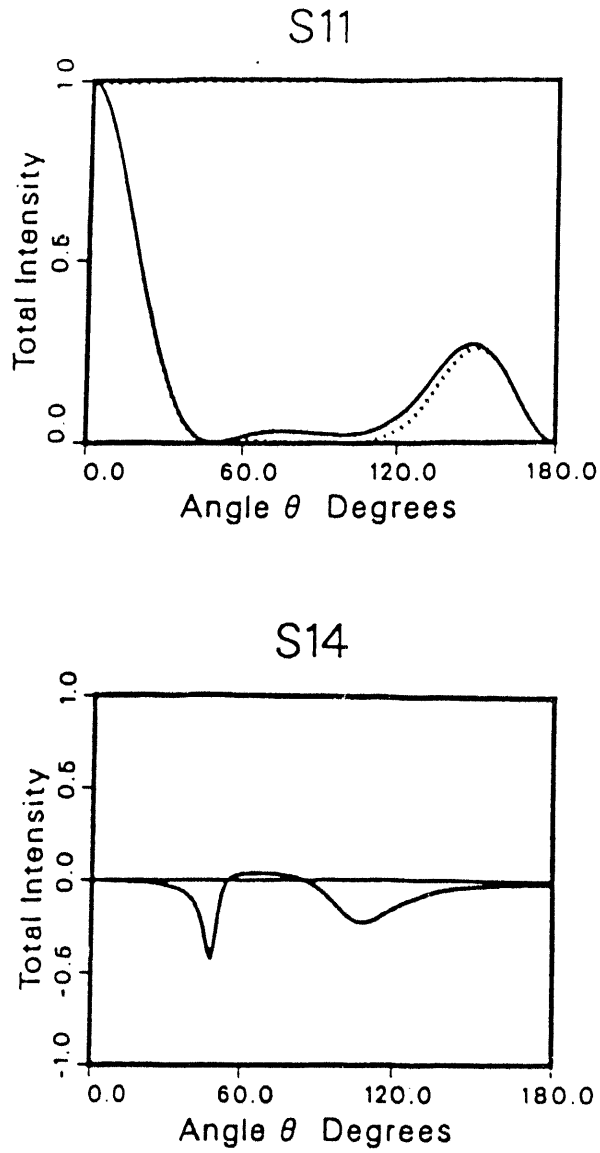

Figure 5.4 Calculated Mueller matrix elements for a single turn of a helix oriented parallel to the incoming light. The helix has a pitch and radius of 250 nm. for a wavelength of 500 nm. The calculation for a single turn of the helix is shown by the continuous curve and the dotted curve represents the calculation for two turns of the helix. a) S_{11}. The S_{11} is shown normalized by its value at the scattering angle 0°. The scattering of the two turn helix is much more forward scattering than the single turn helix as evidenced by its value at 90° b) S_{14}. The matrix element normalized by S_{11} is independent of the number of helix turns.

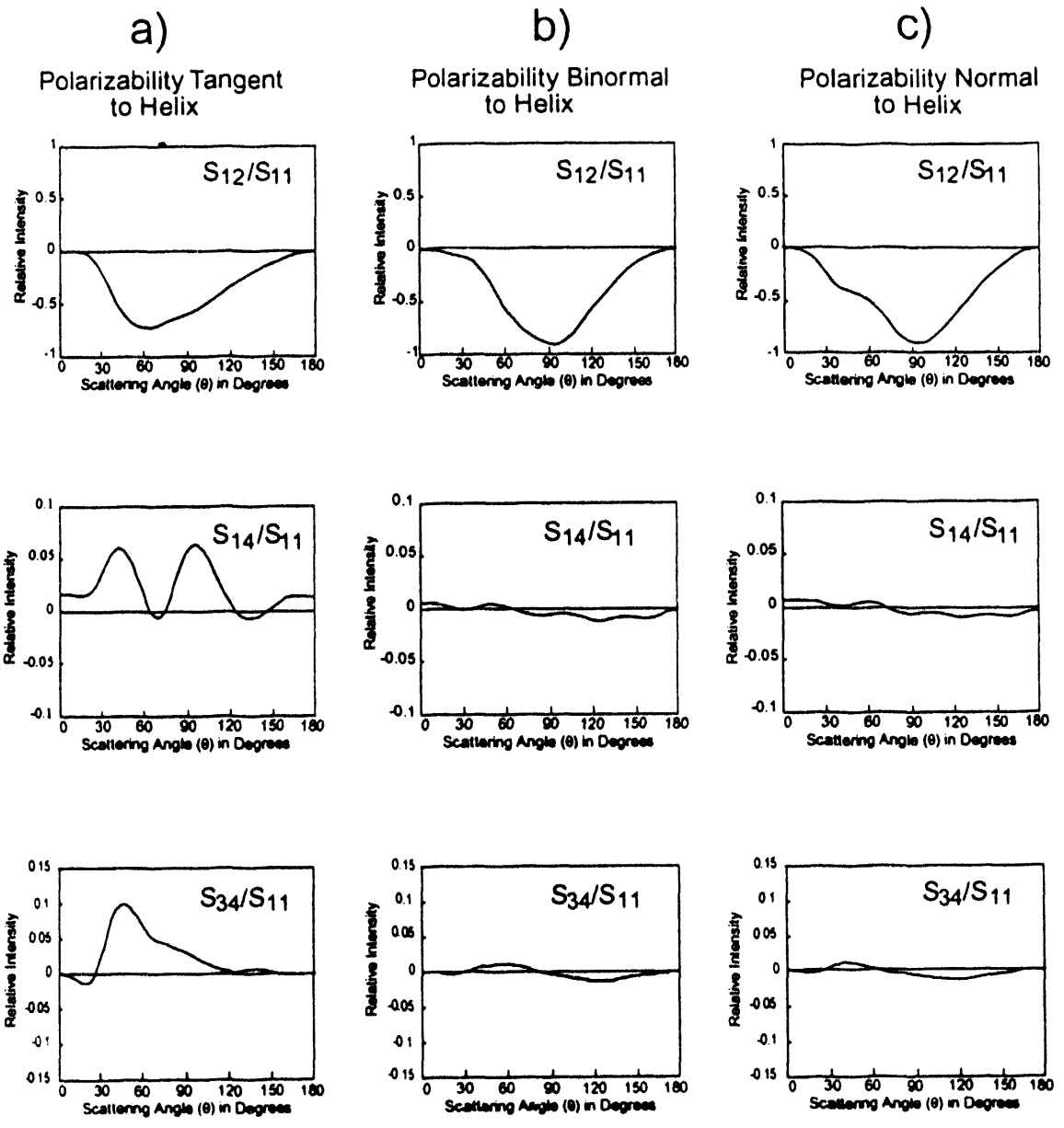

Figure 5.5 Normalized Matrix elements calculated for the model helix in the orientation average. a) The largest strength of the polarizability is close to tangent to the helix; $\zeta_1 = \frac{\pi}{4}$ and $\zeta_2 = \frac{31\pi}{20}$. $\alpha_{tt} = 6{,}433\ nm^3$, $\alpha_{pp} = 2{,}617\ nm^3$, and $\alpha_{nn} = 2{,}617\ nm^3$. b) The largest strength of the polarizability is along the binormal to the helix ($\hat{p}'$) ; $\zeta_1 = \frac{\pi}{4}$ and $\zeta_2 = \frac{31\pi}{20}$. $\alpha_{pp} = 6{,}433\ nm^3$, $\alpha_{tt} = 2{,}617\ nm^3$, and $\alpha_{nn} = 2{,}617\ nm^3$. c) The largest strength of the polarizability is along the normal to the helix ($\hat{n}'$) ; $\zeta_1 = 0$ and $\zeta_2 = \frac{3\pi}{2}$. $\alpha_{nn} = 6{,}433\ nm^3$, $\alpha_{tt} = 2{,}617\ nm^3$, and $\alpha_{pp} = 2{,}617\ nm^3$.

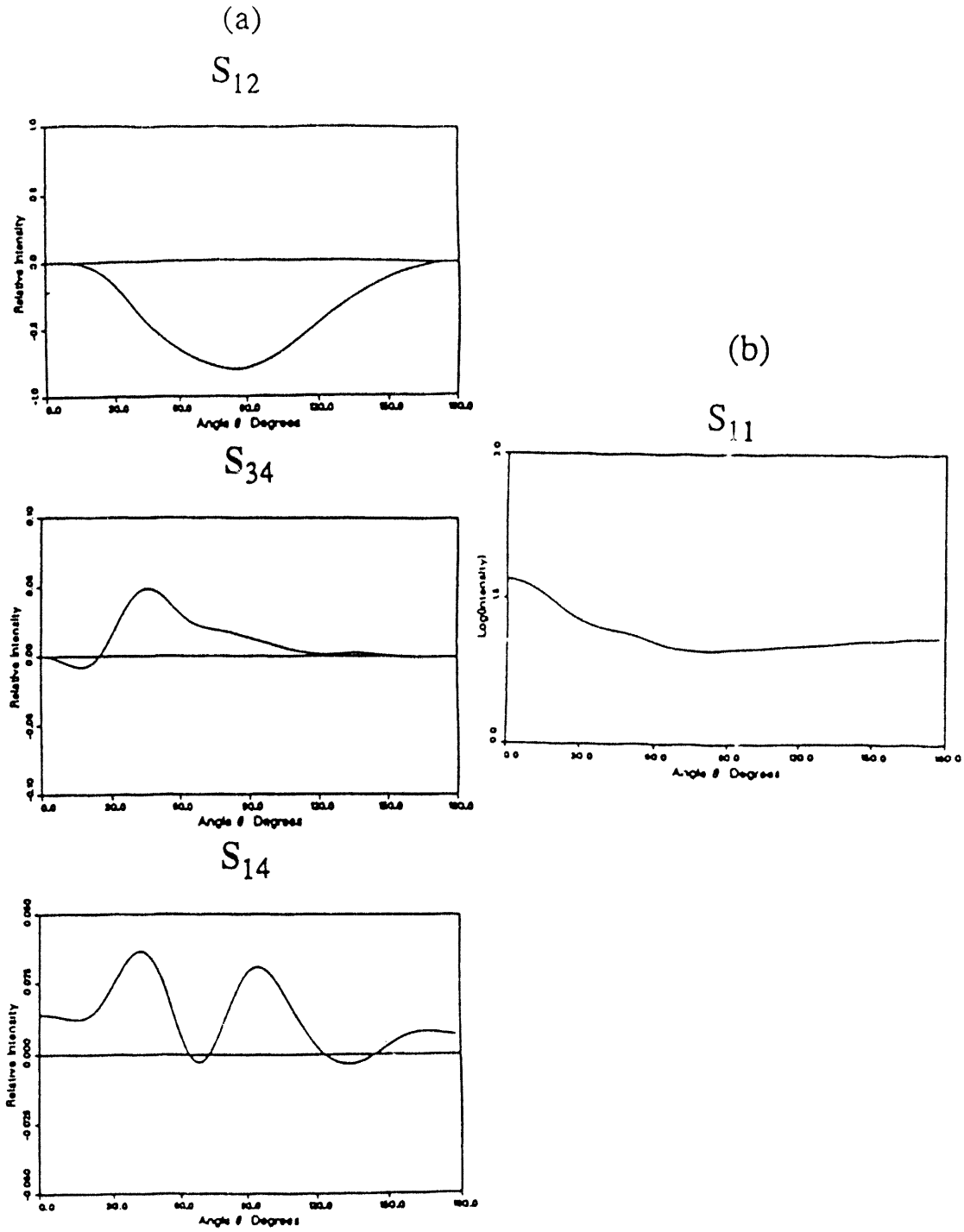

Figure 5.6 The Rayleigh correction. a) The Mueller matrix elements calculated for Figure 5.6a are corrected for the presence of Rayleigh scatterers according to Equations 21 and 22 with $\gamma = 10$. b) The S_{11} for the model helix using the same parameters used to calculate the results shown in Figure 5.5a. This is the S_{11_c} used for the Rayleigh correction.

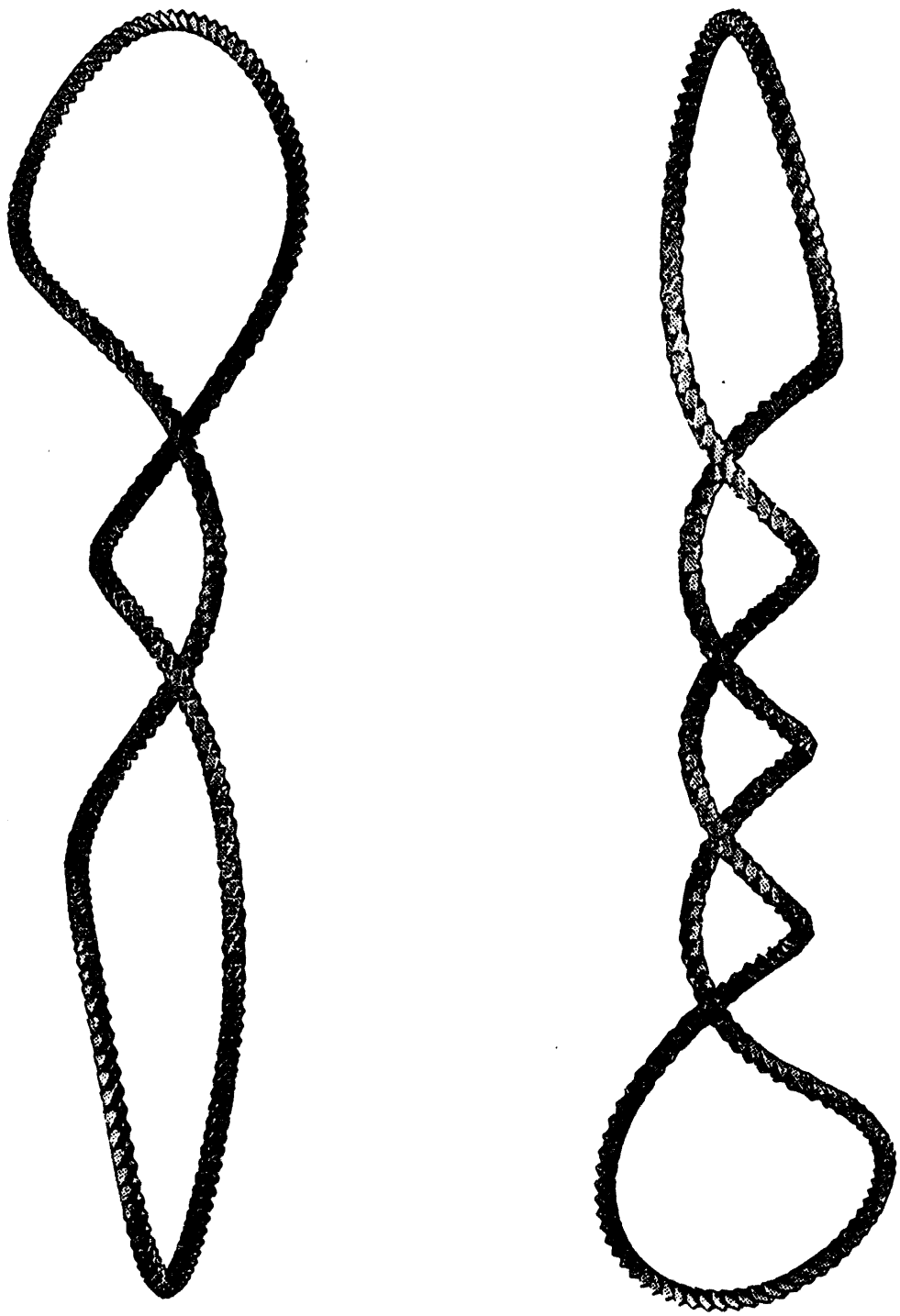

Figure 6.1 The two (left) and four (right) turn helix.

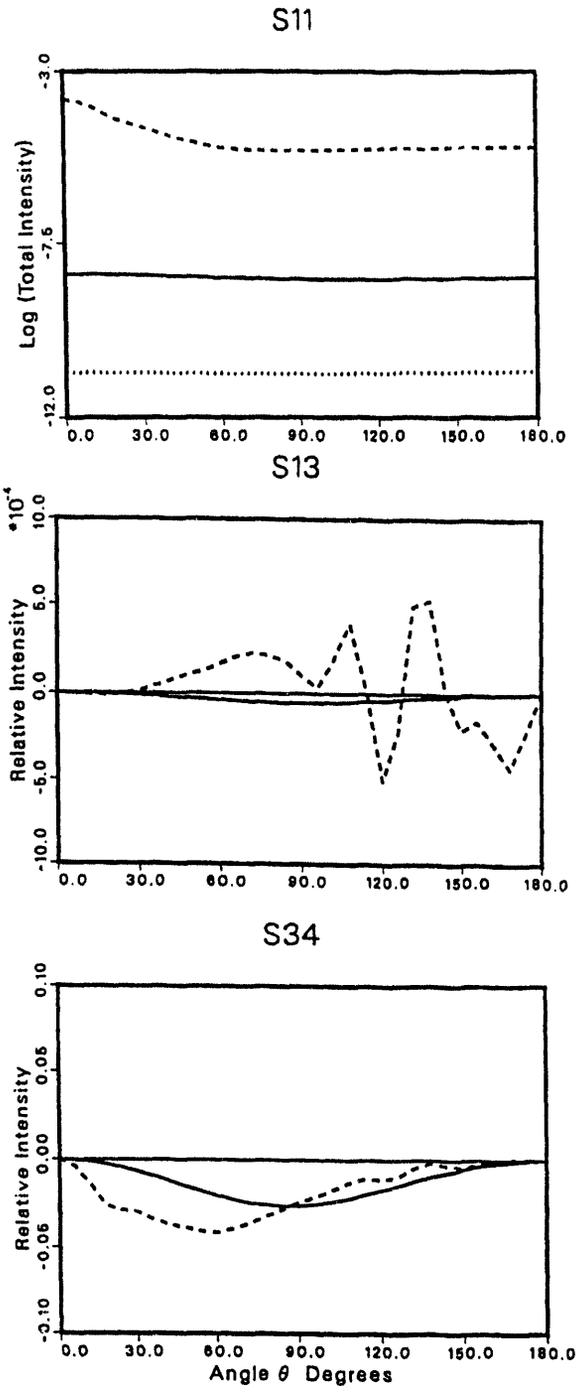

Figure 6.2 Mueller matrix elements calculated for the two turn helix as a function of wavelength. ..... : 633 nm, _____ : 260 nm, ---- : 20 nm. The polarizability strengths used are given in the text. An index of refraction of 1.33 was used at the UV and visible wavelengths and a value of 1.0 was used at 20nm. S_{11} is plotted on a log scale. The other matrix elements are normalized by S_{11}.

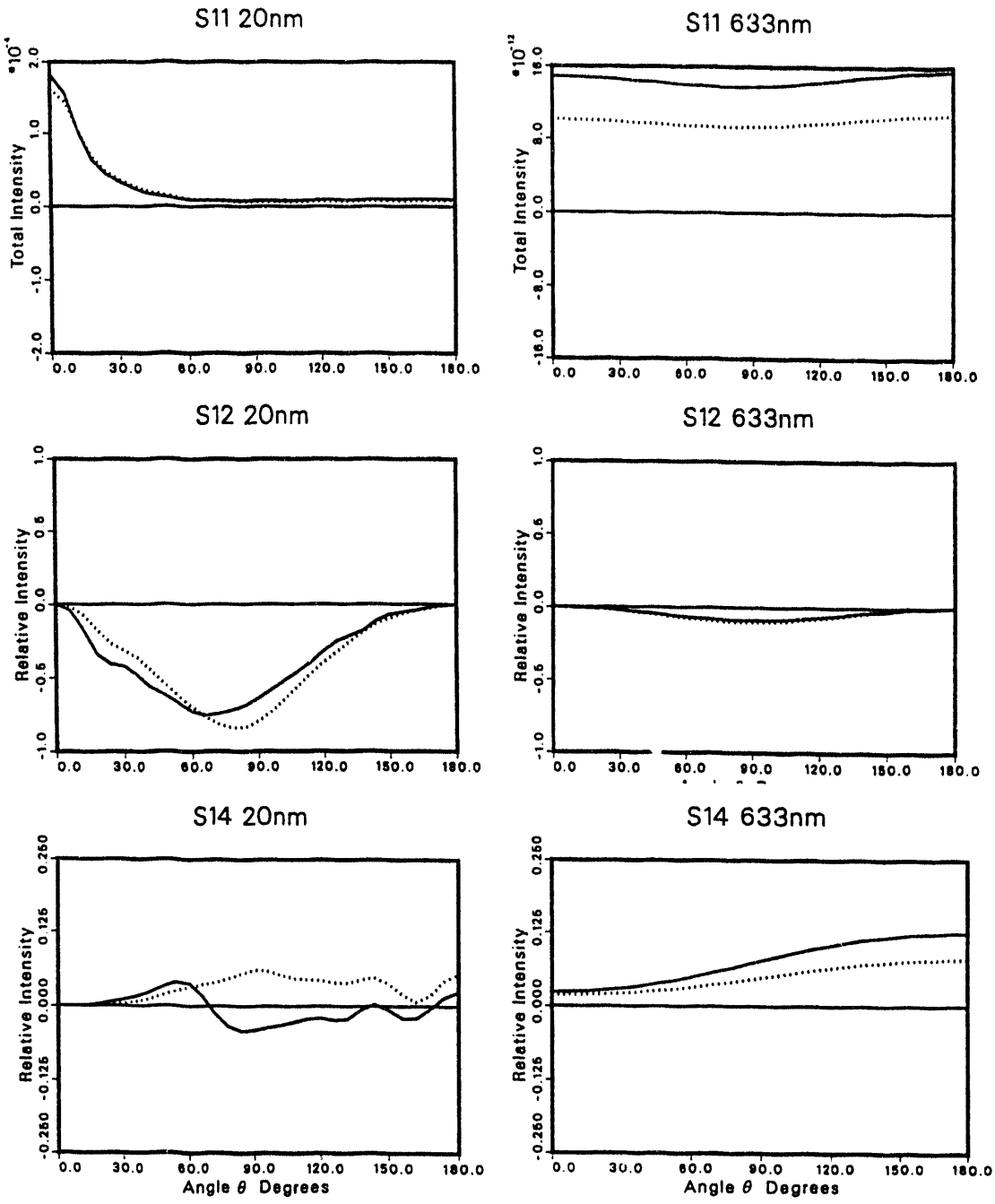

Figure 6.3 The writhe dependence of the Mueller matrix elements. The matrix elements, normalized by S_{11}, are plotted *vs* scattering angle for the two (_____) and four (.....) turn helices. The polarizability strengths at each wavelength are the same as those used for Figure 6.2.

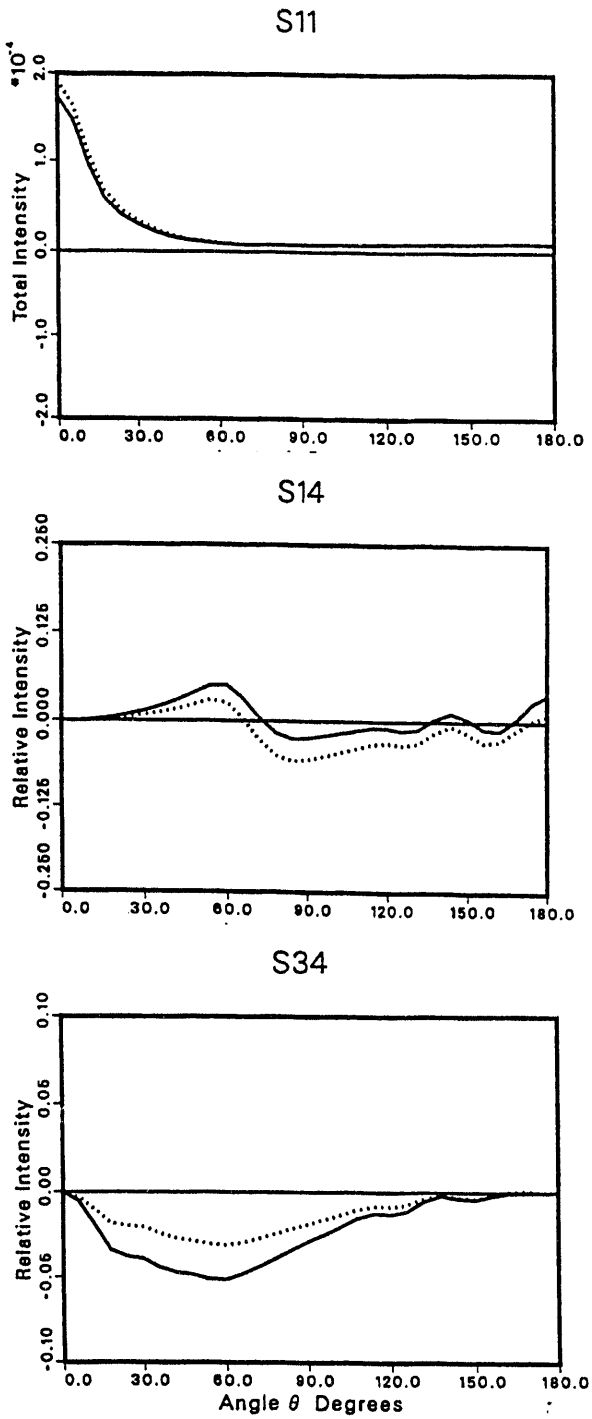

Figure 6.4 Anisotopic polarizabilities. The Mueller matrix elements are plotted *vs* scattering angle for anisotropic polarizabilities that are perpendicular (_____) and parallel (.....) to the base pair. The wavelength used is 20 nm and the polarizability strengths are given in the text.

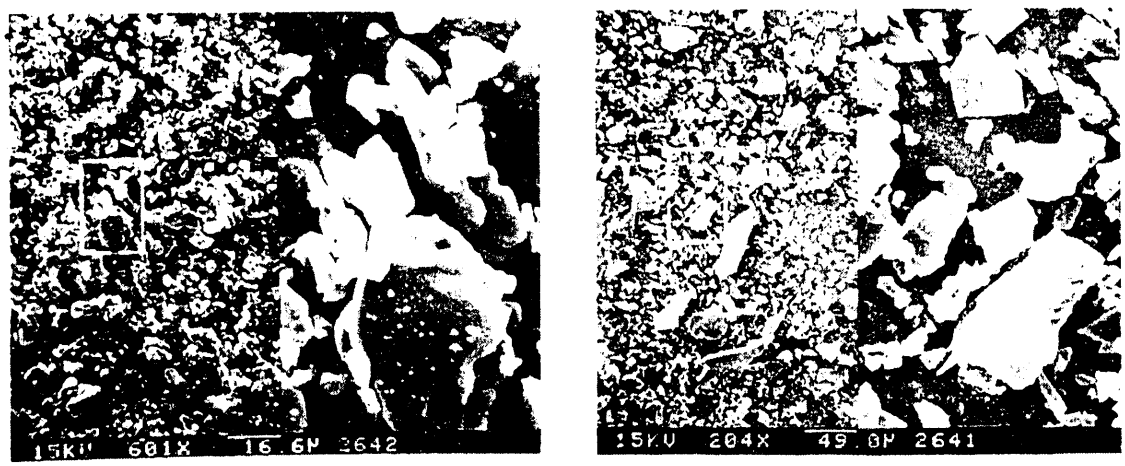

a b

Figure 7.1 Alumina particles; scanning electron micrograph. a. Linde A particles. Bar=16 μm refers to lower magnification (601×) . Higher magnification is 3005×. b. Linde bouls ground to -400 mesh. Bar=49 μm refers to lower magnification (204×). Higher magnification is 1020× .

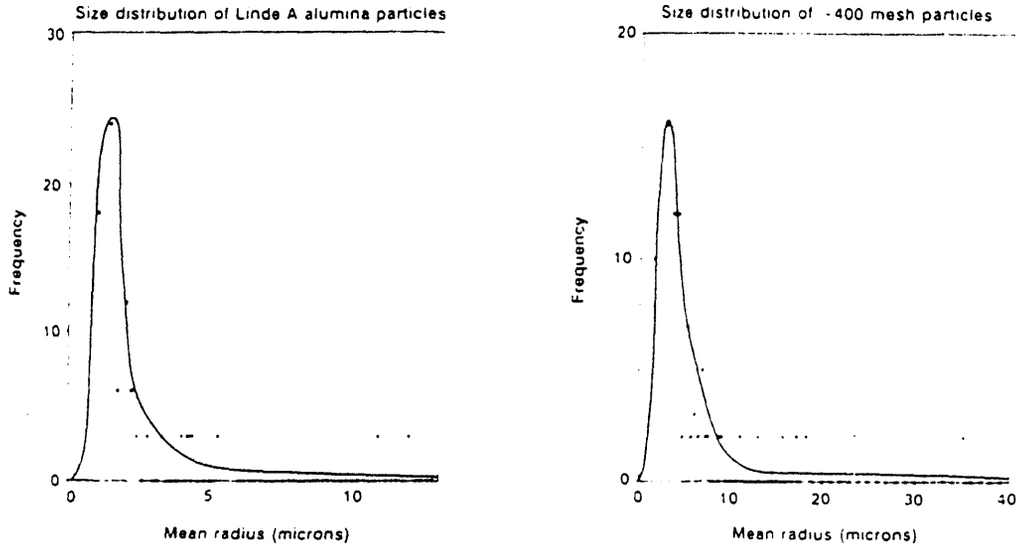

Figure 7.2 Size distributions for alumina particles. Particles were sized using the electron micrographs. The mean radius was calculated by taking the square root of the products of the lengths of the longest perpendicular axes for each particle. The frequency of each particle size, that is the number of particles within their size range divided by the total number of particles, is plotted on the vertical axis. The curves were drawn in by hand.

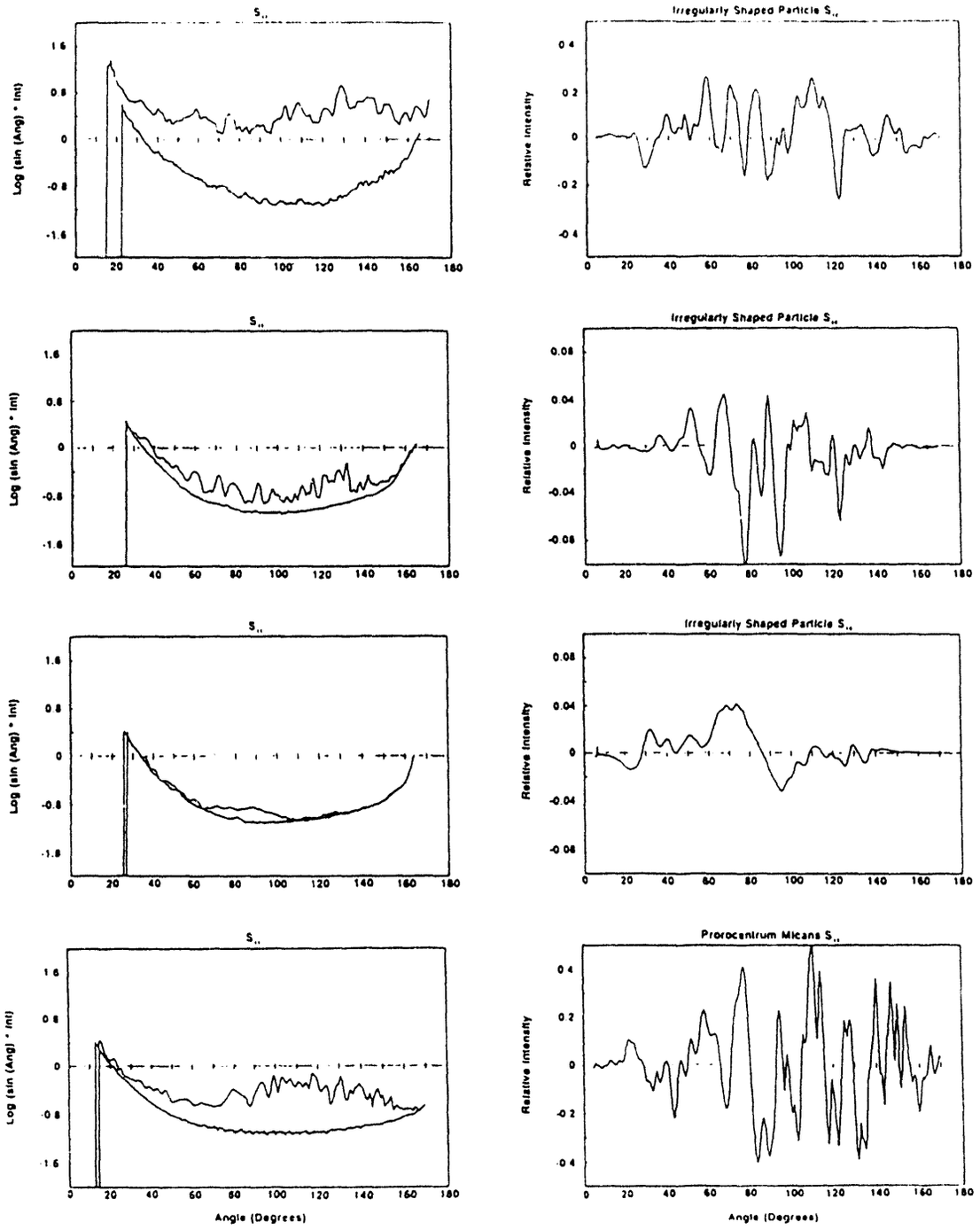

Figure 7.3 S_{11} and S_{14} plots for one *Prorocentrum micans* (lower) and three alumina particles (upper). Each S_{14} plot is shown adjacent to the S_{11} plot for that particle. Note that the S_{14} signals for each particle are plotted on different scales. The background scattering from the gel is also shown (smooth curves) on the S_{11} plots.

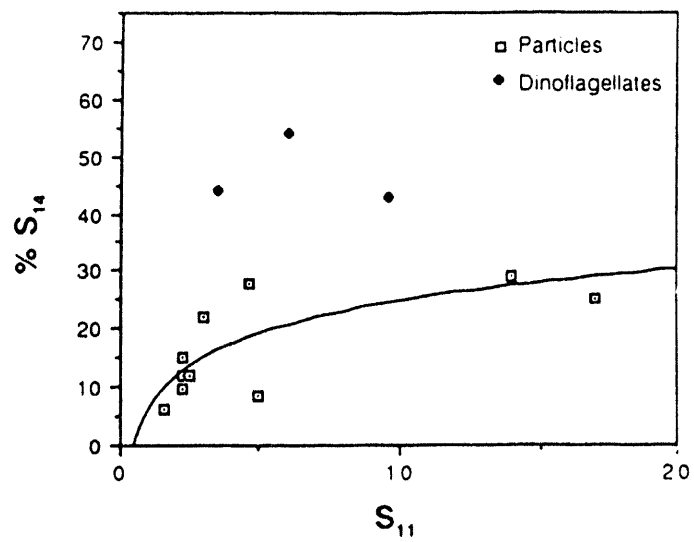

Figure 7.4 The average corrected S_{14} for the three highest peaks plotted vs the corresponding average S_{11} values for each particle.

a.

b.

Species	Deteriorated	Preserved
G. polyedra		
C. cohnii		

Figure 7.5 a. The *P. micans* chromosome. An electron micrograph of a thin section prepared from a *Prorocentrum micans*. Magnification = 60,000x. Note the arched pattern consistent with the cholesteric crystal model. b. Electron micrographs from *C. cohnii* and *G. polyedra*. Micrographs are shown for both proper and improper fixation. The magnification of the damaged *C. cohnii* chromosomes is 100,000x. All other magnifications are 60,000x.

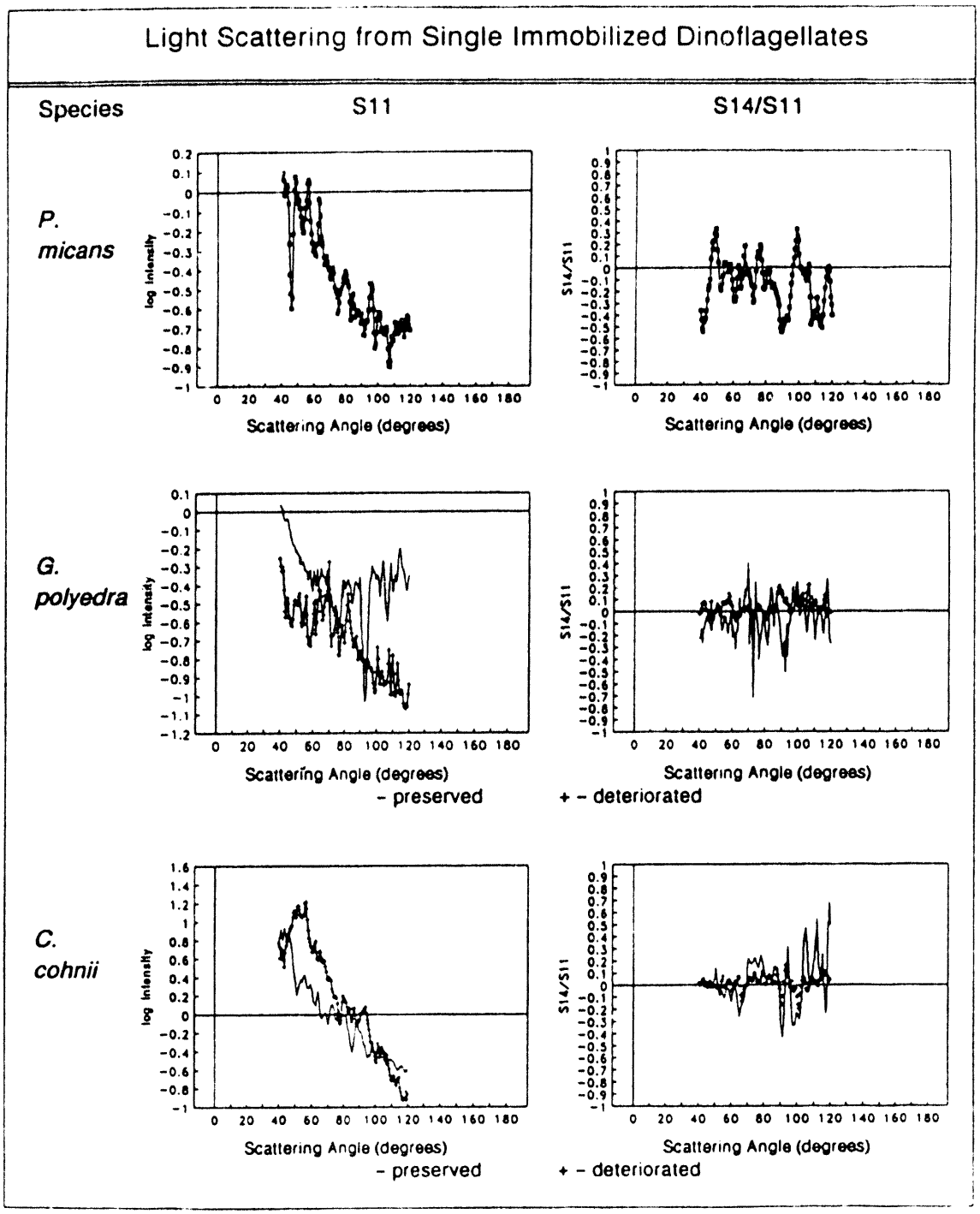

Figure 7.6 Light scattering from single immobilized dinoflagellates.

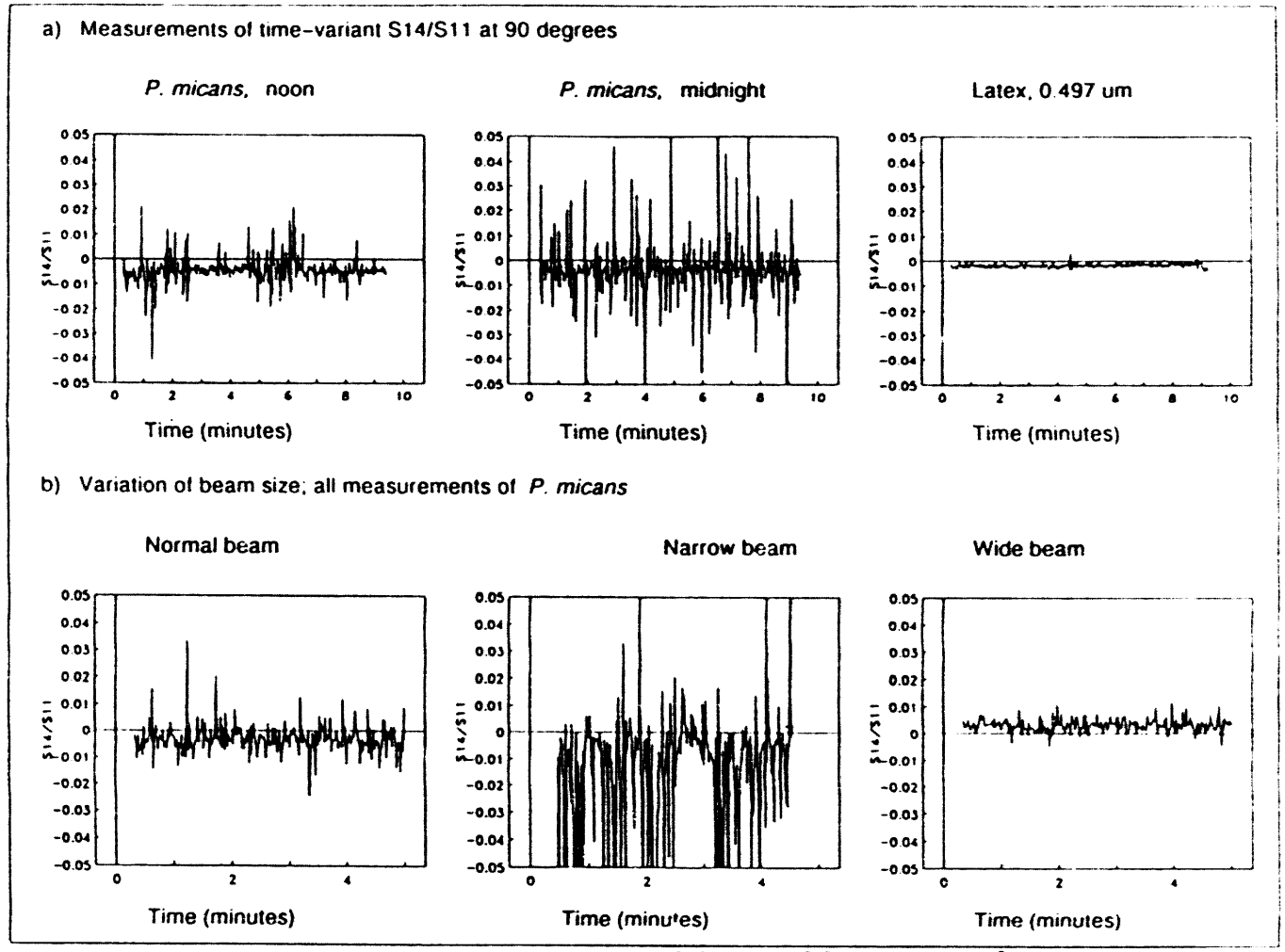

Figure 7.7 S_{14} at 90° measured as a function of time. a. Measurements from suspensions of live *P. micans* taken at noon and midnight are contrasted with measurements from 0.497um spheres. b. S_{14} measurements from *P. micans* with normal and altered beam widths are compared.

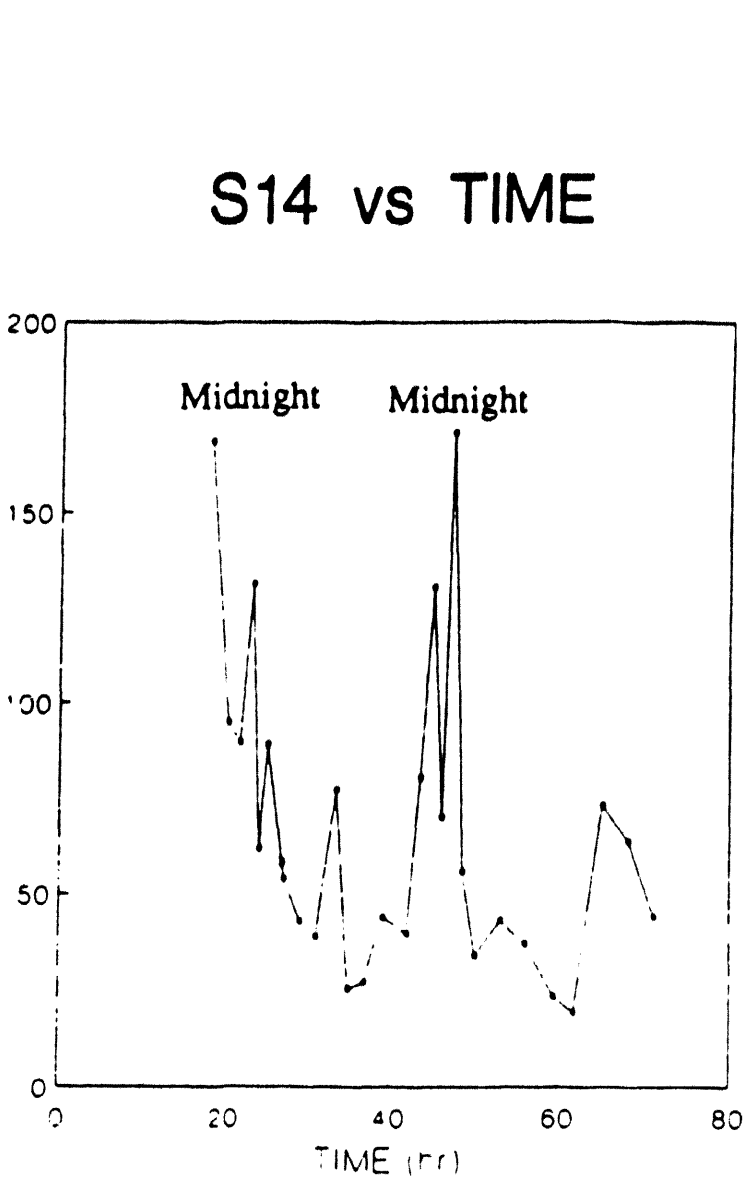

Figure 7.8 The variance multiplied by 10^6 of S_{14} *vs.* time measurements is plotted against the time of day. 0 hours corresponds to midnight of the day when the experiment began.

DATE
FILMED
4/18/94
END